UNIVERSIDADE FEDERAL DO CEARÁ

CENTRO DE TECNOLOGIA

DEPARTAMENTO DE ENGENHARIA QUÍMICA

GRUPO DE PESQUISA EM SEPARAÇÕES POR ADSORÇÃO

UNIVERSIDAD DE MÁLAGA

FACULTAD DE CIENCIAS

DEPARTAMENTO QUÍMICA INORGÁNICA, CRISTALOGRAFÍA Y MINERALOGÍA

LABORATÓRIO DE NUEVOS MATERIALES INORGÁNICOS

PEDRO AUGUSTO SILVA DE MOURA

HYDROTHERMAL STABILITY OF ZEOLITE MOLECULAR SIEVES IN NATURAL GAS DRYING BY TEMPERATURE SWING ADSORPTION

FORTALEZA

2022

PEDRO AUGUSTO SILVA DE MOURA

HYDROTHERMAL STABILITY OF ZEOLITE MOLECULAR SIEVES IN NATURAL GAS DRYING BY TEMPERATURE SWING ADSORPTION

Thesis submitted to the Universidade Federal do Ceará as a requirement to obtain the DSc Degree in Chemical Engineering and to the Universidad de Málaga as a requirement to obtain the PhD Degree in Chemistry, Chemical Technology, Materials and Nanotechnology

Advisor: Profª. Dra. Diana Cristina Silva de Azevedo

Co-Advisor: Prof. Dr. Enrique Rodriguez Castellón

Co-Advisor: Prof. Dr. Moisés Bastos Neto

FORTALEZA

2022

Dados Internacionais de Catalogação na Publicação
Universidade Federal do Ceará
Biblioteca da Pós-Graduação em Engenharia
Elaborada pela bibliotecária Aline Vieira do Nascimento CRB889

M889h Moura, Pedro Augusto Silva de.

Hydrothermal stability of zeolite molecular sieves in natural gas drying by temperature swing adsorption. / Pedro Augusto Silva de Moura. – 2022.
150 f. : il. color.

Tese (doutorado) - Universidade Federal do Ceará, Centro de Tecnologia, Programa de Pós-Graduação em Engenharia Química, Fortaleza; Universidad de Málaga, Facultad de Ciencias, Programa de Doctorado: Química y Tecnologías Químicas. Materiales y Nanotecnología, Málaga, Espanha, 2022.
Orientação: Profa. Dra. Diana Cristina Silva de Azevedo.
Coorientação: Prof. Dr. Moisés Bastos Neto.
Coorientação: Prof. Dr. Enrique Rodríguez Castellón

1. Adsorption. 2. Zeolites. 3. Premature aging. 4. Hydrothermal Stability. I.Título.

CDD 627

PEDRO AUGUSTO SILVA DE MOURA

HYDROTHERMAL STABILITY OF ZEOLITE MOLECULAR SIEVES IN NATURAL GAS DRYING BY TEMPERATURE SWING ADSORPTION

Thesis submitted to the Universidade Federal do Ceará as a requirement to obtain the DSc Degree in Chemical Engineering and to the Universidad de Málaga as a requirement to obtain the PhD Degree in Chemistry, Chemical Technology, Materials and Nanotechnology

Approved on 2 May 2022

Thesis Committee:

Prof. Dra. María Olga Guerrero Pérez

Full Professor of Chemical Engineering
Universidad de Málaga

Member

Prof. Dr. Moisés Bastos Neto

Full Professor of Chemical Engineering
Universidade Federal do Ceará

President (Co-Advisor)

Prof. Dr. Sebastião Mardônio Lucena

Full Professor of Chemical Engineering
Universidade Federal do Ceará

Member

Prof. Dr. Joaquín Silvestre Albero

Full Professor of Inorganic Chemistry
Universidad de Alicante

Member

Prof. Dra. Josefa María Mérida Robles

Full Professor of Inorganic Chemistry
Universidad de Málaga

Member

“The greatest glory in living lies not in never falling, but in rising every time we fall.”

-Nelson Mandela

ABSTRACT (English)

Zeolites are well known crystalline aluminosilicates, which may be used in processes that take advantage of their molecular sieving effect, such as natural gas drying. They are often used in cyclic processes that swing pressure and/or temperature to perform adsorption and desorption steps. It is recognized that thermal stress may decrease process performance of the adsorbent upon prolonged use. In this thesis, Chabazite (CHA) and Linde Type A (LTA) cationic zeolites with three different *Si/Al* ratios and two compensating cations were investigated by thermally aging the samples using a laboratory-scale protocol. Two Premature Aging Protocols – PAPs were proposed that considered the conditions which the adsorbent is exposed to in Temperature Swing Adsorption (TSA) process for natural gas drying. The sample was previously saturated with water and *n*-heptane vapors (as a reference hydrocarbon) followed by pressurization (30 bar) and heating (573 K) with a mixture of CO_2 and CH_4 (1:4, v/v). The *Si/Al* ratios of the CHA and LTA samples under study were 1, 2 and 5 and the compensating cations were *Na* and *K*. Pristine and aged samples were characterized and compared, focusing on the interplay between adsorbent features and the hydrothermal stability. X-Ray Diffraction (XRD) analyses showed that all materials remain with a similar crystallinity despite undergoing the aging protocol (except for the LTA with *K*). X-Ray Photoelectron Spectroscopy associated with ^{29}Al and ^{27}Si Nuclear Magnetic Resonance showed that the bulk *Si/Al* ratio does not change significantly upon aging, even though there may be *Al* migration from the outer to the inner framework, leading to an increase in the *Si/Al* ratio on the external surface of the materials. Chemical analyses reveal that there is an unbalance between *Al* and the compensating alkali cations in the case of *Si/Al* = 5, for both CHA and LTA. This excess *Al* is expected to increase the total acidity, either as Extra Framework *Al* (*EFAl*) or as Acid Sites. The enhanced total acidity in the CHA samples was confirmed by NH_3-TPD and a massive carbon deposition under the aging protocol was observed in CHA and LTA with Si/Al=5. The *K* cation provides different features to CHA and LTA materials submitted to the aging protocol. Once *Na* cations were replaced by *K* in zeolites, thermal resistance of CHA materials is enhanced. Nonetheless, in LTA zeolites, the presence of *K* leads to partial material amorphization upon aging, which was verified by XRD and Fourier Transform Infrared Spectroscopy. Adsorption experiments reveal that aged

materials presented lower N_2 and CO_2 adsorption capacities at low temperatures and an increased content of carbon as compared to their pristine counterparts. The water vapor adsorption isotherms at 313 K also showed decreased uptakes for all aged materials as compared to the respective pristine samples. For LTAs, the pristine sample with the lowest *Si/Al* ratio (=1) in *Na* form reaches a higher water adsorption capacity at 70 mbar, and the sample has an intermediate deactivation upon aging.

Keywords: Adsorption · Zeolites · Premature Aging · Hydrothermal Stability

RESUMO (Português)

As zeólitas são aluminosilicatos cristalinos bem conhecidos, que podem ser utilizadas em processos que se beneficiam do seu efeito de peneiramento molecular, tais como a secagem do gás natural. São frequentemente utilizadas em processos cíclicos que oscilam a pressão e/ou temperatura para realizar as etapas de adsorção e dessorção. Reconhece-se que o *stress* térmico pode diminuir o desempenho do processo de adsorção após utilização prolongada do material adsorvente. Nesta tese, as zeólitas catiônicas Chabazita (CHA) e Linde Tipo A (LTA) com três razões *Si/Al* diferentes e dois cátions de compensação foram investigadas através do envelhecimento térmico das amostras utilizando um protocolo em escala laboratorial. Foram propostos dois protocolos de envelhecimento prematuro - PAPs - que consideraram as condições a que o adsorvente é exposto no processo de *Temperature Swing Adsorption (TSA)* para secagem de gás natural. A amostra foi previamente saturada com água e vapores de n-heptano (como hidrocarboneto de referência), seguido de pressurização (30 bar) e aquecimento (573 K) com uma mistura de CO_2 e CH_4 (1:4, v/v). As razões *Si/Al* das amostras de CHA e LTA em estudo foram 1, 2 e 5 e os cátions de compensação foram *Na* e *K*. Amostras virgens e envelhecidas foram caracterizadas e comparadas, concentrando-se na correlação entre as características dos adsorventes e sua estabilidade hidrotérmica. As análises de Difração de Raios X (*XRD*) mostraram que todos os materiais permanecem com cristalinidade semelhante apesar de terem sido submetidos ao protocolo de envelhecimento (exceto a LTA com *K*). A Espectroscopia Fotoelétrica de Raios X associada à Ressonância Magnética Nuclear de ^{29}Al e ^{27}Si mostraram que a relação *Si/Al* global das amostras não se altera significativamente com o envelhecimento, embora possa haver migração de *Al* da superfície externa para os poros internos, levando a um aumento da relação *Si/Al* na superfície externa dos materiais. As análises químicas revelam que existe um desequilíbrio entre *Al* e os cátions alcalinos de compensação, no caso das amostras com razão *Si/Al* = 5, tanto para CHA como para LTA. Espera-se que este excesso de *Al* aumente a acidez total, quer como Al fora da rede *(EFAl)*, quer como sítios ácidos na estrutura. O aumento da acidez total nestas amostras foi confirmado por *NH3-TPD* e foi observada uma deposição maciça de carbono nestas amostras (Si/Al=5) ao serem envelhecidas. O cátion *K* fornece diferentes características aos materiais CHA e LTA submetidos ao protocolo de envelhecimento.

Uma vez que os cátions *Na* foram substituídos por *K* em zeólitas, a resistência térmica dos materiais CHA é aumentada. No entanto, nas zeólitas LTA, a presença de *K* leva à amorfização parcial do material após o envelhecimento, o que foi verificado pela Espectroscopia de Infravermelho por Transformada de Fourier e XRD. Isotermas de equilíbrio de adsorção revelam que os materiais envelhecidos apresentaram capacidades de adsorção a baixas temperaturas de N_2 e CO_2 inferiores e um maior conteúdo de carbono em comparação com os seus homólogos virgens. As isotermas de adsorção de vapor de água à 313 K também revelaram uma diminuição da capacidade para todos os materiais envelhecidos, em comparação com as respectivas amostras virgens. Para as LTAs, a amostra virgem com a menor relação *Si/Al* (=1) em forma de *Na* atinge a mais alta capacidade de adsorção de água a 70 mbar, apesar de uma desativação intermédia ao envelhecer, que se agrava significativamente na forma potássica. Para materiais CHA, a razão intermediária de *Si/Al* (≈2) na forma *K* proporciona o melhor compromisso entre hidrofilicidade e estabilidade hidrotérmica. Em geral, as CHA se revelaram mais resistentes ao envelhecimento do que as LTA e a deposição de *C* é um dos principais indicadores da desativação dos adsorventes. Desta forma, a amostra S-CHAc-SiAl2-K foi preferida, contudo, a amostra S-LTAc-SiAl2-Na também apresentou devido a uma baixa deposição de *C* e a uma melhor adsorção de vapor de água.

Palavras-Chave: Adsorção · Zeólitas · Envelhecimento Prematuro · Estabilidade Hidrotérmica

RESUMEN EXPANDIDO (Español)

- PLANIFICACIÓN GENERAL

La tesis se divide en ocho capítulos: el **capítulo 1** se expone la motivación para llevar a cabo esta investigación, desde la elección de los materiales adsorbentes hasta la investigación del envejecimiento prematuro en los procesos de secado del gas natural. En el **capítulo 2** se explican los objetivos principales y secundarios. En el **capítulo 3** hay una introducción teórica sobre los temas en los que se basará la investigación. En el **capítulo 4** se indican los materiales y métodos utilizados para la realización de esta investigación, desde los reactivos utilizados en la síntesis de los adsorbentes, los equipos utilizados en la caracterización de los materiales y la metodología utilizada para el envejecimiento prematuro de los absorbentes aplicados en el secado del gas natural. El capítulo siguiente se divide en cuatro secciones. La **sección 5.1** aporta la caracterización completa, antes y después de un protocolo de envejecimiento en laboratorio, de la zeolita CHA con Si/Al ~ 2,0 en forma sódica (*Na*). En primer lugar, a esta zeolita catiónica CHA (S-CHAC-SiAl2-Na) se le sometió a un protocolo de envejecimiento prematuro propuesto - PAP-2 (una explicación detallada se encuentra en el **capítulo 4**, **sección 4.3**) durante diferentes tiempos de envejecimiento. A la misma muestra también se le sometió también a otro procedimiento de envejecimiento, denominado PAP-1, propuesto originalmente por nuestro grupo de investigación en 2019 (Gomes Santiago et al., 2019). Impulsado por la necesidad de un protocolo de envejecimiento que sólo requiera una pequeña cantidad de muestra, el estrés térmico causado la exposición de la muestra a altas temperaturas y la homogeneización del material envejecido, la nueva metodología (PAP-2) fue validada contra el PAP-1 en este capítulo. La caracterización del adsorbente y las isotermas de adsorción de los gases sonda y del vapor de agua se realizaron antes y después de los dos protocolos de envejecimiento para correlacionar los cambios observados en la textura y el rendimiento de la adsorción con las condiciones del PAP. En la **sección 5.2**, se investigan los tamices moleculares CHA sintetizados bajo diferentes relaciones Si/Al y cationes compensadores. Se estudiaron tres zeolitas catiónicas con una relación *Si/Al* intermedia (≈ 2,0) y un alta (≈ 5,0) y dos cationes compensadores (*Na* y *K*). El impacto del envejecimiento hidrotérmico en cada una de las muestras se analizó mediante

técnicas fisicoquímicas, monitorizando las isotermas de adsorción de las moléculas sonda (N_2 y CO_2) y del vapor de agua antes y después del protocolo de envejecimiento. La **sección 5.3** tiene una organización similar a la de la **sección 5.2**, pero con una zeolita catiónica diferente, la LTA. Se sintetizaron cuatro adsorbentes variando la relación *Si/Al* (1, 2 y 5) y el catión compensador (*Na* y *K*). En la **sección 5.4**, se realiza una comparación entre las dos zeolitas catiónicas envejecidas (CHA y LTA), centrándose en materiales CHA x LTA similares, en lo que respecta a la relación *Si/Al* y al catión compensador. El **capítulo 6** se centra en la conclusión extraída de los análisis realizados. Al final de cada sección del **capítulo 5** se ofrecen conclusiones parciales, pero en el **capítulo 6** se sintetizan todas estas conclusiones en un solo texto. El **capítulo 7** contiene material complementario para la caracterización de los adsorbentes. El último capítulo (**capítulo 8**) contiene algunas sugerencias para futuros trabajos de investigación. Por fin, las **Referencias** de artículos y libros utilizados en esa tesis.

- INTRODUCIÓN TEÓRICA

Uno de los principales retos de la humanidad es la necesidad cada vez mayor de generar energía. Desde la primera revolución industrial en la década de 1860, el suministro de energía para todas las actividades de nuestra vida se ha convertido en algo esencial. Acciones rutinarias, como la comunicación, el transporte, la construcción y la fabricación, requieren directa o indirectamente el suministro de energía. Para satisfacer esta demanda, cada país cuenta con diversas fuentes de generación de energía; normalmente, la cantidad total de energía consumida es proporcional al Producto Interior Bruto (OGJ, 2019). Se cree que una matriz energética mixta, que incluya petróleo, gas natural, hidroelectricidad, fuentes renovables y nucleares, es la mejor manera de mejorar el desarrollo. El Gas Natural (*NG*) aparece como una alternativa atractiva, en comparación con otros combustibles fósiles sólidos/ líquidos, debido a las inferiores emisiones de CO_2, los vastos reservorios alrededor del planeta y el alto poder calorífico. Sin embargo, el contenido de vapor de agua presente en el *NG* producido tiene una importancia crucial debido a problemas asociados con la formación de hidratos, reducción de la eficiencia energética, corrosión y/o erosión de equipos. En las instalaciones *offshore* de producción de *NG*, el secado de gas por *Temperature Swing*

Adsorption (*TSA*) es una operación unitaria obligatoria, después de la eliminación de condensados y material particulado.

En los últimos 20 años, el consumo de gas natural ha aumentado más del 2% anual y su participación en la matriz energética mundial fue del 19,3% en 1995; 20,4% en 2005; 21,9% en 2015 y 22,8% en 2018 (McKinsey & Company, 2019). Por lo tanto, es una fuente de energía destacada en el escenario global. La composición del *NG* producido en los yacimientos es variable, ya sea gas asociado o no asociado en los diferentes sitios del planeta. Sin embargo, una composición de referencia considera la presencia mayoritaria de metano (> 85%, v/v), sobre etano, propano y n-butano, en este orden. También hay varias sustancias no deseadas, como dióxido de carbono, vapor de agua, compuestos de azufre e hidrocarburos más pesados. La composición del gas natural puede variar según los distintos yacimientos. Algunas características importantes de los principales componentes del *NG*, donde se pueden apreciar diferencias significativas de propiedades entre ellos. Es importante destacar que otras impurezas, como el mercurio y los mercaptanos, deben ser convenientemente manejadas para garantizar la eficiencia/seguridad del transporte y la combustión y para evitar efectos nocivos para el medio ambiente y la salud (Speight, 2019).

Como regla general, el procesamiento del *NG* comienza con una expansión de volumen, que conduce a una disminución de la temperatura y la presión por el efecto Joule-Thomson (Marić, 2005). Por tanto, una fracción importante de los hidrocarburos pesados y de la humedad en la fase gaseosa se condensa y puede separarse fácilmente. El siguiente paso incluye la eliminación de impurezas, como el vapor de agua y el dióxido de carbono, para cumplir las especificaciones del *NG*. La presencia de impurezas puede causar toxicidad, corrosión de las tuberías y los equipos y reducción del poder calorífico (Baghban et al., 2016). La eliminación de CO_2 suele realizarse mediante absorción química en disoluciones acuosas de aminas (Araújo et al., 2017) y/o permeación selectiva por membrana (Mutch et al., 2019). La eliminación de agua (etapa de secado) se realiza por adsorción; el gas fluye a través de una columna llena de un material hidrofílico (normalmente un tamiz molecular) que es capaz de capturar las moléculas de vapor de agua presentes en el gas (Farag et al., 2011; Rezvani & Fatemi,

2020; Santos et al., 2017). El secado del gas natural juega un papel fundamental para el adecuado desempeño de las operaciones posteriores. Para obtener un producto "in spec", se deben tener en cuenta los tres aspectos siguientes:

1. Para temperaturas suficientemente bajas, el agua en fase gaseosa puede formar hidratos que encapsulan hidrocarburos ($C_nH_{2n} + 2 \times H_2O$), en una estructura cristalina. Los cristales recién formados pueden causar la obstrucción de tuberías y equipos (Talaghat & Khodaverdilo, 2019). Es importante señalar que la formación de cristales puede ser causada por flujos acelerados del gas, inducidos por grandes diferencias de presión (Hammerschmidt, 1934). También existe un problema de seguridad en cuanto a la formación de hidratos que bloquearían las tuberías y tienen el potencial de provocar reacciones de disociación explosivas (Speight, 2019);

2. La presencia de agua disminuye el poder calorífico del *NG* y, por tanto, la eficiencia de la combustión y la potencia entregada (Speight, 2019);

3. El agua asociada al dióxido de carbono y al sulfuro de hidrógeno puede provocar la corrosión de los equipos y las tuberías (Speight, 2019).

La adsorción se define como un fenómeno interfacial espontáneo que impulsa a las moléculas de un fluido libre (líquido o gas) a concentrarse (adsorbato) en la interfase, generalmente una interfase fluido-sólido, en cuyo caso el sólido se denomina adsorbente (Ruthven, 1984). La desorción es el proceso contrario, es decir, la dispersión de las moléculas que estaban previamente adheridas a la superficie por un cambio de presión, temperatura o potencial químico. Según el tipo de interacción entre el adsorbente y el adsorbato, puede haber adsorción física (Fisisorción) y adsorción química (Quimisorción). La fisisorción implica interacciones débiles, como las fuerzas de van der Waals o las interacciones electrostáticas. Libera calores bajos (comparables al calor en las transiciones de fase), es significativa a bajas temperaturas y puede tener lugar en múltiples capas de adsorción. La quimisorción, por el contrario, se caracteriza por fuertes interacciones covalentes, con la formación de una única monocapa. Además,

la adsorción química puede presentar una amplia gama de calores de adsorción comparables a los que muestran las reacciones químicas (Ruthven, 1984). Cuando se analiza un proceso cíclico (adsorción/desorción) impulsado por la adsorción, deben tenerse en cuenta varios aspectos, como las interacciones adsorbato/adsorbente, la capacidad de trabajo, la reversibilidad y cinética de la adsorción, los calores de adsorción, la selectividad para el adsorbato objetivo, entre otros factores. Por lo tanto, la fisisorción es la opción preferida para los procesos cíclicos como la *TSA* (adsorción por oscilación de temperatura) y la *PSA* (adsorción por oscilación de presión) debido a la reversibilidad y a la baja penalización energética (en comparación con la quimisorción). La elección de un buen material adsorbente se convierte en algo esencial para la alta eficiencia del proceso cíclico, algunos ejemplos de materiales son, las zeolitas, los carbones activados y los *Metal Organic Frameworks (MOFs)*.

Para describir el equilibrio de adsorción como un fenómeno monocapa o multicapa, se han propuesto algunos modelos en la literatura. El modelo más sencillo es la Ley de Henry, que establece que la concentración adsorbida es linealmente proporcional a la concentración en la fase fluida. Se aplica estrictamente sólo en cargas de adsorbato suficientemente bajas, más allá de las cuales el equilibrio de adsorción sigue un comportamiento no lineal (Tóth, 2003). Los modelos de Tóth y Freundlich son empíricos y termodinámicamente inconsistentes. Cuando la presión tiende a cero, ambos modelos no se reducen a la Ley de Henry (MOGHIMI et al., 2020; Tóth, 2003). El Modelo de Langmuir (LM), propuesto anteriormente para la adsorción en monocapa sobre una superficie adsorbente homogénea (Langmuir, 1918), es una ecuación matemática flexible que puede reproducir satisfactoriamente las isotermas de tipo I (Thommes et al., 2015). En general, la LM es capaz de ajustarse a los datos experimentales de materiales microporosos en un amplio intervalo de temperaturas y presiones. En cuanto a los parámetros utilizados en la LM, "*qmax*" representa la concentración máxima adsorbida y "*b*" da cuenta de la interacción adsorbente/ adsorbato. Como extensión del LM, el Modelo Sips, tiene en cuenta un parámetro adicional '*n*', que está relacionado con el grado de heterogeneidad de la superficie del adsorbente (Myers & Prausnitz, 1965). El modelo Brunauer-Emmett-Teller (BET) considera una superficie homogénea, en la que pueden acumularse múltiples capas adsorbidas a medida que aumenta la presión. Aparte de las moléculas de gas en la primera (mono)capa adsorbida, las capas siguientes se comportan como un líquido

saturado. Los parámetros BET son "nm", que es la concentración adsorbida en la monocapa y "*C*", que está relacionado exponencialmente con E1 (el calor de adsorción en la primera capa) (Brunauer et al., 1940). El modelo Aranovich-Donohue considera una adsorción multicapa y se ha utilizado frecuentemente para reproducir isotermas de agua de tipo II/IV (Thommes et al., 2015). Es el producto de dos términos, el primero representa la formación de la monocapa como una ecuación del Modelo Sips. El segundo término se refiere a las capas posteriores, teniendo en cuenta la presión de saturación "P_o" y un parámetro empírico "*e*" sin significado físico preciso.

Las zeolitas son materiales nanoporosos, también conocidos como tamices moleculares debido al tamaño único de sus poros, definido por su estructura cristalina, que permite que las moléculas más pequeñas (como el agua) se alojen en las jaulas internas y que las moléculas más grandes queden excluidas. Por lo tanto, este efecto de cribado puede conducir a una alta selectividad. Las zeolitas están compuestas por TO_4 como tetraedros de la Unidad Primaria de Construcción (PBU) (**Figura 3.03**), donde *T* suele ser *Si* o *Al*. El elemento *T* está en el centro y los cuatro vértices tienen átomos de oxígeno, que se comparten con los tetraedros vecinos, para dar lugar a una estructura cristalina que comprende poros y cavidades. El intercambio del átomo de *Si* por otros iones divalentes, trivalentes o tetravalentes da lugar a una gran variedad de estructuras zeolíticas (Corma & Zones, 2010). Los diferentes materiales zeolíticos se generan por las diversas cargas (A. Louis Allred, 1961) y radios iónicos (Shannon, 1976) de los diferentes cationes que se insertan en la estructura. Cuando el átomo *T* es sólo *Si* (u otro elemento tetravalente), la estructura es neutra; sin embargo, si es *Al*, hay una carga negativa en AlO^{4-}, que debe ser compensada por un catión (generando así zeolitas catiónicas) o por un protón (H^+), dando lugar a zeolitas protónicas. Considerando la relación *Si/Al* y los cationes metálicos compensadores en la estructura, la fórmula molecular general de las zeolitas catiónicas es $M_{x/n}$ $[(AlO_2)_x$ $(SiO_2)]$ w H_2O; donde, *M* representa el catión compensador; *n* es la valencia del catión; la relación *Si/Al* es *y* dividida por *x*; *w* es el número de moléculas de agua en cada célula cristalina (Vigil de la Villa Mencía et al., 2020). La síntesis hidrotermal es la ruta más común para sintetizar zeolitas, utilizando agua como disolvente. Además de las fuentes de silicio (y aluminio), se pueden requerir otros productos químicos en la síntesis, como agentes mineralizantes (MA), agentes directores de estructura (SDA) y agua. Una síntesis típica

de zeolita consta de tres pasos: Periodo de Inducción, definido como el tiempo que transcurre desde que todos los reactivos alcanzan la temperatura de reacción hasta el inicio de la formación de los cristales; la Nucleación, que corresponde a la organización estructural de la zeolita, estableciendo su periodicidad de estructura típica; y el Crecimiento Cristalino, que tiene conceptos y supuestos similares a los de la etapa de nucleación (Cundy & Cox, 2005; Yu, 2007).

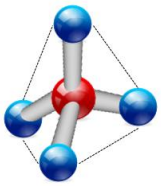

Figura 3.03. Estructura tetraédrica tridimensional (TO_4) de las zeolitas
[Esferas azules = *O*; Esferas rojas = elemento *T*]

Las principales características de una zeolita catiónica que pueden influir en su potencial de adsorción de agua y en su estabilidad hidrotérmica están interconectadas (**Figura 3.06**). A continuación, se detallarán mejor algunos aspectos.

1. Contenido de Al: La cantidad total se define por la regla de Löewenstein (Loewenstein, 1954) que prohíbe los enlaces - *Al* - *O* - *Al*. Por lo tanto, la relación *Si/Al* nunca es inferior a 1. Los átomos de *Al* pueden estar en el *framework* o fuera de ello.

2. Acidez: Los sitios de Brönsted y Lewis proporcionan directa y/o indirectamente la acidez de la zeolita. En los materiales protónicos, un mayor contenido de aluminio aumenta la concentración de hidroxilos puenteados y, por tanto, la acidez de los materiales. El número máximo de sitios de aluminio activos de Brönsted es el número de aluminios tetraédricos (Corma & Martinez, 1995).

3. Afinidad con el agua: Las moléculas de H_2O se incorporan al armazón de las zeolitas catiónicas por dos vías diferentes: (1) los cationes

compensadores extra-*framework* están rodeados por átomos de oxígeno del *framework*, lo que contribuye a las cargas eléctricas negativas, generando fuertes interacciones con el agua; asociadas a la hidratación de los cationes extra-marco (Busca, 2017a; Nachtigall et al., 2012); y (2) por enlaces débiles con la zeolita, al llenarse los poros/canales (Shim et al., 1999a). Cuando el contenido de *Al* aumenta en la estructura de la zeolita, la carga total sin neutralizar (negativa) aumenta, lo que plantea la necesidad de cationes compensadores en la estructura para equilibrar la carga. Además, la adsorción de agua también se ve afectada por el tamaño del catión, la electronegatividad y la topología de la zeolita (Nachtigall et al., 2012).

4. Estabilidad térmica: Una de las razones que hace que las zeolitas tengan un amplio uso extendido en la industria es su alta estabilidad térmica (Mintova & Barrier, 2016). Cuando el contenido de *Al* disminuye, hay una alta densidad de enlaces *Si - O - Si*, que tienen una pronunciada estabilidad térmica, y por lo tanto se requiere más energía para romper estos nuevos enlaces en comparación con los enlaces *Al - O – Si* (Cruciani, 2006; Kerr, 1967).

5. Intercambio de iones: El catión compensador para neutralizar la carga negativa en las zeolitas catiónicas provocada por la presencia de *Al* en el armazón, es generalmente Na^+, pero puede ser intercambiado por otros cationes monovalentes o divalentes del grupo alcalinos y alcalinos térreos, respectivamente.

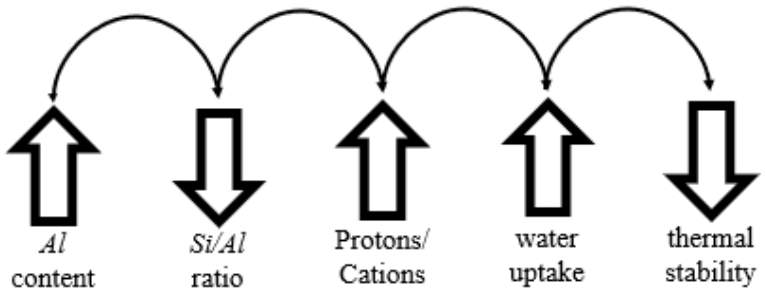

Figura 3.06. Interacción de las propiedades de las zeolitas catiónicas relacionadas con la adsorción de agua y la estabilidad hidrotermal

- MATERIALES Y METOLOGÍA

El trabajo experimental de esta tesis se ha llevado a cabo en cuatro centros de investigación diferentes. Los centros de investigación y sus siglas son *Laboratório de Pesquisa em Adsorção e Captura de CO_2* (LPACO2) de la *Universidade Federal de Ceará* (Brasil); el grupo de Nuevos Materiales Inorgánicos (NMI) de la Universidad de Málaga (España), el Instituto de Tecnología Química (ITQ) del CSIC/Universidad Politécnica de Valencia (España) y el *Laboratório de Adsorção e Catálise Aplicada* (LACAp) de la *Universidade Federal de São Carlos* (Brasil). Además, la muestra de CHA en forma de *Na* con una relación *Si/Al* de 2 se sintetizó en la *University of Mbourne* (Australia) por el Dra. Ranjeet Singh y amablemente donada para esta investigación.

En esta tesis, se sintetizaron zeolitas catiónicas CHA y LTA con tres relaciones *Si/Al* diferentes (1, 2 y 5) y dos cationes de compensación (*Na* y *K*), seguida de un envejeciendo térmico de las muestras utilizando dos procedimientos distintos de envejecimiento acelerado que imitan las condiciones reales a las que están expuestos los adsorbentes. En las etiquetas de los materiales analizados en esa tesis, el prefijo (S) indica que la muestra es casera, es decir, no comercializada, y la letra subíndice (c), junto a la estructura de la zeolita (CHA o LTA), indica que el material está en forma de cristal. También se indican la relación *Si/Al* y el metal de compensación principal (Na o K). Todos los procedimientos de síntesis utilizados en este trabajo se describen en las siguientes secciones. Se evaluaron y se compararon muestras vírgenes y envejecidas, centrándose en la interacción entre las características de los adsorbentes y la estabilidad hidrotermal. Se investigaron dos Protocolos de Envejecimiento Prematuro (*PAPs*) distintos que consideran las condiciones a las que se expone el adsorbente en el proceso de *Temperature Swing Adsorption* (*TSA*) para el secado de gas natural. En el primero (PAP-1) (Gomes Santiago et al., 2019), la muestra (25 g) se coloca en un reactor Parr. Seguidamente, se agrega n-heptano líquido a la muestra gota a gota y el reactor se cierra. El n-heptano es un hidrocarburo de tamaño intermedio en el proceso real para representar todos los hidrocarburos en la estructura. La muestra se humidifica con una corriente húmeda de N_2 durante 24 horas. A continuación, el reactor se presuriza hasta

30 bar con una mezcla de CO_2/CH_4 con una razón molar de 1:4 v/v. Por último, se calienta el sistema hasta 573 K, y posteriormente se disminuye la temperatura hasta 303 K, la cantidad de ciclos (calentamiento/resfriamiento) se determina previamente. En el segundo (PAP-2), la muestra (1 g) se coloca en un portamuestras dentro de una cámara. La muestra se satura con vapor de agua y n-heptano. A continuación, la cámara se presuriza hasta 30 bar con una mezcla de CO_2/CH_4 (1: 4 v/v). Por último, el sistema se calienta hasta 573 K y la temperatura se mantiene durante un determinado número de días. El PAP-2 en comparación con el PAP-1, se aplica más a muestras sintetizadas en menor escala por exigir una menor cantidad de masa y proporcionar un material más regular, en cuanto al contenido de elementos. Además, la presencia de hidrocarburos (n-heptano) asociados con altas temperaturas tiene un papel clave en la desactivación del material.

Para analizar las modificaciones en la composición química, la estructura y las propiedades de adsorción de las muestras de zeolita antes y después de someterse a un protocolo de envejecimiento, se han empleado varias técnicas. Para examinar la cristalinidad y el depósito de sustancias en la superficie del adsorbente, se aplicaron técnicas de rayos X: Espectroscopia de Fotoelectrones de Rayos X (*XPS*), Difracción de Rayos X (*XRD*) y Fluorescencia de Rayos X (*XRF*). Para obtener la composición química, se realizó la Espectroscopia de Emisión Orbital de Plasma Acoplado Inductivamente (*ICP-OES*) y el Análisis Elemental - C, H, N. La estabilidad térmica de las muestras y la morfología se examinaron mediante Análisis Termogravimétrico Diferencial/ Calorimetría de Barrido Diferencial/ Espectrometría de Masas (*TG/DSC-MS*) y Microscopía Electrónica de Barrido (*SEM*), respectivamente. La acidez general de la superficie, las contribuciones de los principales elementos a granel y los enlaces de la estructura se evaluaron mediante la Desorción Termo-Programada de NH_3 (*TPD-NH3*), la Resonancia Magnética Nuclear (*NMR*) en estado sólido y la Espectroscopia Infrarroja por Transformada de Fourier (FT-IR), respectivamente. Para evaluar la textura porosa de las muestras, se midieron las isotermas de le moléculas sonda típicas (N_2 a 77 K y CO_2 a 273 K). Las isotermas de adsorción de vapor de agua se realizaron a 313 K para los adsorbentes prístinos y envejecidos.

Las isotermas de vapor de agua se midieron por el método gravimétrico utilizando un Analizador Gravimétrico Inteligente - IGA 002 de Hiden® (Reino Unido). El equipo consta de un sistema de ultravacío que alcanza presiones de hasta 10^{-7} bar, una microbalanza con una estabilidad de aproximadamente 10^{-6} g, tres transductores de presión en los rangos de 0 - 10 mbar, 0 - 100 bar, 0 - 1 bar y un termopar situado a 5 mm del soporte de la muestra para controlar la temperatura del sistema. Además, se acopla al sistema un baño termostático para mantener la temperatura deseada. El vapor se genera estáticamente a 328 K a partir de agua desionizada contenida en un pequeño cilindro. Por lo tanto, la presión de vapor máxima dentro del sistema está limitada por la presión de vapor de agua a la temperatura de trabajo (328 K), es decir, 73,8 mbar (Dean, 1998). La masa de muestra requerida en un experimento típico es de aproximadamente 35 mg. Antes de la medición de la isoterma, las muestras de zeolita se desgasifican a alto vacío (hasta 10^{-7} mbar) y 573K durante 10 horas. A continuación, se inyecta automáticamente vapor de agua para mantener la presión dentro de la cámara desde 0 hasta 70 mbar. Los efectos de la flotabilidad pueden despreciarse en este sistema, ya que el rango de presión de trabajo es bajo. Los datos de la isoterma del vapor de agua se ajustaron mediante el modelo Aranovich-Donohue, que considera el modelo Sips para la formación de monocapa (Aranovich & Donohue, 1995; Myers & Prausnitz, 1965). El Modelo Aranovich-Donohue considera una adsorción multicapa y se ha utilizado frecuentemente para reproducir isotermas de agua de tipo II/IV (Thommes et al., 2015). Es el producto de dos términos, el primero representa la formación de la monocapa como una ecuación del Modelo Sips. El segundo término se refiere a las capas posteriores, teniendo en cuenta la presión de saturación y un parámetro empírico sin significado físico preciso.

- DISCUSSIONES Y CONCLUSIONES

Ser sintetizaron dos grupos de materiales zeoliticos (CHA y LTA) con diferentes relaciones *Si/Al* (1, 2 y 5) y cationes compensadores (*Na* y *K*) fueron sintetizados con éxito mediante rutas hidrotermales, en algunos casos con la ayuda de un agente orgánico de estructuración directa. Las técnicas químicas y físico-químicas permitieron medir diferentes propiedades texturales y composicionales (superficiales y

de volumen) en dichos materiales. Ambos Protocolos de Envejecimiento Prematuro (PAP- 1 y 2) condujeron a una leve degradación en las propiedades texturales y de adsorción de agua en los dos grupos de adsorbentes, lo que permitió profundizar en la investigación sobre la estabilidad hidrotérmica de las zeolitas catiónicas en procesos de secado TSA. La presencia de hidrocarburos (n-heptano) asociada a las altas temperaturas demostró tener un papel clave en la desactivación del material. El nuevo protocolo de envejecimiento propuesto (PAP-2) provocó una leve degradación de la estructura cristalina de las muestras con un tamaño de muestra mucho menor que el PAP-1. Cuanto mayor es el tiempo de envejecimiento, mayor es el grado de degradación que se observa en las diversas propiedades estudiadas. Se puede postular que el hidrocarburo presente en el protocolo de envejecimiento (n-heptano) se adsorbe uniformemente en los poros interiores y exteriores de la zeolita, ya que se carga a la muestra en fase de vapor, a diferencia del PAP-1. Todos los materiales envejecidos mostraron un empeoramiento de las características texturales, lo que parece estar directamente correlacionado con el aumento del contenido de *C* en la masa. En cuanto al periodo de envejecimiento, el intervalo de 20-30 días provoca las modificaciones más pronunciadas en la porosidad y la cristalinidad, aunque no tan drásticas como en el PAP-1. Por lo tanto, se tomó 30 días como período de envejecimiento utilizado en las siguientes **secciones 5.2, 5.3** y **5.4**. Comparando los resultados del PAP-1 y del PAP-2 en un portamuestra simple y doble, presentan diferentes grados de degradación. El mantenimiento de las altas temperaturas impuestas por el PAP-2 provoca una mayor pérdida de cristalinidad. Además, las muestras envejecidas sometidas al PAP-2 presentaban una composición más homogénea (en particular el análisis de CHN) tanto en una puerta muestra simple como en uno doble. Dicho esto, el PAP-2 (30 días) utilizando un portamuestra doble fue el método de envejecimiento elegido para evaluar el impacto de la relación *Si/Al* y la naturaleza del catión de compensación en la estabilidad hidrotérmica de las zeolitas catiónicas.

El contenido de *K* desempeña un papel diferente en ambas clases de zeolita. Primero, el *K* en la CHA, mejora la resistencia térmica que es un factor clave para los procesos de *TSA*, representada por discrepancias en la cristalinidad de materiales envejecidos que contienen diferentes cationes compensadores. Además, este catión de compensación asociado a los materiales CHA desarrolló un efecto de tamizado,

dificultando el depósito de *C* en la superficie adsorbente, que es una de las principales razones de la desactivación de sólidos. Los análisis elementales de CHN revelaron que la muestra de S-CHAc-SiAl2-K retiene menos contenido de *C* entre todos los materiales de LTA y CHA. Por otro lado, el contenido de *K* en LTA estimula la amorfización de la estructura, reduciendo los enlaces *T – O – T*, de ahí la desorganización de las jaulas de sodalita. Los análisis *FT-IR* revelaron que la señal correspondiente a D4R (presentes en las *Primary Building Unit – PBU*s) disminuye de intensidad desde los materiales vírgenes hasta materiales envejecidos.

La gran mayoría de los materiales zeolíticos vírgenes y envejecidos tienen solo *Al* tetraédrico (dentro de la estructura) como se identificó por análisis ss-*NMR*, pero las muestras con una alta relación *Si/Al* (S-CHAc-SiAl5-Na y S-LTA-SiAl5-Na), además del *Al* dentro de la estructura, se identificaron *Extra-Frameworks Al* (*EFAls*) también mediante experimentos de *NMR*. Además, las mismas dos muestras envejecidas presentaron los mayores depósitos de *C*. Como conclusión, los *EFAls* desarrollan un papel clave en la intensificación del depósito de *C* al envejecer. Se puede postular que el depósito de C se produce en las superficies internas y externas, identificadas por *XPS* y análisis elemental CHN. Además, se observó la migración de *Al* desde la superficie externa a la interna del material adsorbente en todos los sólidos envejecidos. A partir de los experimentos de *XPS*, la relación Si/Al en la superficie externa aumenta después del protocolo de envejecimiento, mientras que la relación *Si/Al* identificada por los experimentos de ss-*NMR* no cambia, lo que significa que la totalidad (*bulk* y superficie), mantiene su valor después del PAP-2. La duración del envejecimiento es proporcional al movimiento, lo que significa que la migración de *Al* continúa teniendo lugar durante todo el protocolo de envejecimiento.

La acidez de las zeolitas es un arma de doble filo que mejora el carácter hidrófilo y el deósito de carbono, simultáneamente. Los materiales zeolíticos con cargas desequilibradas pueden crear Sitios Ácidos de Brönsted (*BAS*) que está compuesto por hidroxilos puenteados, el sitio ácido más fuerte en las zeolitas. De esta manera, hay una atracción más intensa por las moléculas ácidas, como el agua. Por otro lado, el depósito de carbono también aumenta y puede bloquear los poros, lo que dificulta la

accesibilidad del adsorbato al interior de los microporos. En la mayoría de los materiales analizados en esta tesis, existe una proporción entre la acidez de *BAS* y/o *EFAls*, hidrofilicidad y depósito de *C* al envejecer. Sin embargo, la muestra S-LTAc-SiAl2-Na presenta un interesante mantenimiento de la capacidad de adsorción, debido principalmente a una bajo depósito de carbono. Es necesario realizar más estudios en esta muestra, con el fin de observar la acumulación continua de *C* y el efecto que se produce en la estabilidad hidrotermal.

Evaluando ambos grupos de zeolitas, la evidencia experimental mostró una mejor estabilidad para las muestras de CHA sobre LTA durante el envejecimiento. La resistencia térmica superior puede explicarse por un mayor *Framework Density (FD)* de los materiales CHA. Además, las CHA tienen poros de cavidad más pequeños que previene la ramificación y formación de compuestos mayores de hidrocarburos previamente adsorbidos, de esta manera, el *C* retenido sale continuamente de la muestra, induciendo una reducción en la desactivación. La estabilidad hidrotermal de un material en un proceso *TSA* durante un período prolongado debe tener en cuenta, no solo la capacidad de adsorción de vapor de agua, sino el equilibrio térmico y la capacidad de prevenir el depósito de *C* en la estructura.

Palabras-Clave: Adsorción · Zeolitas · Envejecimiento Prematuro · Estabilidad Hidrotérmica

LIST OF FIGURES

LIST OF TABLES

ABREVIATIONS

ADM	Aranovich-Donohue Model
AN	Avogadro Number
BAS	Brönsted Acid Sites
BDH	Aluminate hydroxide
BE	Binding Energy
BET	Brunauer-Emmett-Teller
CHA	Chabazite
DEDMAOH	Diethyldimethyl-ammonium hydroxide 20 wt.%
DR	Dubinin-Radushkevich
DTA/DSC-MS	Differential Thermogravimetric Analysis/ Differential Scanning Calorimetry - Mass Spectrometry
EFAl	Extra-Framework *Al*
FD	Framework Density
FT-IR	Fourier Transform – Infrared Spectroscopy.
ICP-OES	Inductively Coupled Plasma – Optical Emission Spectroscopy
IPA	Aluminium Isopropoxide ≥ 98 wt.%
ITQ	*Instituto de Tecnología Química*
LACAp	*Laboratório de Adsorção e Catálise Aplicada*
LM	Langmuir Model
LPA	*Laboratório de Pesquisa em Adsorção e Captura de CO_2*
LTA	Linde Type A
MA	Mineralizing Agent
MM	Molar Mass
MRs	Membered Rings
NG	Natural Gas
NMI	*Nuevos Materiales Inorgánicos*
NMR	Nuclear Magnetic Resonance
OSDA	Organic Structure Direct Agent
PAP	Premature Aging Protocol
PBU	Primary Boundary Unit

PSA	Pressure Swing Adsorption
SAP	Sodium Aluminate Pure
SAS	Sodium Aluminate Solution
SDA	Structure Direct Agent
SSS	Sodium Silicate Solution 1.5 S.G.
SEM	Scanning Electron Microcopy
TEAOH	Tetraethyl-ammonium hydroxide 35 wt.%
TMACl	Tetramethyl-ammonium chloride ≥ 97 wt.%
TMAda	NNN-trimethyl-1-adamantammonium
TMAOH	Tetramethyl-ammonium hydroxide 25 wt.%
TPD-NH3	Temperature Programmed Desorption of NH_3
TSA	Temperature Swing Adsorption
XPS	X-Ray Photoelectron Spectroscopy
XRD	X-Ray Diffraction
XRF	X-Ray Fluorescence

SYMBOLS

q_{max}	Maximum adsorbed in all adsorption sites
b	Adsorbent/adsorbate interaction
n_m	Adsorbed concentration in the monolayer
C	Exponentially related to E_1 (the heat of adsorption in the first-layer)
P	Vapor pressure
Po	Saturation pressure
σ	Cross section area of a probe molecule
V_P	Pore volume
ρ	Density of the adsorbed
D	Empirical Constant from Dubinin-Radushkevich Method
n	Number of adsorbed mols
Φ	Parameter relating the lost in hydrophilicity by the C content
λ	Parameter relating the lost in micropore volume by the C content

SUMMARY

1 MOTIVATION

The increasing energy consumption worldwide demands a higher efficiency in power generation (IEA, 2021). Natural Gas – NG appears as an attractive alternative, as compared to solid/liquid fossil fuels, due to lower CO_2 emissions, vast reservoirs around the planet and relatively high calorific power (OECD, 2020). Nevertheless, the water vapor content present on produced NG has a crucial importance due to problems associated with the hydrate formation, reduced power efficiency, corrosion and/or erosion of equipment and pipelines (Rezvani & Fatemi, 2020; Talaghat & Khodaverdilo, 2019).

In offshore NG production facilities, gas drying by Temperature Swing Adsorption – TSA is a mandatory unit operation, following the removal of condensates and particulate matter (Santos et al., 2017; Speight, 2019). In the adsorption step of a drying TSA cycle, the adsorbent packed in a column is ordinarily submitted to high pressures (around 30 bar) and a gas feed containing CO_2, H_2O and trace heavier hydrocarbons ($C5+$), besides methane. After being loaded with water, the column is heated to desorb water and set up the adsorbent for another adsorption step. Chabazite – CHA and Linde Type A – LTA are interesting materials to be applied in NG TSA drying. Both zeolites in cationic forms have different features that may fluctuate depending on the composition (Singh & Webley, 2005) and investigations regarding its water vapor adsorption have reported (Nascimento et al., 2021; Wang, 2020). Even though the general correlations between zeolite features (such as *Si/Al* ratio, compensating cation or proton) and its hydrophilicity and thermal stability are well known, the combined effect of water, traces of heavy hydrocarbons, high pressure with CO_2 and CH_4 and elevated temperature in a confined pore, such as the small pore of CHA and LTA, is yet to be investigated. A better understanding about the interplay of zeolite features, water uptake and its thermal stability under these severe conditions should allow to identify the main causes of premature aging and guide the choice of robust and high-capacity adsorbents for TSA drying.

Therefore, the aim of this thesis is to investigate the influence of the *Si/Al* ratio and the compensating cations of CHA and LTA cationic zeolites on their water uptake and thermal stability, considering process conditions currently found in offshore NG TSA drying. The materials stability was assessed by means of an aging protocol which accounted for the conditions found in TSA natural gas drying and the trade-off between the main adsorbent features that impact on the material performance is analyzed. Three CHA and four LTA cationic zeolite samples were synthetized with different *Si/Al* ratios (approximately 1, 2 and 5) in sodium and potassium forms. Then, the samples were submitted to Premature Aging Protocols (PAPs) that mimic the severity of TSA processes for NG drying (Gomes Santiago et al., 2019). Before and after undergoing the PAP, samples were characterized by X-Ray Diffraction (XRD), X-Ray Photoelectron Spectroscopy (XPS), CHN Elemental Analysis, Inductively Coupled Plasma – Optical Emission Spectroscopy (ICP-OES), Fourier Transform Infrared Spectroscopy (FT-IR), Nuclear Magnetic Resonance (NMR), Differential Thermogravimetric Analysis/ Differential Scanning Calorimetry-Mass Spectrometry (DTA/DSC-MS) and Scanning Electron Microscopy (SEM). N_2 and CO_2 adsorption/desorption isotherms at 77 K and 273 K, respectively, Temperature Programmed Desorption of NH_3 and H_2O adsorption isotherms at 313 K were carried out to highlight the implications of the *Si/Al* ratio and compensating cations on the CHA and LTA samples textural and adsorption properties.

2 OBJECTIVE OF THE THESIS

2.1 GENERAL OBJECTIVE

The main objective of this research is to analyze the influence of different features of cationic zeolite molecular sieve on its hydrothermal stability in typical conditions of natural gas drying by Temperature Swing Adsorption (TSA). The zeolite features to be assessed are the framework structure (CHA and LTA), the *Si/Al* ratio and the nature of the compensating cation.

2.2 SPECIFIC OBJECTIVES

The main objective of this thesis can be unveiled in 4 stages:

- Synthesize seven different cationic zeolite materials from two crystal structures (Chabazites and Linde Type A), with different compensations metals (Na and K) and *Si/Al* ratios (1, 2, 5).

- Develop lab-scale aging protocols (PAP-1 and PAP-2) that expose the materials to the operating conditions found in a TSA natural gas dehydration process.

- Perform a comprehensive set of physical-chemical characterization techniques in the pristine and aged absorbent samples.

- Measure water vapor adsorption isotherms in the pressure range from 0 to 70 mbar at 313 K for the pristine and aged samples.

2.3 THESIS CONTENTS

The next chapter (3) brings an introduction that revisited fundamental concepts regarding adsorption-based gas drying processes, molecular sieves and their hydrothermal stability. The chemicals and experimental techniques used in the thesis will be detailed in Chapter 4. The thesis results are disclosed in four sections of chapter 5. The first section will describe the proposed lab-scale aging protocol that mimics the hazardous conditions faced by the adsorbent material in a TSA drying process. The subsequent sections address the hydrothermal stability of a specific group of adsorbent materials. For last, a comparison between both cationic zeolite groups previous aged.

Section 5.1 brings the full characterization, before and after an aging laboratory protocol, of CHA zeolite with *Si/Al* ~ 2.0 in sodic (*Na*) form. First, this CHA cationic zeolite (S-CHA_C-SiAl2-Na) was submitted to a proposed Premature Aging Protocol – PAP-2 (a detailed explanation is found in **Chapter 4**, **Section 4.3**) during different aging times. The same sample was also submitted to another aging procedure, named as PAP-1, originally proposed by our research group in 2019 (Gomes Santiago et al., 2019). Both PAPs (PAP-1 and PAP-2) consist in exposing the samples to conditions found in real TSA cycles. Driven by the need of an aging protocol that only requires a small amount of sample, the thermal stress caused the exposition of the sample to high temperatures and the homogenization of the aged material, the new methodology (PAP-2) was validated against PAP-1 in this chapter. Adsorbent characterization and adsorption isotherms of probe gases and water vapor were performed before and after the two aging protocols to correlate observed changes in texture and adsorption performance with PAPs conditions.

In **Section 5.2**, CHA molecular sieves synthesized under different *Si/Al* ratios and compensating cations were investigated. Three cationic zeolites were studied with an intermediate (≈ 2.0) and a high (≈ 5.0) *Si/Al* ratios and two compensating cations (*Na* and *K*). The impact of hydrothermal aging in each of the samples was

analyzed by physical-chemical techniques, monitoring adsorption isotherms of probe molecules (N_2 and CO_2) and water vapor before and after the aging protocol.

Section 5.3 has a similar organization as **Section 5.2**, but with a different cationic zeolite, LTA. Four adsorbents were synthetized varying the *Si/Al* ratio (1, 2 and 5) and compensating cation (*Na* and *K*).

In **Section 5.4**, a comparison between the two aged cationic zeolites (CHA and LTA) is performed, focusing similar CHA x LTA materials, regarding the *Si/Al* ratio and compensating cation.

3 INTRODUCTION

3.1 NATURAL GAS

One of the main challenges of mankind is the ever-growing need for power generation. Since the first Industrial Revolution in the 1860's, energy supply for all activities of our lives has become essential (BPSTATS, 2019; VGB, 2020). Routine actions, such as communication, transportation, housing and manufacturing, all require directly or indirectly energy supply. To meet this demand, each country has diverse power generation sources; normally, the total amount of energy consumed is proportional to the Gross Domestic Products (IMF, 2019; OGJ, 2019). A mixed energy matrix, including oil, natural gas, hydroelectricity, renewable and nuclear sources, is believed to be the best way to improve the development.

In the last 20 years, the consumption of natural gas has increased more than 2% per year and its share in the world energy matrix was 19.3% in 1995; 20.4% in 2005; 21.9% in 2015 and 22.8% in 2018 (McKinsey & Company, 2019; OECD, 2020). It is therefore an outstanding energy source in the global scenario. The composition of NG produced from the reservoirs is variable, whether it is associated or non-associated gas in different sites around the globe. However, a reference composition considers the major presence of methane (> 85%, v/v), over ethane, propane and n-butane, in this order. There are also several undesired substances, such as carbon dioxide, water vapor, sulfur compounds and heavier hydrocarbons. The natural gas composition may vary from different reservoirs. Some important features of the main NG components are summarized in **Table 3.01**, where significant differences in properties may be appreciated among them. It is important to highlight that other impurities, such as mercury and mercaptans, must be conveniently handled to ensure transportation and combustion efficiency/safety and to prevent harmful effects for the environment (Baker & Lokhandwala, 2008; Getu et al., 2013; Kubesh et al., 1992; Malenshek & Olsen, 2009; Speight, 2019; Van Duc Long & Lee, 2013).

Table 3.01 - Natural gas components

Molecule	Chemical Formula	Molar Mass [$g\ mol^{-1}$]	Critical Kinetic Diameter [nm]
Methane	CH_4	16.04	0.38
Ethane	C_2H_6	30.07	0.44
Propane	C_3H_8	44.10	0.45
n-Heptane	C_7H_{16}	100.21	0.46
Carbon dioxide	CO_2	44.01	0.33
Nitrogen	N_2	28.01	0.36
Water	H_2O	18.01	0.26
Oxygen	O_2	16.00	0.34

Source: (Doetsch et al., 1974; Sircar, 2006; Theodore L. et al., 2017)

As a general rule, NG processing (**Figure 3.01**) starts with a volume expansion, which leads to a decrease in temperature and pressure by the Joule-Thomson effect (Marić, 2005). Therefore, a major fraction of the heavy hydrocarbons and moisture in the gas phase condenses and can be easily separated. The next step includes the removal of impurities, such as water vapor and carbon dioxide, to meet NG specifications. The presence of impurities may cause toxicity, corrosion of pipelines and equipment and reduced calorific power (Baghban et al., 2016; Speight, 2019). CO_2 removal is usually carried out by chemical absorption in aqueous amine solutions (Araújo et al., 2017) and/or membrane selective permeation (Mutch et al., 2019). Water removal (drying step) is performed by adsorption; the gas flows through a column filled with a hydrophilic material (usually a molecular sieve) that is able to capture the water vapor molecules present in the gas (Farag et al., 2011; Rezvani & Fatemi, 2020; Santos et al., 2017). Natural gas drying plays a key role for the adequate performance of subsequent operations. To obtain an "in spec" product, the three following aspects should be taken into account:

4. For sufficiently low temperatures, water in gas phase may form hydrates that encapsule hydrocarbons ($C_nH_{2n} + 2 \times H_2O$), in a crystalline framework. Newly formed crystals might cause obstruction of pipelines

and equipment (Talaghat & Khodaverdilo, 2019). It is important to note that the crystals formation can be caused by accelerated flows of the gas, induced by large differences in pressures (Hammerschmidt, 1934). There is also a safety issue regarding the hydrates formation that would block pipelines and have the potential for explosive dissociation reactions (Speight, 2019);

5. The presence of water decreases the calorific power of Natural Gas and thus the combustion efficiency and delivered power (Speight, 2019);

6. Water associated with carbon dioxide and hydrogen sulfide may lead to corrosion of equipment and pipelines (Speight, 2019).

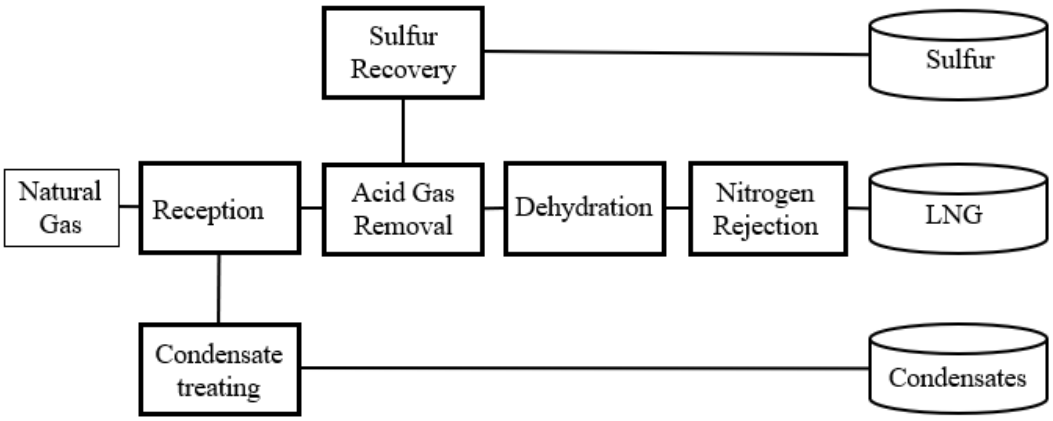

Figure 3.01. Simplified natural gas industrial processing

Source: adapted from (Speight, 2019)

3.2 FUNDAMENTALS OF ADSORPTION

Adsorption is defined as a spontaneous interfacial phenomenon that drive molecules of a free fluid (liquid or gas) to concentrate (adsorbate) on the interface, usually a fluid-solid interface, in which case the solid is named the adsorbent (Ruthven, 1984). Desorption is the opposite process, in other words, the dispersion of molecules that were previously attached to the surface by a change in pressure, temperature or

chemical potential. According to the kind of interaction between adsorbent and adsorbate, there may be physical adsorption (Physisorption) and chemical adsorption (Chemisorption). Physisorption involves weak interactions, such as van der Waals forces or electrostatic interactions. It releases low heats (comparable to heat in phase transitions), is significant at low temperatures and may take place in multiple adsorbate layers. Chemisorption, by contrast, is characterized by strong covalent interactions, with the formation of a single monolayer. Besides that, chemical adsorption may present in a broad range of heats of adsorption comparable to the ones shown by chemical reactions (Ruthven, 1984). When an adsorption-driven cyclic (adsorption/desorption) process is analyzed, several aspects should be taken in account, such as, adsorbate/adsorbent interactions, working capacity, adsorption reversibility and kinetics, heats of adsorption, selectivity for the target adsorbate among other factors (Ruthven, 1984). Hence, physisorption is the preferred choice for cyclic processes such as TSA (temperature swing adsorption) and PSA (pressure swing adsorption) due to the reversibility and low energy penalty (as compared to chemisorption).

In physisorption, the thermodynamic equilibrium is usually expressed by relating the adsorbed phase concentration (mols per unit mass adsorbent) with the solute concentration in the fluid phase. At a constant temperature, this equilibrium relationship is known as adsorption isotherm. The International Union of Pure and Applied Chemistry (IUPAC) has classified isotherms of condensable vapors (such as N_2 at 77K) into 6 types (**Figure 3.02**), which reveal important information about adsorbate/adsorbent interaction and the adsorbent pore structure (Thommes et al., 2015). Type I is typical of microporous adsorbent with strong adsorbate/adsorbent interaction. The types II, IV and VI isotherms also suggest strong adsorbate/adsorbent interactions, but the inflection point(s) in the curve, as pressure increases, is (are) indicative of larger pores where the adsorbate may condense (upon pressurization) and evaporate (upon depressurization) at different partial pressures, leading to the hysteresis observed in type IV(a). The other types of isotherms (III and V) are found for solids with a weak adsorbate/adsorbent interaction, which are thus not suitable for separation/purification purposes. For the purpose of gas drying, adsorbents will usually exhibit type I water isotherms, in the case of molecular sieves, or type II/IV, if they have a broad pore size distribution. The latter isotherms may also be found for

microporous solids shaped into pellets/beads. In type I isotherms, it is likely that water adsorption takes place as a monolayer of adsorbate or not enough adsorbed layers to allow for condensation, whereas in larger pores (type II and IV isotherms), multiple layers of adsorbed water confined in a sufficiently large pore may result in clustering or condensation.

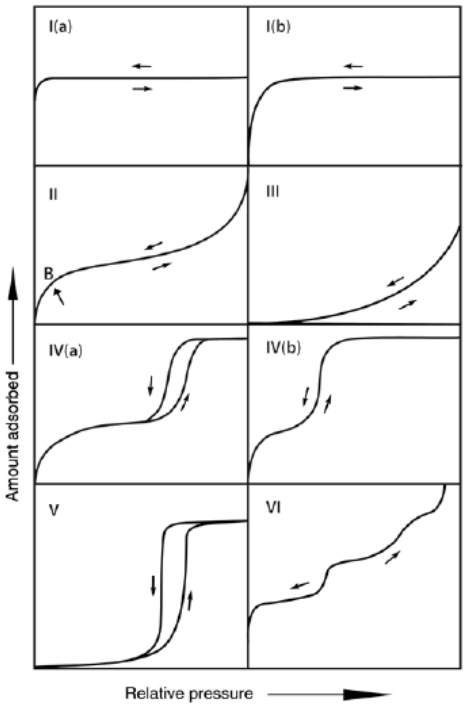

Figure 3.02. Classification of vapor adsorption isotherms proposed by IUPAC, concerning the relative pressure and adsorbed mass

Source: (Thommes et al., 2015)

To describe adsorption equilibrium as a mono or multi-layer phenomenon, some models have been proposed in the literature (**Table 3.02**). The simplest model is the Henry's Law, which states that the adsorbed concentration is linearly proportional to the fluid phase concentration. It strictly applies only in sufficiently low adsorbate loadings, beyond which adsorption equilibrium follows a non-linear behavior (Tóth, 2003). The models from Toth and Freundlich are empirical and thermodynamically inconsistent. When the pressure tends to zero, both models do not reduce to the Henry's Law (MOGHIMI et al., 2020; Tóth, 2003). The Langmuir Model (LM) (**Table 3.02**), formerly proposed for monolayer adsorption on a homogeneous adsorbent surface

(Langmuir, 1918), is a flexible mathematical equation that may satisfactorily reproduce type I isotherms. The LM is generally able to fit experimental data from microporous materials in a wide range of temperatures and pressures. Regarding the parameters used in LM, 'q_{max}' stands for the maximum adsorbed concentration and 'b' accounts for the adsorbent/adsorbate interaction. As an extension to the LM, the Sips Model (**Table 3.02**), takes into account an additional 'n' parameter, which is related to the degree of heterogeneity of the adsorbent surface (Myers & Prausnitz, 1965). The Brunauer-Emmett-Teller Model (BET) (**Table 3.02**) considers a homogeneous surface, onto which multiple adsorbed layers may build up as pressure increases. Apart from the gas molecules in the adsorbed first (mono)layer, the subsequent layers behave as a saturated liquid. The BET parameters are "n_m", which is the adsorbed concentration in the monolayer and "C", which is exponentially related to E_1 (the heat of adsorption in the first layer) (Brunauer et al., 1940). The Aranovich-Donohue Model (**Table 3.02**) considers a multi-layer adsorption and has been frequently used to reproduce type II/IV water isotherms. It is the product of two terms, the first accounting for the monolayer formation as a Sips Model equation. The second term refers to the subsequent layers, taking in account the saturation pressure "P_o" and an empirical parameter "e" with no precise physical meaning.

Table 3.02. Adsorption models

Isotherm Model	Equation		Reference
Langmuir – LM	$q_{eq} = \frac{q_{máx} \cdot b \cdot P}{1 + b \cdot P}$	**Eq. 3.01**	(Langmuir, 1918)
Sips – SM	$q_{eq} = \frac{q_{máx} \cdot (b \cdot P)^n}{1 + (b \cdot P)^n}$	**Eq. 3.02**	(Myers & Prausnitz, 1965)
Brunauer-Emmett-Teller – BET	$q_{eq} = \frac{\left(P/P_\circ\right)}{\left[\frac{1}{n_m C} + \left(\frac{C-1}{n_m C}\right)\left(P/P_\circ\right)\right] \cdot \left[1 - \left(P/P_\circ\right)\right]}$	**Eq. 3.03**	(Brunauer et al., 1940)
Aranovich-Donohue –	$q_{eq} = \frac{q_{máx} \cdot (b \cdot P)^n}{1 + (b \cdot P)^n} \cdot \frac{1}{1 - \left(\frac{P_o}{P}\right)^e}$	**Eq. 3.04**	(Aranovich & Donohue,

ADM			1995)

Cyclic adsorption processes were developed to separate gas mixtures, while allowing for the regeneration and reuse of the adsorbent by swings in pressure (Pressure Swing Adsorption – PSA) and/or in temperature (Temperature Swing Adsorption – TSA). Desorbing solutes by PSA or VSA has advantages and disadvantages in terms of cycle time, energy expenditure and adsorbent lifetime (Bastos-Neto et al., 2020; Cavenati et al., 2006). |Temperature swings are preferentially chosen when there is a strong adsorbent-adsorbate interaction, such as in the case of water adsorption in cationic zeolites. However, one of the huge drawbacks in TSA are related to the kinetics of heat transfer and adsorbents deactivation (Gomes Santiago et al., 2019). Some of the causes of the material deactivation are the carbon deposition (coke formation) and the crystal structure degradation (Barry Crittenden, 1998).

3.3 ZEOLITES

Zeolites are nanoporous materials, also known as molecular sieves due to their unique pore size(s) defined by their crystalline structure, which allows smaller molecules (such as water) to be hosted in the internal cages and larger molecules to be excluded. Therefore, this sieving effect may lead to high selectivity. Zeolites are composed of TO_4 as the Primary Building Unit (PBU) tetrahedra (**Figure 3.03**), where *T* is usually *Si* or Al. The *T* element is in the center and the four vertices have oxygen atom, which are shared with the neighboring tetrahedra, to give rise to a crystalline structure comprising pores and cavities. The exchange of the *Si* atom for other divalent, trivalent or tetravalent ions leads to a variety of zeolite structures. Different zeolitic materials are generated by the diverse charges (A. Louis Allred, 1961) and ionic radius (Shannon, 1976) of different cations that are insert in the structure.

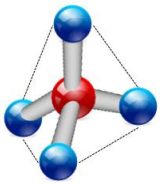

Figure 3.03. Tridimensional tetrahedral structure (TO_4) of zeolites
[Blue spheres = *O*; Red spheres = *T* element]

When the *T* atom is only *Si* (or another tetravalent metal), the structure is neutral; however, if it is *Al*, there is a negative charge in AlO_4^-, which must be compensated by a cation (thus generating cationic zeolites) or by a proton (H^+), giving rise to protonic zeolites. Considering the *Si/Al* ratio and the compensating metal cations in the structure, the general molecular formula of cationic zeolites is $M_{x/n}$ $[(AlO_2)_x (SiO_2)_y]$ w H_2O; where, *M* stands for the compensating cation; *n* is the valence of the cation; the *Si/Al* ratio is *y* divided by *x*; *w* is the number of water molecules in each crystalline cell (Vigil de la Villa Mencía et al., 2020). The hydrothermal synthesis is the most common route to synthesize zeolites, using water as solvent. In addition to the sources of silicon (and aluminum), other chemicals may be required in the synthesis, such as mineralizing Agents (MA), Structure-Directing Agents (SDA) and water. A typical zeolite synthesis consists of three steps: Induction Period, defined as the time from the moment that all reagents reach the reaction temperature until the onset of crystal formation; Nucleation, which corresponds to the structural organization of the zeolite, establishing its typical structure periodicity; and the Crystal Growth, that has similar concepts to those of the nucleation stage (Cundy & Cox, 2005; Yu, 2007).

Two small-pore cationic zeolites (Linde Type A – LTA and Chabazite – CHA), both in the sodium and potassium forms, are commonly indicated for water adsorption. LTA has a cubic zeolite structure (8 MR) with pore dimensions of 0.4 x 0.4 nm and a cavity (alpha super cage) size of 1.14 nm (Ch. Baerlocher, Lynne B. McCusker, 2007; L. Liu et al., 2020; Wang, 2020). The crystals form a cubic structure, *d4r*, with a total area of 0.245 nm² and a Framework Density (FD) of 12.9 *T* per nm³ (Ch. Baerlocher, Lynne B. McCusker, 2007). LTA (**Figure 3.04**) is generally available with *Si/Al* ratio equal to one and in sodium form, in which case its molecular formula is $|Na_{12}(H_2O)_{27}|_8$ $[Al_{12}Si_{12}O_{48}]_8$, however the sodium may be exchanged for other cations,

such as, *Ag, Ca, K, Na, NH_4, Li* and *Mg* (Cejka et al., 2007). This is why most of the produced Na-LTA is applied in the detergent industry to remove water hardness. In the case of sodic LTA, Na atoms are localized in three different sites I, II and III, all of them (approximately 12 *Na* cations) in the vicinity of the α cages. Sites I are in the center of the 6-membered rings separating α and β cages. Sites II are in the center of the 8-membered rings separating α cages. Lastly, sites III are located randomly in the center of the 4-membered rings (Busca, 2017a). LTA has an impressive dehydration capacity, due to the strong hydrophilic character of the framework and not only the similarity between water molecular kinetic diameter and the pore size (**Table 3.03**) (Cejka et al., 2007). CHA (**Figure 3.05**) is a molecular sieve that can be found in mineral deposits or obtained in pure form by synthetic routes. It is a small-pore zeolite with 8-membered ring pores (0.38 x 0.38 nm) connecting channels in a rhombohedral crystal structure (Dent & Smith, 1958; Mintova & Barrier, 2016). CHA framework may easily host and exchange cations, such as, *Tl, K, Ag, Rb, Na, Ba, Sr, Ca* and *Li* (Capasso et al., 2005, 2007) and these cations may be located at three possible sites (I, II and III) inside the structure. Sites I is located in the center of the hexagonal prisms with a possible octahedral coordination. Sites II is located in the center of 6-membered rings that connect the CHA cavities in a planar layer with a 3-fold coordination. Sites III is located in the center of 8-membered ring with planar 8-fold coordination (Koningsveld, 2007; Mortier et al., 1977). There are six different spots in three different sites per unit cell, one site I, two sites II and three sites III, however sites I and II cannot be occupied simultaneously, due to the repulsion effect among the cations. The synthetic form of CHA has a framework density of 14.5 *T* atoms per nm^3 (slightly higher than that of LTA) (Mintova & Barrier, 2016), which is related to the material strength and stability.

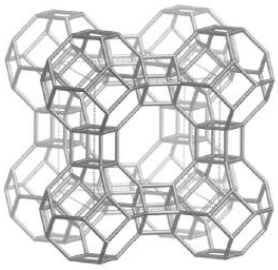

Figure 3.04. Linde Type A (LTA)

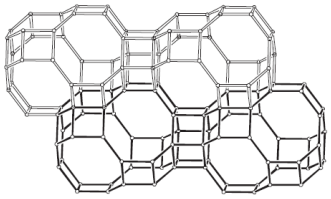

Figure 3.05. Chabazite (CHA)

Source: (Ch. Baerlocher, Lynne B. McCusker, 2007; Koningsveld, 2007)

The main features in a cationic zeolite that are likely to impact its potential to adsorb water and its hydrothermal stability are interconnected as depicted in **Figure 3.06**. In the following, some aspects will be better detailed.

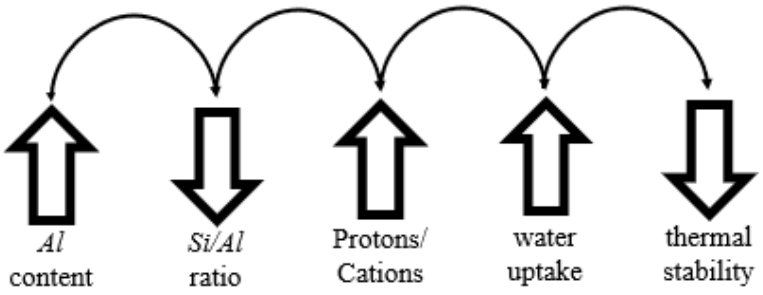

Figure 3.06. Interplay of properties of cationic zeolites related to water uptake and hydrothermal stability

1. *Al* Content: The total amount is defined by the Rule of Löewenstein (Loewenstein, 1954) that forbids – *Al* – *O* – *Al* – bonds. Hence, the *Si/Al* ratio is never less than 1. *Al* atoms can be in PBUs or outside the crystal structure, as Extra Framework Aluminum (EFAl). The EFALs structures are not precisely known, however they are associated with aluminum and oxyaluminum cations, such as, AlO^{+}, $Al(OH)^{2+}$,Al^{3+} (Bhering et al., 2003). Even at the room temperature, *Al* coordination fluctuates from tetrahedral to octahedral phases (Xu et al., 2006).

   In protonic zeolites, the *Al* atoms belonging to the AlO_4 tetrahedra that comprise the crystal structure are responsible for the acidity in the form of Brönsted Acid Sites – BAS (**Figure 3.07**). Regarding the acidity in zeolites, Johannes Nicolaus Brönsted (1879 – 1947) and Thomas Martin Lowry (1874 – 1936) introduced an acid-base definition, both in 1923 (Brönsted, 1923; Lowry, 1923). The theory states that an acid is any compound that can transfer a proton to another compound, and a base is the one that can accept the proton. In zeolites, the BAS are composed by

a proton (H^+) attracted to a negative framework oxygen, which is linked to an *Al* atom and one *Si* atom. The three referenced bonds (*O – H, O – Al, O – Si*) are covalent bonds ruled by electrostatic interactions (**Figure 3.07**). As a result, these *O* atoms have a similar coordination as found in hydronium cations (H_3O^+) and the bond (*O – H*) forms the well-known bridged hydroxyl or the BAS in protonic zeolites frameworks (Boronat & Corma, 2019; Busca, 2017b). The bridged hydroxyls are the strongest acid sites in zeolite frameworks (Phung & Busca, 2015).In the case of cationic zeolites this negative charge is balanced by a compensating metal, commonly an alkali or an earth alkali, hence the presence of BAS is supposedly reduced to zero.

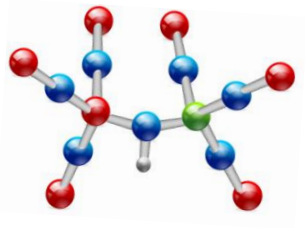

Figure 3.07. Brönsted acid sites in protonic zeolites [blue spheres = *O*; green sphere = *Al*; red spheres = *Si*; white sphere = *H*].

The amount of aluminum not located in the framework of zeolites (EFAl) also impacts on the material acidity. Lewis's acidity was originally defined by Gilbert Newton Lewis in 1916 (Lewis, 1916), for acid and base substances. In both cases, it is characterized by a chemical element which is able to accept a pair of electrons, as acid, or a chemical element able to donate a pair of electrons, as base. The EFAl acts as a Lewis acid site (M. C. Silaghi et al., 2014), because they are capable of accepting a pair of electrons. In addition, some polarization effects between Brönsted–Lowry and Lewis sites may enhance the total zeolitic acidity (Corma, 1995; Mota et al., 2004; Ribeiro et al., 1995). On the other hand, the excess EFAl may cause undesirable effects, such as pore blocking (M.-C. Silaghi et al., 2016).

2. Acidity: The Brönsted and Lewis Sites directly and/or indirectly provide the zeolite acidity. In protonic materials, higher aluminum content increases the concentration of bridged hydroxyls and hence the materials acidity. The maximum number of Brönsted active aluminum sites is the number of tetrahedral aluminums (Corma, 1995). In addition, investigations relating the porosity and the water vapor adsorption are being further studied, due to the BAS existence limited to the inner surface of the protonic adsorbents. The stabilization provided by the opposite wall of the zeolite cavities on BAS are a vital aspect to its equilibrium (Bevilacqua et al., 2006). Therefore, the acidity will probably be increased by a higher material porosity in the case of protonic materials. It is important to note that the presence of compensating cations may neutralize the total charge of the zeolite (cationic zeolites). Thus, BAS rarely occur in cationic zeolites, but Lewis's acid sites may occur due to structure defects or extra-framework (octahedral) aluminum (Ravi et al., 2020).

3. Water Affinity: H_2O molecules are incorporated in the framework of the cationic zeolites by two different ways: (1) extra-framework compensating cations are surrounded by oxygen atoms of the framework, which contributes to negative electric charges, generating strong interactions with water; associated with the hydration of the extra-framework cations (Busca, 2017b; Nachtigall et al., 2012); and (2) by weak bonds with the zeolite, upon pore/channel filling (Shim et al., 1999b). When the *Al* content increases in the zeolite framework, the total unbalanced (negative) charge increases, which raises the need of compensating cations in the framework to balance the charge (**Figure 3.06**). In addition, the adsorption water uptake is also impacted by the cation size, electronegativity and on the zeolite topology (Nachtigall et al., 2012). Regarding the location of water molecules in LTA structures with a *Si/Al* ratio up to 5, the β-cages are first occupied at low pressure. The water molecules in β-cages drops proportionally as compared to the water molecules hosted in the α-cages with increasing pressure (Perez-Carbajo et al., 2020). The LTA structure (**Figure 3.04**) in the sodium

form may accommodate 27 water molecules, a cluster of 20 molecules in α-cage, 4 water molecules in the β-cages and 3 molecules in the side faces (Jansen, 1998). Water molecules in CHA are spread over seven different sites in the PBU. The first site is exactly at the center of the 8-ring window, far from framework oxygens. The other six sites are inside the large cage, with a low occupancy and far from the framework oxygen atoms (Alberti et al., 1982).

4. Thermal Stability: One of the reasons that renders zeolites a widespread use in industry is their high thermal stability (Mintova & Barrier, 2016). When the *Al* content decreases, there is a high density of *Si – O – Si* bonds, which have pronounced temperature stability, and thus more energy is required to break these new bonds as compared to *Al – O – Si* bonds (Cruciani, 2006; Kerr, 1967).

5. Ion Exchange: The compensating cation to neutralize the negative charge in cationic zeolites brought about by the presence of *Al* in the framework, is generally Na^+, but it may be exchanged for other monovalent or divalent cations from the alkaline and earth alkaline group, respectively. For the same *Si/Al* ratio, according to the valence and size of the cation, water uptake may change with available pore space left in the cage for adsorption (Singh & Webley, 2005).

In summary, CHA and LTA cationic zeolite molecular sieves are one of the most suitable adsorbents for this gas drying, due to their high affinity for polar and polarizable molecules (Company, 2015; Kawai & Tsutsumi, 1992); relative hydrothermal stability and the pore opening of around 0.40 nm (Yan & Bein, 1992), which excludes most hydrocarbon molecules. The critical kinetic diameters of the most common molecules are compared, and the water molecule dimension is highlighted as the smallest one (**Table 3.03**). In addition, synthetized CHA zeolites have been reported as possessing the highest hydrothermal stability combined with a small-pore structure of all known zeolites (Cejka et al., 2007; Cruciani, 2006). On the other hand, LTA materials are one of the most widely used zeolites in industrial applications, particularly

as cation exchanger for water softening. Numerous advances in the synthesis and post-syntheses procedures have been reported in the literature to improve the target features of an adsorbent for a given application. Note that, in the case of CHA, it is mostly used from natural deposits which ordinarily contain a variety of different cations. Nevertheless, a better understanding about the interplay between key-features from cationic zeolite materials, such as, acidity, thermal stability and water uptake must be further investigated to guide the choice of zeolites to be applied in TSA dehydration processes.

Table 3.03. Gas molecules critical diameter

Gas Molecule	Critical Kinetic Diameter [nm]	Reference
H_2O	0.27	(Yan & Bein, 1992)
C_2H_2 (acetylene)	0.33	(L. Liu et al., 2020)
CO_2	0.33	(Kennedy & Tezel, 2018)
Ar	0.34	(Freeman et al., 2006)
O_2	0.35	(Fernández-Barquín et al., 2016)
H_2S	0.36	(Freeman et al., 2006)
N_2	0.36	(Kennedy & Tezel, 2018)
Kr	0.37	(Feng et al., 2016)
CH_4	0.38	(Kennedy & Tezel, 2018)
Xe	0.41	(Feng et al., 2016)
C_2H_4 (ethylene)	0.42	(L. Liu et al., 2020)
CH_3OH (methanol)	0.43	(Madani et al., 2015)
C_6H_{14} (n-hexane)	0.43	(Yan & Bein, 1992)
C_7H_{16} (n-heptane)	0.43	(Funke et al., 1996)
C_8H_{18} (isooctane)	0.62	(Funke et al., 1996)

4 EXPERIMENTAL

The experimental work in this thesis was carried out in four different research centers. The research centers and their acronyms are: *Laboratório de Pesquisa em Adsorção e Captura de CO_2 (LPACO2)* at the Federal University of *Ceará* (Brazil); the group on *Nuevos Materiales Inorgánicos (NMI)* at the University of Málaga (Spain); the *Instituto de Tecnología Química (ITQ)* at the Polytechnic University of *València* (Spain) and the *Laboratório de Adsorção e Catálise Aplicada (LACAp)* at the Federal University of *São Carlos* (Brazil). In addition, the CHA sample in *Na* form with a *Si/Al* ratio of 2 was synthetized by Dr. *Ranjeet Singh* at the University of Melbourne (Australia) and kindly donated for this research.

4.1 ADSORBENT: MATERIALS AND SYNTHESES

Seven zeolite samples were synthesized in this thesis. The following chemicals were used for the syntheses performed at ITQ:

- *CBV500,* supplied by Zeolyst® (CAS. 1318-02-1);
- *KOH* 90%, supplied by PanReac AppliChem® (CAS. 1310-58-3);
- Sodium Silicate Solution 1.5 S.G. (SSS), supplied by Fisher Scientific® (CAS. 1344-09-8);
- Sodium Aluminate Pure (SAP), supplied by Carlo Erba® (CAS. 11138-49-1);
- Sodium Aluminate Solution (SAS), supplied by Süd-Chemie (CAS 11138-49-1);
- Ludox AS-40, supplied by Sigma-Aldrich® (CAS. 7631-86-9);
- Tetramethyl-ammonium hydroxide 25 wt.% (TMAOH), supplied by Sigma-Aldrich (CAS. 79-59-2);
- Diethyldimethyl-ammonium hydroxide 20 wt.% (DEDMAOH), supplied by Sigma-Aldrich® (CAS. 95500-19-9);
- Tetraethyl-ammonium hydroxide 35 wt.% (TEAOH), supplied by Sigma-Aldrich® (CAS. 77-98-5);

- Aluminium Isopropoxide ≥ 98 wt.% (IPA), supplied by Aldrich® (CAS. 555-31-7);
- Tetramethyl-ammonium chloride ≥ 97 wt.% (TMACl), supplied by Sigma-Aldrich® (CAS.75-57-0);
- *NaCl* Synthetic Grade, supplied by Scharcau® (CAS. 7647-14-5);
- 1-Adamantamine 97%, supplied by Sigma-Aldrich® (CAS. 768-94-5);
- Potassium carbonate 99.99%, supplied by Sigma-Aldrich® (CAS. 584-08-7);
- Chloroform ≥ 99.8%, supplied by Sigma-Aldrich® (CAS. 67-66-3);
- Methyl iodide ≥ 99.0%, supplied by Sigma-Aldrich® (CAS. 74-88-4).

At LACAp, zeolite LTA was synthesized using the following reagents:

- Sodium hydroxide ≥ 99.0%, supplied by Fisher Scientific® (CAS. 1310-73-2);
- Sodium aluminate (NaO_2 : Al_2O_3 : 3 H_2O), supplied by Fisher Scientific® (CAS. 11138-49-1);
- Sodium metasilicate (Na_2SiO_3 : 5 H_2O), supplied by Fisher Scientific® (CAS. 10213-79-3).

At NMI, ion-exchange procedures were carried out using *KCl* ≥ 99.0% supplied by Sigma-Aldrich® (CAS. 7447-40-7). In addition, a Chabazite sample was synthetized by Dr. *Ranjeet Singh* with *Si/Al* ratio of approximately 2 at the Clean Energy Laboratory – CEL in the University of Melbourne (Australia).

For the aging protocols carried out at LPACO2, the following chemicals and gases were used:

- Heptane HPLC grade ≥ 99.0% (CAS. 142-82-5), supplied by Sigma-Aldrich®;
- CO_2 99.800, supplied by White Martins Praxair®;
- CH_4 99.996, supplied by White Martins Praxair®;
- Deionized water.

The hydrothermal routes to synthetize zeolitic materials involve the choice of silicon and aluminum sources. Furthermore, the nature of the M cation to compensate the negative charge brought about by the Al content plays a key role in the characteristics of the final zeolite. A Mineralizing Agent (MA) is essential to bring the framework constituent elements (*Si, Al, M*) from the amorphous gel phase to a crystalline phase. The Structure Directing Agent (SDA) works as a template, leading the synthesis to a specific crystalline arrangement. In addition, temperature and pressure conditions are essential to define the shape and size of the crystals. A summary of all adsorbent samples investigated in this thesis is shown in **Table 4.01**. In the materials labels, the prefix (S) indicates that the sample is homemade, *i.e.*, not commercialized, and the subscript letter ($_C$), next to the zeolite structure, indicates that the material is in the crystal form. All syntheses procedures used in this work are described in the following sections.

Table 4.01. Summary of the zeolite samples and their labels

	Material Description			Label
	Zeolite Structure	*Si/Al* Theoretical	Compensating Cation	
1	LTA	1.0	*Na*	S-LTA$_C$-SiAl1-Na
2	LTA	1.0	*K*	S-LTA$_C$-SiAl1-K
3	LTA	2.0	*Na*	S-LTA$_C$-SiAl2-Na
4	LTA	5.0	*Na*	S-LTA$_C$-SiAl5-Na
5	CHA	2.0	*K*	S-CHA$_C$-SiAl2-K
6	CHA	2.0	*Na*	S-CHA$_C$-SiAl2-Na
7	CHA	5.0	*Na*	S-CHA$_C$-SiAl5-Na

1. Synthesis of LTA (LACAp, UFSCar) with *Si/Al* ratio of approximately 1.0 in Na form (Mintova & Barrier, 2016).

Initially, 0.723 g Sodium Hydroxide were dissolved in 80 mL H_2O under magnetic stirring for 20 minutes. Then, 8.258 g Sodium Aluminate were added to half the volume of the previous solution and 15.480 g Sodium Metasilicate were added to the other half. Both solutions were stirred by mechanical agitation for 1 hour at 27 °C.

Then, one solution was added to the other dropwise. The final gel composition was 3.165 Na_2O : 1.000 Al_2O_3 : 1.926 SiO_2 : 128.000 H_2O. The mixture was homogenized by mechanical agitation for 20 minutes and left to stand in an oven for 4 hours (preheated at 373.15 K) to allow the crystals to precipitate. The solids were separated by vacuum filtration, washed with distilled water and the filtrate pH was verified until it reached neutrality. The obtained solid mass in each synthesis batch was approximately 10.00 g, which means a total yield of 10% (comparing the mass of the synthesis gel to that of the obtained solid).

2. Ion exchange in LTA (NMI, Malaga Univ) with *Si/Al* ratio of approximately 1.0 to replace *Na* for *K* as the compensating metal

The synthesis procedure to obtain LTA with *Si/Al* ratio 1 in sodium form is fully described above. The exchange of Na for K was carried out according to the following procedure (Moura et al., 2016). First, *KCl* was dissolved in deionized water and stirred by magnetic agitation for 30 minutes. Then, Na-LTA was added to the salt solution. The suspension was agitated for 24 hours followed by the separation of solids by vacuum filtration. This procedure (immersion in KCl solution followed by vacuum filtration) was repeated 4 times, always with a freshly prepared salt solution. The expected solid composition is 1.000 SiO_2 : 0.601 Al_2O_3 : 0.408 K_2O : 0.264 CaO : 1.996 H_2O.

3. Synthesis of LTA (ITQ-UPV) with *Si/Al* ratio of approximately 2.0 in Na form (Wadlinger et al., 1968).

First, 3.080 g SAS were diluted in 13.600 g H_2O in a polypropylene bottle under magnetic stirring for 20 minutes. Then, 28.160 g TMAOH were dissolved in 14.660 g H_2O and the solution was stirred magnetically for 20 minutes. These two previously prepared solutions were mixed and stirred by magnetic agitation for 20 minutes. Thereafter, 14.800 g Ludox-AS-40 were added and stirred for 60 minutes. The obtained solution was aged in a silicon bath at 27 °C for 24 hours. Then, the synthesis gel was left to crystallize in an oven (preheated at 373.15 K) for 28 hours inside a polypropylene bottle. The solids were separated by vacuum filtration, washed with

distilled water and the filtrate pH was verified until it reached neutrality. The final synthesis gel composition was 1.190 Na_2O : 2.370 $(TMA)_2O$: 1.000 Al_2O_3 : 6.000 SiO_2 : 200.000 H_2O. The obtained solid mass in each synthesis batch was around 6.50 g, which means a yield of 10% (comparing the mass of the synthesis gel to that of the obtained solid).

4. Synthesis of LTA (ITQ-UPV) with *Si/Al* ratio of approximately 5.0 in Na form (Moscoso & Lewis, 2003).

First, 12.000 g TEAOH, 11.400 g DEDMAOH and 1.960 g IPA were added to a plastic beaker. The mixture was stirred under magnetic agitation for 30 minutes. Then, 14.200 g Ludox-AS-40 were added to the solution under mechanical agitation for 1 hour. The mixture was transferred to a polypropylene bottle and stood in an oven for 24 hours (preheated at 373.15 K) to allow for a pre-crystallization step. Then, after this solution was cooled down, 0.562 g TMACl, 0.298 g NaCl and 4.026 g water were added. The mixture was stirred for 40 minutes and transferred to two teflon-lined autoclaves to allow for crystallization in an oven for 3 weeks (preheated at 373.15 K). The solids were separated by vacuum filtration, washed with distilled water and the filtrate pH was verified until it reached neutrality. The final synthesis gel composition was 19.700 SiO_2 : 1.000 Al_2O_3 : 6.000 TEAOH : 4.000 DEDMAOH : 1.000 TMACl : 1.000 NaCl : 342.000 H_2O. The obtained solid mass in each synthesis batch was around 2.10 g, which means a yield of 5% (comparing the mass of the synthesis gel to that of the obtained solid).

5. Synthesis of CHA (ITQ-UPV) with *Si/Al* ratio of approximately 2.0 in potassium form (Bourgogne et al., 1985).

1.420 g KOH were dissolved in 21.300 g H_2O in a polypropylene bottle. The solution was homogenized by magnetic agitation for 20 minutes. Then, 2.500 g CBV500 were added to the solution and stirred for 30 minutes. Thereafter, the solution stood in an oven for 2 days (preheated at 373.15 K) to allow for crystallization. The solids were separated by vacuum filtration, washed with distilled water and the filtrate pH was verified until it reached neutrality. The final synthesis gel composition was

0.170 Na_2O : 2.000 K_2O : 1.000 Al_2O_3 : 5.180 SiO_2 : 224.000 H_2O. The obtained solid mass in each synthesis batch was around 2.00 g, which means a yield of 10% (comparing the mass of the synthesis gel to that of the obtained solid).

6. Synthesis of CHA (ITQ-UPV) with *Si/Al* ratio of approximately 5.0 in sodium form (Zones, 1991).

The synthesis of CHA (Si/Al ~ 5) requires an Organic Structure Direct Agent – OSDA, NNN-trimethyl-1-adamantammonium (TMAda), which was synthesized in-house. First, 29.600 g 1-Adamantamine and 64 g Potassium Carbonate were mixed in 320 mL Chloroform under magnetic agitation for 30 minutes. Then, 75 g Methyl Iodide was added dropwise to the mixture under agitation in an ice bath. Thereafter, the solution remained under agitation for 5 days at room temperature. The precipitated solids were recovered by vacuum filtration and washed with diethyl ether, followed by extraction with chloroform. After the production of TMAda, CHA zeolite with Si/Al ratio of approximately 5.0 and in the sodium form was synthesized as follows. First, 11.490 g SSS, 0.900 g CBV500 and 1.600 TMAda were added to 22.800 g H_2O in a plastic beaker. Then, the solution was stirred by mechanical agitation for 2 hours and transferred to two teflon-lined autoclaves. The autoclaves were placed in an oven for 5 days (preheated at 408.15 K) to allow for crystallization. The solids were separated by vacuum filtration, washed with distilled water and the filtrate pH was verified until it reached neutrality. The final synthesis gel composition was 1.000 SiO_2 : 0.027 Al_2O_3 : 0.090 TMAda : 0.340 Na_2O : 25.000 H_2O. The obtained solid mass in each synthesis batch is around 0.350 g, which means a yield of 1% (comparing the mass of the synthesis gel to that of the obtained solid).

In addition to the six synthesis procedures described above, an additional CHA sample was also investigated in this thesis. It was synthetized at the University of Melbourne by Dr. Ranjeet Singh following the procedure described in (Gaffney & Coe, 1991). Briefly, aluminate hydroxide (BDH) was mixed to sodium hydroxide 97%, potassium hydroxide 85% and Tetramethylammonium hydroxide pentahydrated 97%. Then, the silica source (Ludox-LS-30, supplied by Aldrich) was added. The final synthesis gel has the composition: 0.16 $(TMA)_2O$: 6.67 Na_2O : 2.2 K_2O : 17.5 SiO_2 :

Al_2O_3 : 276 H_2O. The synthesis gel was placed in a propylene bottle inside a preheated oven at 358.15 K for 4 hours to allow for crystallization. The solids were separated by vacuum filtration, washed with distilled water and the filtrate pH was verified until it reached neutrality.

After the synthesis procedures described above, all samples underwent a calcination step at 823 K in air for 3 hours, in order to remove the remaining SDA. Samples were heated up to 623 K in a ramp of 2.2 °C min^{-1} and they were kept for two hours at this temperature. Then, they were further heated up to 823 K at a heating rate of 1.3 °C min^{-1} and remained in the final temperature for 3 hours. Furthermore, following the sample label (**Table 4.01**), a suffix indicates whether the sample is pristine (V) or aged (E) material (see **Table 4.02** for a detailed description). All aging protocols are described in **section 4.3**.

Table 4.02. Summary of the suffixes added to zeolite sample labels

	Sample State	Suffix
1	Pristine sample	-V
2	Sample aged by PAP-1 for35 cycles	-E35c
3	Sample aged by PAP-2 in a single sample-port for 20 days	-E20d
4	Sample aged by PAP-2 in a single sample-port for 30 days	-E30d
5	Sample aged by PAP-2 in a single sample-port for 45 days	-E45d
6	Sample aged by PAP-2 in a single sample-port for 60 days	-E60d
7	Sample aged by PAP-2 in a double sample-port for 30 days	-E30d*

4.2 SAMPLES CHARACTERIZATION AND ADSORPTION EXPERIMENTS

To analyze the modifications in the chemical composition, structure and adsorption properties of zeolite samples before and after undergoing an aging protocol, several techniques have been employed. To examine the crystallinity and deposition of substances on the adsorbent surface, X-rays techniques were applied: X-Ray

Photoelectron Spectroscopy (XPS), X-Ray Diffraction (XRD) and X-Ray Fluorescence (XRF). To obtain chemical composition, Inductively Coupled Plasma – Orbital Emission Spectroscopy (ICP-OES) and Elemental Analysis – C, H, N were performed. The thermal stability of the samples and morphology were examined by Differential Thermogravimetric Analysis/ Differential Scanning Calorimetry – Mass Spectrometry (DTA/DSC-MS) and Scanning Electron Microscopy (SEM), respectively. The general surface acidity, main elements bulk contributions and structure bonds were assessed by Temperature Programmed Desorption of NH_3 (TPD-NH3), Nuclear Magnetic Resonance (NMR) and Fourier Transform Infrared Spectroscopy (FT-IR), respectively. To assess the porous texture of samples, isotherms of typical probe gases (N_2 at 77 K and CO_2 at 273 K) were measured. The water vapor adsorption isotherms were carried out at 313 K for the pristine and aged adsorbents.

4.2.1 X-RAY DIFFRACTION – XRD

XRD technique is commonly used as a fingerprint technique of crystalline solids. The technique is based on the generation and emission of x-rays with wavelength in the range from 10 to 10^{-3} nm directly to the sample. Then, the x-rays diffracted by the solid are captured in well-known angles. The emission occurs in a period of a fraction of a rotation from 5 to 40 degrees that is the most significant range to zeolite materials. The crystallinity is estimated from the area under the main peaks from 20 to 32° of the diffractogram (2θ° x Intensity), which is a fingerprint of zeolitic structures. The experiments take only a few minutes and provide reliable results with straight-forward interpretation. Philips X'Pert Pro-MPD Powder Diffractometer, PANalytical®; MiniFlex 600 diffractometer Rigaku® and a Cubix PRO^{TM} (Series number: DY0822), PANalytical® were used in order to obtain the diffractograms.

4.2.2 X-RAY PHOTOELECTRON SPECTROSCOPY – XPS

The analyses were mainly used to observe the *Si/Al* variation in the external surface and the composition/oxidation state of elements. Spectra were recorded on a

Physical Electronic spectrometer (PHI Versa Probe II) using monochromatic Al Kα radiation (15 kV, 1486.6 eV), a dual beam charge neutralizer for analyzing the core-level signals of the elements of interest and a hemispherical multichannel detector. The samples spectra were recorded with a constant pass energy value at 29.35 eV and a beam diameter of 100 µm. Energy scale was calibrated using Cu 2p3/2, Ag 3d5/2, and Au 4f7/2 photoelectron lines at 932.7, 368.2, and 83.95 eV, respectively. Atomic concentration percentages of the characteristic elements were determined considering the corresponding area sensitivity factor for the different measured spectral regions.

4.2.3 NUCLEAR MAGNETIC RESONANCE – NMR

The technique does not use either x-rays or radioactive substances (Stepanov, 2016). NMR allows for the measurement of extraordinarily small differences in the element contents presented in the material bulk. The *Si/Al* ratio was also obtained with the combination of ^{29}Si and ^{27}Al magic-angle spinning in an AVANCEIII HD 600 (Bruker AXS) spectrometer. The *Si/Al* ratio estimated from NMR experiments considers five different environments and contributions from *Si* in the zeolite framework (Duer, 2001).

4.2.4 CHEMICAL ANALYSIS by INDUCTIVELY COUPLED PLASMA - OPTICAL EMISSION SPECTROMETRY – ICP-OES

The bulk concentration of *Si*, *Al*, *Na* and *K* in the samples was performed in an Agilent 715-ES^{TM}, Varian® instrument. Prior to the readings, the sample is dissolved in an acidic medium. Then, the sample is ionized y an argon torch at around 10,000 °C. The emitted light by the energized atoms dislocation is retrieved and associated to an element.

4.2.5 CHEMICAL ANALYSIS by X-RAY FLUORESCENCE SPECTROSCOPY – XRF

From the bombarding of high-energy x-rays to a solid material by a UniQuant^{TM}, Thermo Fisher Scientific®, the emitted energy from the relaxation process is retrieved and associated to a given element. In addition, the intensity of the emitted energy is related to quantitative amounts of each component. The technique was employed to assess the extent of cation exchange carried out in LTA with a *Si/Al* ratio of 1, from *Na* to *K*.

4.2.6 ELEMENTAL ANALYSIS (CHNS/O)

The combustion of the sample in a pure oxygen atmosphere releases gases, which are retrieved and associated to the contents of C, H, N, S and O in the sample bulk composition. In particular, the C content in the samples, before and after the exposure to the PAPs, is key to understanding the adsorbent aging. For these determinations, a Leco TruSpec Micro CHNSO elemental analyzer was used.

4.2.7 SCANNING ELECTRON MICROSCOPY – SEM

The material morphology is studied using the irradiation of high-energized and accelerated electrons into a sample in a ultra-high vacuum atmosphere. The electrons of the sample leave the surface and generate 3D images (Ruska, 1987), using a Magellan® 400 L FEI equipment. The main need of those analyzes comes from the fact that similar syntheses procedures can generate materials with different morphologies (Sharma et al., 2015).

4.2.8 FOURIER TRANSFORM INFRARED SPECTROSCOPY – FT-IR

Based on the absorption of bands in the infrared region related to the natural vibrational energy of stretching and bending of the chemical bonds present in the sample under analysis. This absorption promotes an increase in the amplitude of vibration of the bonds. The same type of bond in two different molecules shows different infrared spectra, because the chemical neighborhood influences the absorption and behave of the bond. The equipment used was a VERTEX 70V (Bruker®, UK).

4.2.9 TEMPERATURE PROGRAMMED DESORPTION OF NH_3 – TPD-NH3

To measure the total acidity of the samples (pristine and aged materials), Temperature Programmed Desorption of NH_3 was performed. Briefly, 80 mg of an adsorbent sample were treated by flowing helium (100 mL min^{-1}) and heating from room temperature up to 620 °C at a rate of 3 °C min^{-1}. Then, ammonia diluted in *He* flows through the sample at 100 °C until complete saturation as detected by a mass spectrometer detector. Finally, ammonia is desorbed, by switching the flow to *He* and heating the sample up to 800 °C at a rate of 10 ºC min^{-1}. The MS signal of ammonia being desorbed is recorded.

4.2.10 DIFFERENTIAL THERMOGRAVIMETRIC ANALYSIS/ DIFFERENTIAL SCANNING CALORIMETRY – MASS SPECTROMETRY – DTA/DSC-MS

The sample is submitted to a thermal cycle of heating against an inert reference sample, commonly alumina, which is submitted to the same conditions. Hence, the excess energy not related to the thermal cycle is captured, and then, associated to several effects. With these experiments, it is possible to observe the elements that volatize or decompose from the adsorbent with the increasing temperature. The equipment used was a Skimmer™ QMS STA 409 CD/403/5/G NETZSCH® and a TGA/DCS 851e (X-12Nb), MettlerToledo®.

4.2.11 ADSORPTION/DESORPTION ISOTHERMS OF PROBE GASES - TEXTURAL CHARACTERIZATION

By measuring adsorption isotherms of probe gases, equilibrium models can be used to estimate textural features of the adsorbent, such as pore volume and surface area. Although the concept of surface area does not strictly apply to tridimensional microporous crystalline structures like zeolites, it is a useful figure of merit to compare samples of the same nature that undergo changes in texture such as those expected to take place in hydrothermal aging. The kinetic diameter of the probe gas will determine whether these molecules access the micropores. The presence of dipole and/or quadrupole moments in the probe gas molecule may also affect physisorption, which should be taken into account in the evaluation of surface area and pore volumes (Thommes et al., 2015). We have used N_2 at 77 K and CO_2 at 273 K as probe molecules.

To estimate de apparent area, the BET equation (**4.03**) was applied in the linear range of the plot $(P/Po)/n[1-(P/Po)]$ vs P/P_0, that corresponds to the adsorption of a monolayer of the probe gas (Brunauer et al., 1938). (*P)* accounts for the vapor pressure, (P_0) is the saturation pressure of the gas at the experiment temperature, (n) is the number of adsorbed mols in equilibrium and (n_m) is the number of adsorbed mols in a monolayer. The BET model is usually applied at a low relative pressure range from 0.05 to 0.35 (Brunauer et al., 1940) (**Equation 4.01**). In **Equation 4.01**, the parameter (C) is associated with the adsorbate-adsorbent interaction (Brunauer et al., 1940) and must always be a positive value. The estimation of the apparent BET area comes from the number of mols adsorbed in a monolayer (n_m) (Sing, 2014) multiplied by the Avogadro Number (AN), $6.023 \cdot 10^{23}$ molecules/mol and (σ) is the cross section area (16.2 Å²) of the probe molecule, as shown in **Equation 4.02**.

$$\frac{\left(\frac{P}{P_\circ}\right)}{n\left[1-\left(\frac{P}{P_\circ}\right)\right]} = \frac{1}{n_m C} + \left(\frac{C-1}{n_m C}\right)\left(\frac{P}{P_\circ}\right) \quad \textbf{(Eq. 4.01)} \qquad A_{BET} = n_m \cdot \sigma \cdot AN$$

To estimate the total pore volume (V_P) (**Equation 4.03**), the total amount of gas adsorbed (n) at a relative pressure of 0.99 is multiplied by the molar mass of the gas (*MM*) and divided by density of the adsorbed (ρ), considering the temperature and pressure conditions. At relative pressure of 0.99, it is assumed that all pores are filled with liquid adsorbate (Thommes et al., 2015). Considering only the fraction of the pores that corresponds to micropores (sizes smaller than 2 nm), a good estimation is proposed by the Dubinin-Radushkevich (DR) method (**Equation 4.04**) (Dubinin, M.M., Radushkevich, 1947). In **Equation 4.04**, (*D)* is an empirical constant, ($n_P(mic)$) is the number of mols adsorbed in the micropores and (*n)* is the total number of adsorbed mols. Note that the specific mass of probe gases in the porosity and microporosity calculations were 1.023 g cm^{-3} for CO_2 and 0.808 g cm^{-3} for N_2 (Salinas-Martinez de Lecea et al., 1988). Isotherms for both gases were measured in an Autosorb iQ 3 equipment (Quantachrome Instruments®, USA).

$$V_P = n_{N_2} \cdot \frac{MM}{\rho} \qquad \textbf{(Eq. 4.03)}$$

$$\log_{10}(n) = \log_{10}(n_P(mic)) - D \log_{10}{}^2(p_0/p) \qquad \textbf{(Eq. 4.04)}$$

4.2.12 WATER VAPOR ADSORPTION ISOTHERMS AT 313 K

Water vapor isotherms were measured by the gravimetric method using an Intelligent Gravimetric Analyzer - IGA 002 by Hiden® (UK). The equipment comprises an ultra-vacuum system, reaching pressures up to 10^{-7} bar, a microbalance with a stability of approximately 10^{-6} g, three pressure transducers in the ranges 0 - 10 mbar, 0 - 100 bar, 0 - 1 bar and a thermocouple located 5 mm from the sample holder to monitor the system temperature. In addition, a thermostatic bath is coupled to the system to maintain the desired temperature. Steam is statically generated at 328 K from deionized water contained in a small cylinder. Hence, the maximum vapor pressure inside the system is limited by water vapor pressure at the working temperature (328 K), i.e., 73.8 mbar (Dean, 1998). The required sample mass in a typical experiment is approximately 35 mg. Prior to the the isotherm measurement, zeolite samples are degassed at high vacuum (up to 10^{-7} mbar) and 573K for 10 hours. Then, water vapor is injected

automatically to keep the pressure inside the chamber from 0 up to 70 mbar. Buoyancy effects can be neglected in this system, since the working pressure range is low. The water vapor isothermdata was fit by the Aranovich-Donohue Model (**Equation 3.04**), which considers the Sips model for the monolayer formation (Aranovich & Donohue, 1995; Myers & Prausnitz, 1965).

4.3 PREMATURE AGING PROTOCOLS (PAPs)

The PAPs consist in exposing the zeolite sample to the conditions found in natural gas drying by TSA. These conditions include high temperatures (desorption step), high pressures (adsorption step) and the presence of humidity, heavy hydrocarbons, CH_4 and CO_2. On one hand, PAP-1 requires around 25 g of adsorbent for each run, whereas PAP-2 can be carried out with 1 g sample.

PAP-1 (**Figure 4.01**) is carried out in a high-pressure Parr vessel (Model 3848), by Parr Company® (USA).The steps of the protocol are reported elsewhere (Gomes Santiago et al., 2019) and briefly described below:

i. Place 25 g sample homogeneously in the bottom of the *Parr* vesse*l*;
ii. Add liquid *n*-heptane to the sample dropwise (0.6 mL per sample gram) and seal the vessel; A hydrocarbon of intermediate size (n-heptane) was chosen to represent all the heavy organic species present in natural gas. It is important to note that both quantities (water and *n*-heptane) are in excess to ensure the saturation of the sample.
iii. Humidify the sample by flowing through the Parr vessel a moist N_2 stream (20 mL s^{-1}) coming from a washing vessel for 24 hours;
iv. Pressurize the Parr vessel up to 30 bar pressure with a CO_2/CH_4 gas mixture with a molar rate of 1:4;
v. Then, heat the system up to 573 K at 5 K min^{-1}, subsequently, decrease the temperature down to 303 K at 0.75 K min^{-1};

The heating and cooling steps described in (v) were carried out successively 35 times, when the vessel was depressurized and opened to collect the aged sample for characterization. The suffix (E35c) is added to the label (**Table 4.01**) of samples that were aged for 35 cycles in PAP-1.

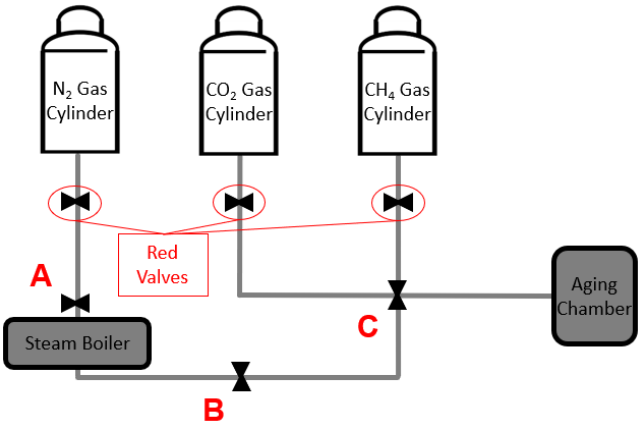

Figure 4.01. Premature Aging Protocol 1 (PAP-1) scheme (Gomes Santiago et al., 2019)

An alternative aging protocol (PAP-2) was proposed to handle small quantities of sample. It is carried out in the chamber of a gravimetric setup by Rubotherm® (Germany), to profit from the gas inlet/outlet piping and pressure/temperature control (weight was not monitored). It comprises the following steps:

i. Place 1.0 g sample in the hanging port inside the chamber;

ii. Degas the chamber and tubing at 10^{-3} mbar. Open valves in the sequence G, E, C, F, D for 1 hour. Then, close all valves in the opposite order;

vi. Connect a small cylinder (10 mL) to the sample chamber containing 1.0 mL n-heptane and 0.5 mL of water per gram sample. An intermediate hydrocarbon of intermediate size (n-heptane) was chosen to represent all the hydrocarbons in the structure heavy organic species present in natural gas. The water quantity was determined by taking into account two

contributions. First, the water vapor in equilibrium as a free vapor at the system volume (*Antoine* equation). Besides the water vapor in the volume, the average amount of water adsorbed in zeolites (Wang, 2020) was considered. Note that both added quantities (water and *n*-heptane) were calculated to ensure the sample saturation.

iii. Open the connection of the cylinder (10 mL) containing water/n-heptane (valve H) to allow vapors to be in contact with the sample and wait 24 hours for equilibrium to be reached. Then, close valve H;

iv. Pressurize the sample chamber up to 30 bar total pressure with a CO_2/CH_4 mixture (1:4 v/v) and wait for 1 hour. Open valves in the sequence D, C, F, Red Valves. Then, close in the opposite order;

v. Lastly, increase the system temperature up to 573 K at 5 K min^{-1} and leave it at the final temperature for 20, 30, 45 and 60 days.

PAP-2 was carried out in a single sample-port or in a dual sample-port (in order to age 2 samples simultaneously) (**Figure 4.03**). When a double sample-port was used in the aging process, the amounts of water and n-heptane were well-adjusted. In the PAP-2, the steps (*ii*) to (*v*) were repeated on every occasion that the *Aging Chamber* was opened. To the samples label (**Table 4.01**) a suffix was added to indicate that the sample was aged for *XX* days in PAP-2 in a single (E*XX*d) and dual (E*XX*d*) sample port (**Table 4.02**).

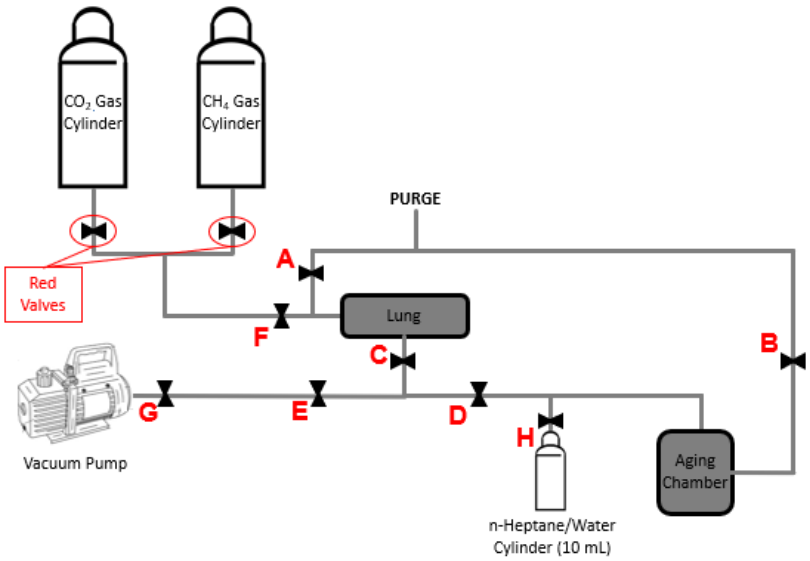

Figure 4.02. Premature Aging Protocol 2 (PAP-2) scheme

(a) **(b)**

Figure 4.03. Single (a) and dual (b) sample ports in the PAP-2

5 RESULTS AND DISCUSSIONS

In this chapter, Chapter 5 – Results and Discussions, the content will be divided in four sections. The first section comprises two sub-sections: a complete study of the proposed aging protocol for limited sample amount and a comparison between the proposed aging protocol and a similar one already reported in the literature. The second and third sections will focus on water adsorption and other properties before and after aging for CHA and LTA zeolites, respectively. Finally, in section four, a comparison between these two classes of materials is discussed.

5.1 PREMATURE AGING PROTOCOLS (PAPs)

5.1.1 PREMATURE AGING PROTOCOL 2 (PAP-2): CHABAZITE

The X-ray diffraction patterns of the pristine and aged CHA samples (**Figure 5.1.1**) are quite similar showing nearly the same peak locations, although with different magnitudes (Cejka et al., 1985; Dent & Smith, 1958). The main reflection peaks found in the angle range (2θ) from 20° to 32° (Miller Index), at 20.4 (2 0 -1), 22.9 (2 1 -1), 24.7 (2 1 1), 25.8 (2 0 -2) and 30.4° (2 2 -1) agree with the CHA pattern and the pristine (non-aged) sample. These peaks compose a fingerprint for the CHA crystal structure (Treacy & Higgins, 2007). The materials that were aged for 20, 30, 45 and 60 days by PAP-2 show similar diffractograms (**Figure 5.1.2**). However, the peaks intensity (y-axis) decreases with the aging period, which in turn is reflected in the materials crystallinity. The adsorbents crystallinities are found in **Table 5.1.1**. and they were calculated as the ratio between the sum of areas under the main peaks in the angle range (2θ) from 20° to 32° and the sum of areas under the same peaks for the pristine (non-aged) sample. Aged samples show decreasing crystallinity for longer aging period, although degradation levels off beyond 45 days of aging and the most pronounced deterioration occurs in the first 30 days.

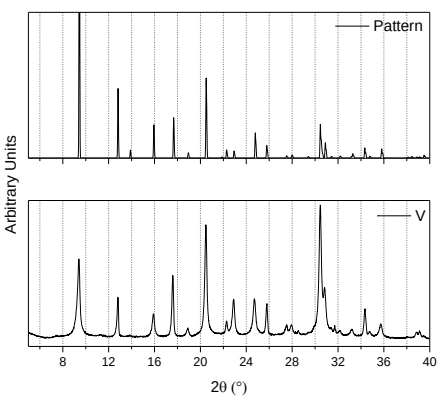

Source: (Cejka et al., 1985)

Figure 5.1.1. XRD diffractograms for pattern and homemade synthesized S-CHA$_C$-SiAl2-Na-V

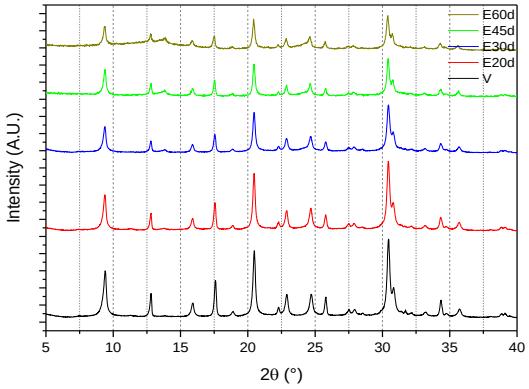

Figure 5.1.2. XRD diffractograms for S-CHAc-SiAl2-Na series aged by PAP-2

Table 5.1.1. Materials crystallinity from XRD diffractograms to S-CHAc-SiAl2-Na series aged by PAP-2

Sample	Crystallinity [%]
S-CHAc-SiAl2-Na-V	100
S-CHAc-SiAl2-Na-E20d	96.77
S-CHAc-SiAl2-Na-E30d	65.56
S-CHAc-SiAl2-Na-E45d	58.30
S-CHAc-SiAl2-Na-E60d	57.49

The main elements found in the pristine and aged materials by XPS are summarized in **Table 5.1.2** with their respective Binding Energies (BE)**.** In all samples, the BE accounting for C *1s* may be assigned to C – C and C – O bonds. The BE for *Si*2p and *Al2p* are typical of the tetrahedral coordination found in aluminosilicates; the BE of *O*1s also accounts for aluminosilicates (C.D. Wagner, W.M. Riggs, L.E. Davis, J.F. Moulder, 1979). The mass composition on the surface is shown as pie charts in **Figure 5.1.3.** Note that the *C* content varies erratically and no correlation with the progress of the aging protocol may be identified. Interestingly, the *Si/Al* ratio increased in the outer surface with the aging period by almost 30% (**Table 5.1.3**). The higher thermal resistance presented by *Si – O – Si* bonds also influence the increasing of the *Si* concentration in the surface (Cruciani, 2006; Kerr, 1967) (**Figure 5.1.3**). It may be the

case that carbon (either as adsorbed n-heptane or coke) deposits preferentially in the vicinity of *Al* centered tetrahedra, which are acid sites, thus covering these sites on the surface and increasing the *Si/Al* ratio (Moura et al., 2021). In addition, the migration of *Al* to the inner of the material occurs upon aging (Moura et al., 2021).

Table 5.1.2. Binding Energy values (eV) as Detected by XPS for the S-CHA$_C$-SiAl2-Na Series Aged by PAP-2

Sample	Si2p	Al2p	C1s	O1s	Na1s	K2p3/2
S-CHAc-SiAl2-Na-V	102.6	74.6	285.0 286.6	531.8	1072.7	294.6
S-CHAc-SiAl2-Na-E20d	102.6	74.3	284.8 286.6	531.8	1072.4	294.5
S-CHAc-SiAl2-Na-E30d	102.8	74.5	284.6 286.6	531.9	1072.6	294.6
S-CHAc-SiAl2-Na-E45d	102.7	74.4	284.8 286.1	531.9	1072.6	294.3
S-CHAc-SiAl2-Na-E60d	102.8	74.4	284.8 285.9	532.0	1072.6	294.4

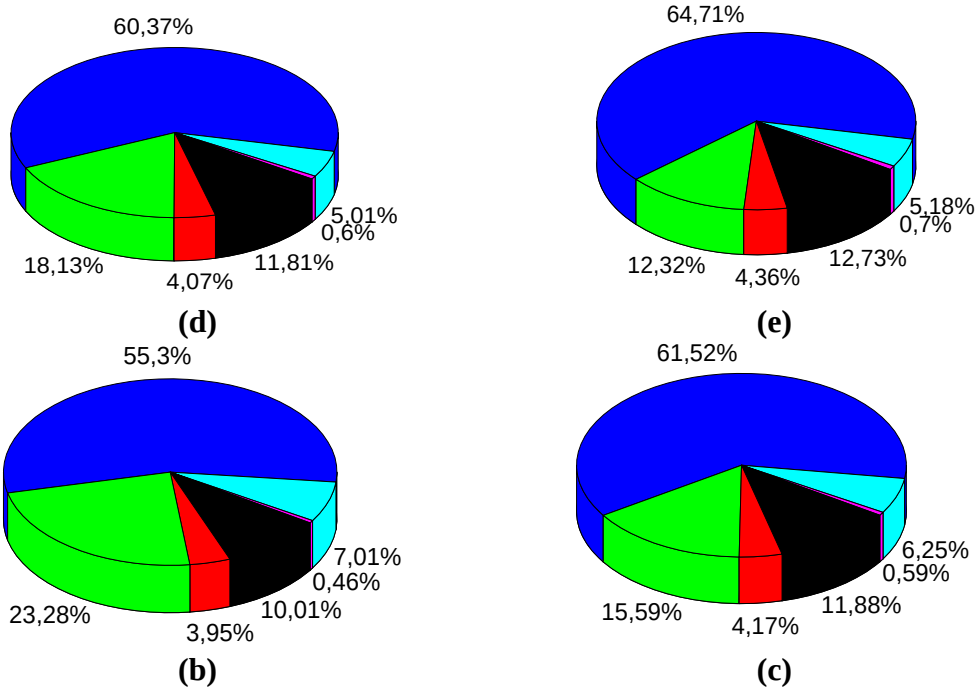

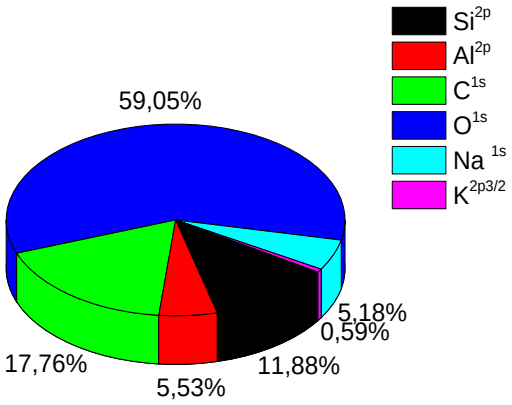

(a)

Figure 5.1.3. Chemical surface composition (% mass concentration) determined by XPS analysis for S-CHA$_C$-SiAl2-Na-V (a); S-CHA$_C$-SiAl2-Na-E20d (b); S-CHA$_C$-SiAl2-Na-V-E30d (c); S-CHA$_C$-SiAl2-Na-E45d (d); S-CHA$_C$-SiAl2-Na-E60d (e) aged by PAP-2

Table 5.1.3. Obtained *Si/Al* atomic ratio determined by XPS for S-CHA$_C$-SiAl2-Na series aged by PAP-2

Sample	*Si/Al* atomic ratio
S-CHAc-SiAl2-Na-V	2.2
S-CHAc-SiAl2-Na-E20d	2.6
S-CHAc-SiAl2-Na-E30d	3.0
S-CHAc-SiAl2-Na-E45d	3.0
S-CHAc-SiAl2-Na-E60d	3.1

From the CHN elemental analyses in the pristine (V) and the aged samples for 30 days (E30d) and for the longest time (E60d), it is possible to note a significant increase in the bulk carbon content of the solid (**Table 5.1.1.4**). According to (Karge, 1991)), the carbon content in zeolites is related to coke formation. Results of the carbon content of samples aged for a shorter period (S-CHAc-SiAl2-Na-E30d) confirm the hypothesis that carbon builds up in the solid, possibly due to coke formation triggered by high temperatures.

Table 5.1.4. Elemental CHN analysis for the pristine (V) and aged samples by PAP-2 in a single sample-port for 30 days (E30d) and 60 days (E60d)

Sample	C [%]	H [%]	N [%]
S-CHAc-SiAl2-Na-V	< 0.3	1.8	< 0.3
S-CHAc-SiAl2-Na-E30d	0.9	1.9	< 0.3
S-CHAc-SiAl2-Na-E60d	3.1	1.9	0.8

The N_2 isotherms at 77 K for the pristine CHA sample shows a characteristic behavior of microporous solids, or type I isotherms, up to 0.8 relative pressure, according to the IUPAC classification (Thommes et al., 2015) (**Figure 5.1.4**). In this pressure range, the measured adsorbed concentrations are in agreement with literature data for CHA zeolites (Ridha et al., 2009). Beyond $p/p_0 = 0.8$, the N_2 uptake rises steeply, which may be due to condensation in interstitial voids between particles. The N_2 adsorption isotherms for any of the aged samples, regardless the duration of the protocol, show a drastic decrease in uptake as compared to the pristine sample, comparable to isotherms of non-porous solids. The effect of aging is dramatic, particularly for relative pressure below 0.1. When the aged solids are compared to each other above relative pressure 0.1, the adsorption capacity decreases for increasing number of aging days (**Figure 5.1.4**). This acute reduction in N_2 adsorption is probably caused by the carbon deposition detected by CHN elemental analysis (**Table 5.1.4**). The carbon deposition may occupy/block pores, which is corroborated by the equally pronounced drop in total pore volume, as shown in **Table 5.1.5**. For the aged samples, the values of specific apparent BET area and total pore volume obtained from N_2 isotherms at 77 K are similar to each other, irrespective the number of days of the aging protocol (PAP) (**Table 5.1.5**). For this reason, isotherms using another probe gas or temperature may provide further information on the impact of increasing aging severity on textural properties.

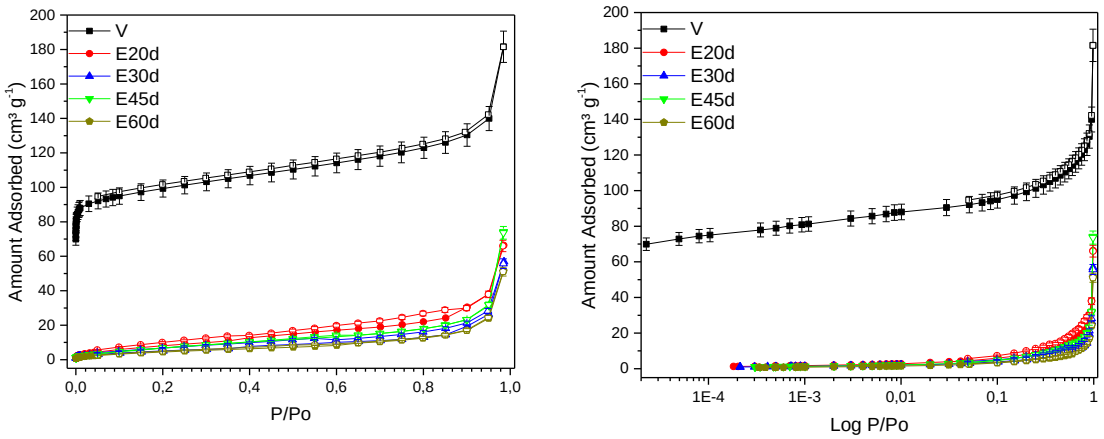

Figure 5.1.4. N_2 isotherms at 77 K for S-CHA$_C$-SiAl2-Na series aged by PAP-2 in linear (a) and logarithmic (b) scales

Table 5.1.5. Apparent BET area and pore volume from N_2 isotherms at 77 K for S-CHA$_C$-SiAl2-Na series aged by PAP-2

Sample	Apparent BET Area [$m^2\ g^{-1}$]	Total Pore Volume [$cm^3\ g^{-1}$]
V	308	0.281
E20d	34	0.031
E30d	20	0.018
E45d	31	0.022
E60d	19	0.014

Reference: (Stephen Brunauer, P. H. Emmett, 1938)

The CO_2 isotherms at 273 K for the pristine and aged samples are illustrated in **Figure 5.1.5**. CO_2 was considered as probe molecule because at 273 K, it may diffuse more easily in small micropores as compared to N_2 at 77K. Unlike N_2 isotherms, there is now a clear correlation between CO_2 uptake and the severity of aging (**Figure 5.1.5**). By checking isotherms in log scale (**Figure 5.1.5(b)**), the progressive decrease in uptake suggests that aging leads to pore obstruction, to an extent that only CO_2 may diffuse through. The pristine sample (-V) has a maximum adsorption capacity of 110.7 $cm^3\ g^{-1}$, while the most severely aged sample (-E60d) has less than 30% of such capacity. Similar to the trend observed in crystallinity (**Table 5.1.1**), the speed of aging seems to

slow down after 45 days, when prolonging the aging period no longer has a massive impact on the adsorption capacity. Micropore volume of the samples was estimated by the Dubinin-Radushkevich method using CO_2 isotherms at 273 K (Dubinin, M.M., Radushkevich, 1947) and the values are condensed in **Table 5.1.6**. By comparing the total pore volume, as estimated from N_2 isotherms (**Table 5.1.5**), and the micropore volume estimated from CO_2 isotherms (**Table 5.1.6**), the same trends are confirmed, even though N_2 at 77K does not have access to the full range of pores, especially ultramicropores brought about by carbon deposition upon aging.

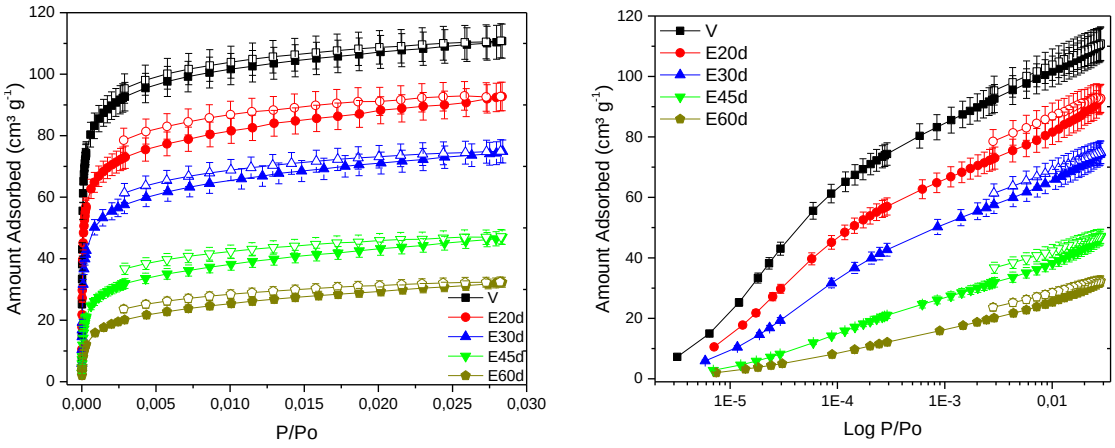

(a) **(b)**

Figure 5.1.5. CO_2 isotherms at 273 K for S-CHA$_C$-SiAl2-Na series aged by PAP-2 in linear (a) and logarithmic (b) scales

Table 5.1.6. Adsorption capacity and micropore volume from CO_2 isotherms at 273 K for S-CHA$_C$-SiAl2-Na series aged by PAP-2

Sample	Maximum Adsorption Capacity* [cm³ g^{-1}]	Micropore Volume [cm³ g^{-1}]
V	110.7 (100%)	0.225
E20d	92.7 (83.7%)	0.182
E30d	74.9 (67.7%)	0.156
E45d	47.0 (42.4%)	0.095
E60d	32.3 (29.2%)	0.072

* At a relative pressure of 0.029

Reference: (Dubinin, M.M., Radushkevich, 1947)

In **Figure 5.1.6**, the water adsorption isotherms are illustrated for the pristine sample (-V) and those aged for 30 and 45 days (-E30d and -E45d). The experimental data was fit by the Aranovich-Donohue Model – ADM (Aranovich & Donohue, 1995), which takes into account micropore filling according to the Sips model (Myers & Prausnitz, 1965) multiplied by a term that accounts for clustering or condensation in larger voids/defects in the zeolite structure (Equation 2.04). The shape of isotherms comprises a sharp increase in the low-pressure range, which confirms the high adsorbent-adsorbate affinity. The interactions of water molecules and the zeolite structure come from the zeolite affinity for polar molecules that is induced by the unbalanced charges brought about by AlO_4^- (Company, 2015; Kawai & Tsutsumi, 1992). The pristine material presents a maximum capacity of 256.08 mg g^{-1} at 50 mbar, while the aged materials have 233.44 mg g^{-1} for the sample (-E30d) and 165.47 mg g^{-1} for the sample (-E45d) also at 50 mbar. This decrease in water uptake (**Figure 5.1.6**) between the fresh and aged samples is associated with the reducing porosity in aged samples, presented by the N_2 at 77 K (**Figure 5.1.4**) and CO_2 at 273 K (**Figure 5.1.5**) isotherms, probably caused by the *C* deposition. Nevertheless, the deterioration in water uptake for aged samples was comparatively less severe than that observed in textural properties, which means that the zeolite retains most of its hydrophilic character, despite the impact of hydrothermal aging in other properties. When analyzing the high-pressure zone (pressures close to the saturation of water at 313 K), the difference between the adsorption capacity samples becomes higher. The pristine sample presents a steeper rise in uptake above 50 mbar as compared to the aged materials, that could be associated to a higher density of larger pores (interstitial voids or defects).

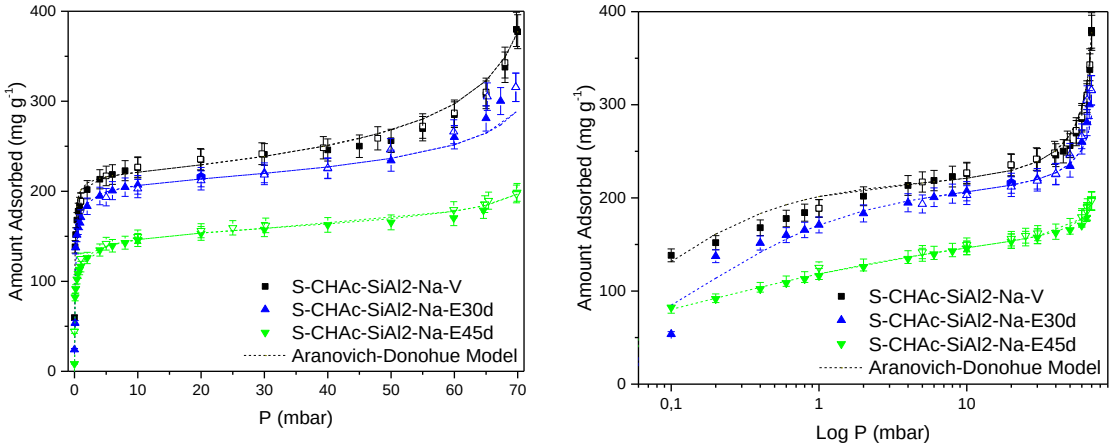

(a) **(b)**

Figure 5.1.6. H_2O isotherms at 313 K for S-CHAc-SiAl2-Na-(V, E30d, E45d) in linear (a) and logarithmic (b) scales

The isotherm fitting parameters of the ADM are condensed in **Table 5.1.7**. The parameter that qualifies the water-zeolite interaction (*b*) decreases almost an order of magnitude as compared to the pristine sample. This reduced adsorbent/adsorbate affinity may be associated with the carbon deposition (**Table 5.1.4**), thus reducing the availability of acid sites in the zeolite structure that bind water more strongly. In addition, the homogeneity of the solid surface (*n*) decreases with the deactivation, suggesting modifications in the energy topology of the zeolite with aging.

Table 5.1.7. Parameters Used in Aranovich-Donohue Model Fitting for H_2O Isotherms at 313 K for S-CHAc-SiAl2-Na-(V, E30d, E45d)

Sample	Parameters			
	q_{max} [mg g^{-1}]	b [$mbar^{-1}$]	n	e
S-CHAc-SiAl2-Na-V	217.41	16.07	0.90	0.19
S-CHAc-SiAl2-Na-E30d	210.69	6.10	0.80	0.11
S-CHAc-SiAl2-Na-E45d	168.30	7.97	0.41	0.08

5.1.2 PAP-1 AND PAP-2 FOR CHA SAMPLES

In order to better visualize the aging effects in samples submitted to different aging protocols, a comparison was carried out for CHA in Na form with an intermediate Si/Al ratio (S-CHAc-SiAl2-Na). A sample was aged by PAP-1 for 35 cycles (E35c) and another one, by PAP-2 for 30 days using a single sample-port (E30d) and a third sample, by PAP-2 for 30 days but using a dual sample-port (E30d*). The diffractograms for the three aged samples present similar patterns, although reflection peaks have different magnitudes (**Figure 5.1.7**). The main reflection peaks are located in the 2θ range from 20° to 32° (20.4, 22.9, 24.7, 25.8 and 30.4°) (Cejka et al., 1985). All identified peaks agree with the standard of the pristine sample. The samples crystallinity, calculated from the sum of areas under the main peaks from 20° to 32° divided by that for the pristine sample, are shown in **Table 5.1.8**. Regardless using a single or dual sample-port, the aged samples in PAP-2 suffer a similar reduction in crystallinity, around 67%. On the contrary, the structure of the sample submitted to PAP-1 was practically unchanged (**Table 5.1.7**). The crystallinity changes in the aged CHA by PAP-2 is possibly associated to the maintenance of high temperatures for longer times.

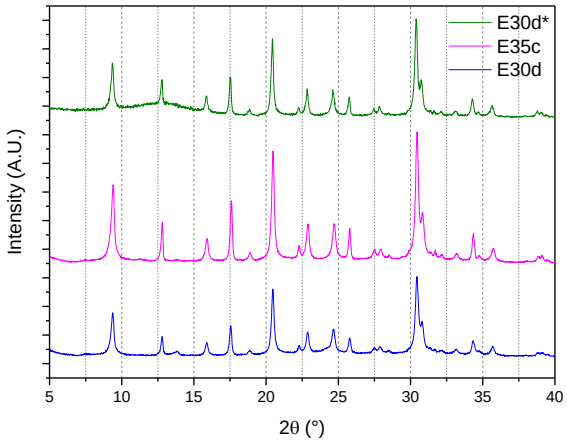

Figure 5.1.7. XRD patterns for S-CHAc-SiAl2-Na aged under different protocols (E30d, E30d*, E35c)

Table 5.1.8. Materials Crystallinity determined by XRD Diffractograms to the S-CHAc-SiAl2-Na Aged by PAP-1 (-E35c) and by PAP-2 in a Single (-E30d) and Dual (-E30d*) Sample-Port

Sample	Crystallinity [%]
S-CHAc-SiAl2-Na-V	100
S-CHAc-SiAl2-Na-E30d	65.56
S-CHAc-SiAl2-Na-E30d*	68.49
S-CHAc-SiAl2-Na-E35c	97.85

The surface atomic concentrations, as determined by XPS, for the pristine sample (S-CHAc-SiAl2-Na-V), aged by PAP-1 (S-CHAc-SiAl2-Na-E35c) and those aged by PAP-2 (S-CHAc-SiAl2-Na-E30d and S-CHAc-SiAl2-Na-E30d*) are shown in **Table 5.1.9**. In general, the content of carbon on the surface does not follow a clear trend, whereas the *Si/Al* ratios increase for aged materials (**Table 5.1.10**). It is likely that carbon deposition preferentially occurs in the stronger acid sites (*Al – O*), thus covering Al atoms on the surface and leading to an apparent increase in Si/Al ratio. The binding energies (BE) of the aged materials (not shown) have similar assignments as those previously presented in **Table 5.1.2**. In short, C *1s* accounts for C – C and C – O bonds. The BE for *Si*2p, *Al2p* and O *1s* are those typically found in aluminosilicates for tetrahedral coordination (C.D. Wagner, W.M. Riggs, L.E. Davis, J.F. Moulder, 1979).

Table 5.1.9. Chemical Surface determined by XPS Analysis (% mass concentration) for the S-CHA$_C$-SiAl2-Na- (V, E30d, E30d*, E35c) Aged by PAP-1 and PAP-2

Sample	C1s	O1s	Al2p	Si2p	Na1s	K2p
S-CHAc-SiAl2-Na-V	17.76	59.05	5.53	11.88	5.18	0.59
S-CHAc-SiAl2-Na-E30d	15.59	61.52	4.17	11.87	6.25	0.59
S-CHAc-SiAl2-Na-E30d*	23.48	54.97	4.08	10.18	6.77	0.51
S-CHAc-SiAl2-Na-E35c	23.27	55.30	3.94	10.01	7.01	0.46

Table 5.1.10. Atomic *Si/Al* ratios, as determined by XPS Analysis for the S-CHA$_C$-SiAl2-Na- (V, E30d, E30d*, E35c) Aged by PAP-1 and PAP-2

Sample	*Si/Al* atomic ratio
S-CHAc-SiAl2-Na-V	2.2
S-CHAc-SiAl2-Na-E30d	3.0
S-CHAc-SiAl2-Na-E30d*	2.6
S-CHAc-SiAl2-Na-E35c	2.6

From the CHN elemental analysis (**Table 5.1.11**), there is an increasing content of carbon in the bulk for the aged samples as compared to the fresh sample (V). The detected *C* content in the sample aged by PAP-1 varies in a relatively wide range; this heterogeneity is probably caused by the manual addition (pouring) of the hydrocarbon (*n*-heptane) in liquid form. In both samples aged by PAP-2, a smaller increase in the carbon content was measured, which may be correlated to a partial deterioration of textural properties and water uptake (Bukhtiyarova & Echevskii, 2020) to be described in the following sections. The carbon content results as given by CHN elemental analysis suggests that there is carbon deposition in the inner and outer structure of the samples.

Table 5.1.11. Elemental CHN Analysis for the Pristine (V), Aged Samples by PAP-1 (E35c) and by PAP-2 in a Single (E30d) and Dual (E30d*) Sample-Port

Sample	C [%]	H [%]	N [%]
S-CHAc-SiAl2-Na-V	< 0.3	1.8	< 0.3
S-CHAc-SiAl2-Na-E35c	1.2 - 4.9	1.6 - 4.6	0.4 - 4.7
S-CHAc-SiAl2-Na-E30d	0.9	1.9	< 0.3
S-CHAc-SiAl2-Na-E30d*	0.5	1.6	0.3

NMR analyses (**Table 5.1.12**) reveal a similar *Si/Al* ratio after any aging procedure, *either* PAP1 or PAP2. The sample aged by PAP1, S-CHAc-SiAl2-Na-E35c, and the sample aged by PAP2, S-CHAc-SiAl2-Na-E30d*, maintain approximately the ratio between these elements. Considering the results from XPS analyses, where the *Si/Al* ratio increased in the material external surface (**Table 5.1.10**), it is likely that a migration of *Al* to the inner of the material occurs upon aging. In this way, the *Si/Al* ratio may increase in the external surface though nearly constant in the bulk material.

Table 5.1.12. Si/Al Ratio by NMR Analyses for the Pristine (V), Aged Samples by PAP-1 (E35c) and by PAP-2 in a and Dual Sample-Port (E30d*)

Sample	Si/Al ratio
S-CHAc-SiAl2-Na-V	2.1
S-CHAc-SiAl2-Na-E35c	2.1
S-CHAc-SiAl2-Na-E30d*	1.9

The N_2 isotherms at 77 K (**Figure 5.1.8**) indicate microporous materials with a good adsorbent-adsorbate interaction (Thommes et al., 2015). In addition, a decrease in uptake of N_2 in different extents is observed for aged materials. The sample aged by PAP-2 using the dual port was much less affected. This distinct behavior is probably due to an incomplete evaporation of the water and n-heptane in the cylinder (see **Figure 4.02**) because twice as much amount is required in the dual-port mode (two samples aged simultaneously) as compared to the protocol with one port. The dual sample-port in the PAP-2 results in a less degraded material with textural properties closer to the pristine sample (**Figure 5.1.8**). As a matter of fact, Santiago (Gomes Santiago et al., 2019) state that the degradation of textural properties is closely related to the presence of the hydrocarbon. PAP-2 appears as an improvement from the PAP-1, not only because it requires a smaller sample mass, but also for allowing the homogeneous vapor-phase pre-adsorption of water and n-heptane. However, using a dual port may impact on the severity of aging, as explained above. By comparing the specific apparent BET area and total pore volume obtained from N_2 isotherms at 77 K (**Table 5.1.13**), the aging by PAP-1 (-E35c) or single port PAP-2 (-E30d) caused a similar degradation.

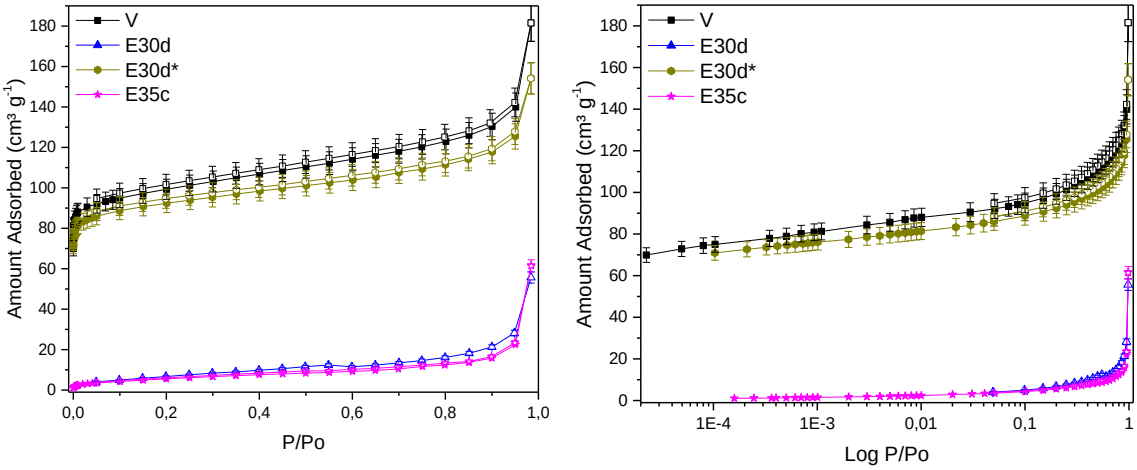

(a) **(b)**

Figure 5.1.8. N_2 isotherms at 77 K in linear (a) and logarithmic (b) scales for (S-CHA$_C$-SiAl2-Na): pristine (V); aged by PAP-1 (E35c) and by PAP-2 in a single (E30d) and dual (E30d*) sample port

Table 5.1.13. Apparent BET area, pore volume, adsorption capacity and micropore volume for S-CHA$_C$-SiAl2-Na-(V, E30d, E30d*, E35c)

Sample	from N_2 Isotherms at 77 K		from CO_2 Isotherms at 273 K	
	Apparent BET Area [m^2 g^{-1}]	Total Pore Volume [cm^3 g^{-1}]	Maximum Adsorption Capacity * [cm^3 g^{-1}]	Micropore Volume [cm^3 g^{-1}]
V	308	0.281	110.7	0.225
E30d	20	0.018	74.9	0.156
E30d*	267	0.164	85.0	0.174
E35c	22	0.016	63.6	0.138

* At a relative pressure of 0.029

References: (Brunauer et al., 1938; Dubinin, M.M., Radushkevich, 1947)

Regarding the CO_2 adsorption at 273 K, the isotherms presented a type I shape (**Figure 5.1.9**), according to the IUPAC classification (Thommes et al., 2015). Comparing the porous structures obtained from N_2 and CO_2 isotherms at 77K and 273K (**Table 5.1.13**), respectively, it is clear that the different kinetic diameter of the

molecules and the higher temperature used in the CO_2 experiments allows for the latter molecule to better access the porosity and reveals an important micropore volume. The pristine sample has a micropore volume of 0.225 $cm^3\ g^{-1}$, which is reduced in the sample aged by PAP-1 (42% decrease) whereas the sample aged by PAP-2 is significantly less affected, with smaller reductions in microporosity. In addition, **Figure 5.1.9 (b)** allows for a better visualization in the low-pressure range to better analyze the impact of the aging procedures on the stronger adsorption sites.

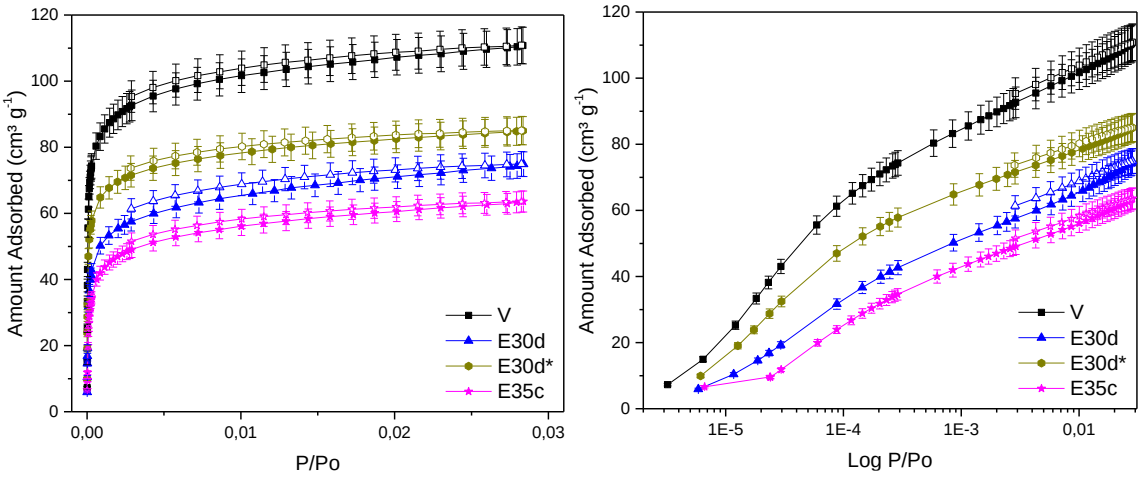

Figure 5.1.9. CO_2 isotherms at 273 K in linear (a) and logarithmic (b) scales for (S-CHA$_C$-SiAl2-Na): pristine (V); aged by PAP-1 (E35c) and by PAP-2 in a single (E30d) and dual (-E30d*) sample port

The water vapor isotherms at 313 K (**Figure 5.1.10**) also show that the adsorbed concentrations of the aged materials are below those measured for the pristine sample, although the differences in uptake are significantly more modest than those observed for N_2 and CO_2 adsorption (**Figure 5.1.8** and **5.1.9**). All isotherms have a step rise in the low-pressure range, up to 5 mbar, indicating the existence of strong adsorbate-adsorbent interaction, which persists despite the aging protocols. In the pressure range from 5 to 40 mbar, all isotherms reach a plateau visible in the linear scale, which is lower for aged samples and nearly the same for those aged by PAP-2 (regardless the type of sample port). Beyond 40 mbar, there is a sudden rise in the high-pressure zone. The sample aged in the PAP-1 (-E35c) does have the lowest

microporosity among the aged samples (**Table 5.1.13**) and it also shows the highest *C* content (**Table 5.1.11**). The carbon seems to block some of the assessing pores of the zeolite to the inner structure, which is evidenced by the very low uptake in the N_2 adsorption isotherms (**Figure 5.1.8**). Nevertheless, it seems that some strong sites located in micropores are preserved, which is shown in CO_2 isotherms (**Figure 5.1.9**) and further confirmed in water isotherms in the low-pressure range (**Figure 5.1.10(b)**). For samples aged by the PAP-2, it seems that carbon is deposited in the stronger micropore sites, thus reducing CO_2 and H_2O uptake in the low-pressure range, despite a modest *C* content as compared to the sample aged by PAP-1. In fact, the marked differences in the two aging protocols are that, prior to heating, PAP-2 exposes the sample to a homogeneous environment containing water and n-heptane vapors whereas in PAP-1, liquid hydrocarbon is poured onto the sample; Second, the continuous exposure to high-temperature occurred in PAP-2 may affect the structure and chemical bonds. PAP-2 also causes partial degradation in the samples, as PAP-1, leading to changes in sample adsorption properties. However, to obtain a similar degradation degree in both PAPs, PAP-2 should be performed for a more prolonged time. The Aranovich-Donohue model (ADM) fitted all isotherms satisfactorily in the complete pressure range (**Figure 5.1.10**). The ADM parameters (**Table 5.1.14**) have consistent values with the previous discussions. Regarding the parameter accounting for the adsorbate-adsorbent interaction (*b*), the significant decreases obtained in the aged samples corroborate the inactivation of some of the strong adsorption sites. The heterogeneity parameter (*n*) of the sample aged by the PAP-1 (-E35c) presents an interesting decrease in comparison to the pristine and aged materials by the PAP-2, which may be a consequence of the uneven distribution of the hydrocarbon in the former protocol.

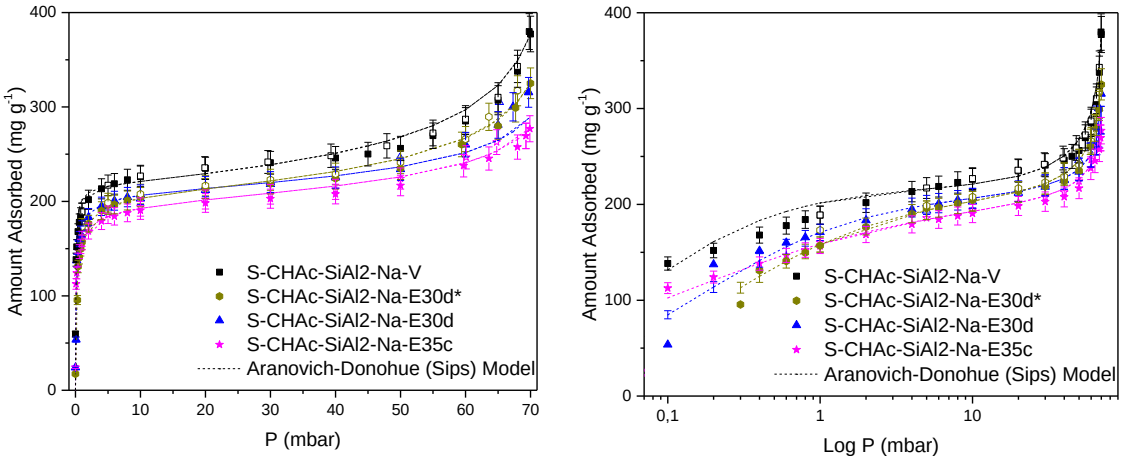

Figure 5.1.10. H_2O isotherms at 313 K in linear (a) and logarithmic (b) scales for (S-CHA$_C$-SiAl2-Na): pristine (V); aged by PAP-1 (E35c) and by PAP-2 in a single (E30d) and dual (E30d*) sample port. The dashed curves stand for the Aranovich-Donohue model fits

Table 5.1.14. Parameters Used in Aranovich-Donohue Model Fitting for H_2O Isotherms at 313 K for S-CHAc-SiAl2-Na-(V, E30d, E30d*, E35c)

Sample	Parameters			
	q_{max} [mg g^{-1}]	b [$mbar^{-1}$]	n	e
S-CHAc-SiAl2-Na-V	217.41	16.07	0.90	0.19
S-CHAc-SiAl2-Na-E30d*	208.96	4.09	0.80	0.15
S-CHAc-SiAl2-Na-E30d	210.69	6.10	0.80	0.11
S-CHAc-SiAl2-Na-E35c	207.29	9.54	0.52	0.11

SECTION 5.1 - PARTIAL CONCLUSIONS

The newly proposed aging protocol (PAP-2) caused a mild degradation of the crystalline structure of the samples with a much smaller sample size than PAP-1. The longer the aging time is, the higher degradation degree is observed in the several studied properties. It may be postulated that the hydrocarbon present in the aging protocol (n-heptane) is evenly adsorbed in the inner and outer pores of the zeolite, because it is charged to the sample in vapor phase, unlike PAP-1. All aged materials showed worsened textural characteristics, which seemed directly correlated to the increase in *C* content in the bulk. Regarding the aging period, the interval 20-30 days causes the most pronounced modifications in the porosity and crystallinity although not as drastic as in PAP-1. Hence, 30 days was taken as the aging period used in the next **Sections 5.2**, **5.3** and **5.4**. Comparing the results from PAP-1 and PAP-2 in a single and dual sample-port, they present different degradation degrees. The maintenance of high temperatures imposed by the PAP-2 causes a higher loss of crystallinity. Furthermore, the aged samples undergoing the PAP-2 had a more homogeneous composition (particularly CHN analysis) either in a single or dual sample-port. Having said that, PAP-2 (30 days) using a dual sample-port was the aging method of choice to assess the impact of Si/Al ratio and nature of compensation cation on the hydrothermal stability of cationic zeolites.

5.2 CHABAZITE – CHA

The X-ray diffractograms of the pristine and aged samples are shown in **Figure 5.2.1**. The overall intensities of the diffraction peaks of the aged samples are lower, but the peak positions do not significantly change. Also, the absence of the typical broad band at 20 - 30 degrees characteristic of the presence of amorphous solid indicates that CHA samples do not undergo drastic modifications upon aging. For all samples, irrespective the Si/Al ratio, the nature of the cation or the extent of aging (V or E30d*), the main characteristic diffraction peaks of a CHA structure are present and located in similar positions to those previously reported for CHA materials of similar *Al* contents (Cejka et al., 1985; Mintova & Barrier, 2016).

Table 5.2.1 summarizes the crystallinity of the aged samples, defined as the sum of areas under the main peaks in the range from 20 to 32° divided by the same sum for the pristine sample. As expected, a higher *Si/Al* ratio (5) for the Na samples leads to superior crystallinity, despite undergoing the aging protocol. The crystallinity of CHA sample with *Si/Al* ~ 2 (S-CHAc-SiAl2-Na-E30d*) decreases by 32% upon aging, whereas the sample with a higher Si/Al retains nearly the same crystallinity. The robustness of the latter sample is due to a superior thermal stability of *Si–O* bonds as compared to *Al–O* bonds, which means that more energy is required to break the former (Cruciani, 2006; Kerr, 1967). On the other hand, for the CHA samples with the same *Si/Al* ratio and different compensating cations, the presence of *K* renders the crystal lattice a higher resistance to aging. The presence of K^+ as compensating cations acts as a transformation inhibitor in the materials, increasing its resistance to elevated temperatures (Cartlidge et al., 1984).

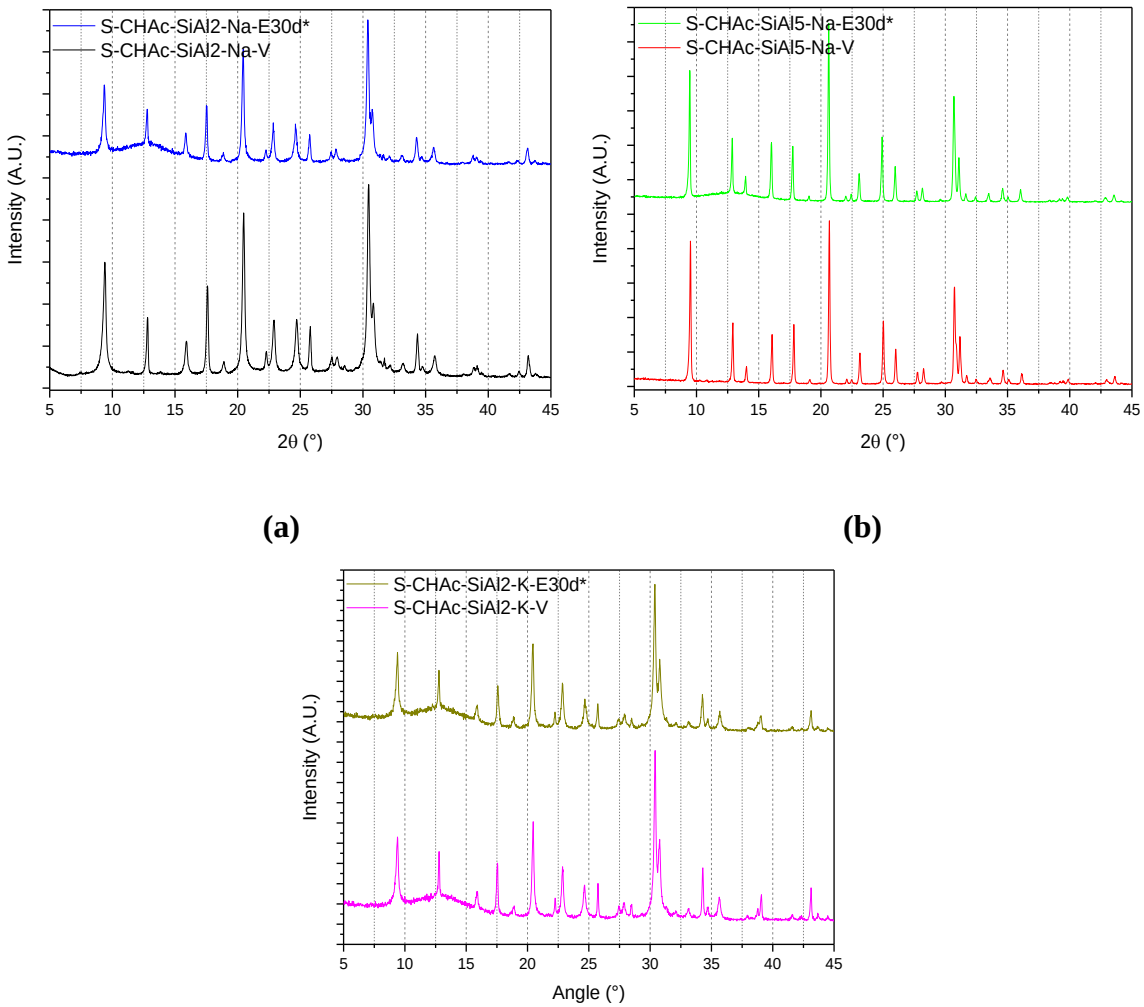

Figure 5.2.1. XRD diffractograms for S-CHA$_C$-SiAl2-Na- (V, E30d*) (a), S-CHA$_C$-SiAl5-Na- (V, E30d*) (b) and S-CHA$_C$-SiAl2-K- (V, E30d*) (c)

Table 5.2.1. Materials Crystallinity from XRD Diffractograms to the Samples S-CHAc - SiAl(2, 5) - (Na, K) - (V, E30d*)

Sample	Crystallinity [%]
S-CHAc-SiAl2-Na-V	100
S-CHAc-SiAl2-Na-E30d*	68
S-CHAc-SiAl5-Na-V	100
S-CHAc-SiAl5-Na-E30d*	96
S-CHAc-SiAl2-K-V	100
S-CHAc-SiAl2-K-E30d*	90

The chemical surface composition, as determined by XPS for all samples under study, is shown in **Table 5.2.2**. The carbon content present on the surface of the pristine samples it is mostly attributed to adventitious carbon due to sample manipulation (Evans, 1997). Except for the sample S-CHAc-SiAl2-K-V, all the other samples (*Na* form) display an increase in carbon content on the surface after undergoing the aging protocol, which may be related to coke formation (Guisnet et al., 1997). This is likely to be related to the lower *Si/Al* and hence, increase in framework negative charge which may trigger more intense coke deposition and impact on the lower crystallinity, as observed in **Table 5.2.1**. For the same *Si/Al* ratio, the sample S-CHAc-SiAl2-K-V shows a lower carbon content on the surface after undergoing the aging protocol, which is an unexpected result. Because XPS is a spectroscopic technique that only examines the external surface, another technique to assess the chemical composition in the bulk may be useful to better understand this behavior. **Table 5.2.3** summarizes the binding energies found in the detailed spectral regions (not shown) of each of the identified elements in the samples. The Binding Energy (BE) for carbon (C 1*s*) accounts not only for bonds C – C (~284.6 eV), but also a small contribution from C – O (~286.3 eV); the binding energies for Si 2*p* (~102.5 eV) and Al 2*p* (~74.1 eV) are typical of the tetrahedral coordination in aluminosilicates and the binding energy for O 1*s* (~532.0 eV) also refers to aluminosilicates (Bare et al., 2016; C.D. Wagner, W.M. Riggs, L.E. Davis, J.F. Moulder, 1979). Note that *Al* is only present with a single binding energy and no octahedral coordination (extra-framework *Al*) was detected on the surface of either the pristine or aged samples. The theoretical *Si/Al* ratios of the samples approximately match those found by XPS in the case of *Si/Al*=2 (**Table 5.2.4**). For the sample S-CHAc-SiAl5-Na-V, the *Si/Al* ratio on the surface is considerably higher than the theoretical value expected from the synthesis-gel composition (≈5), which suggests that *Al* atoms tend to be located in the bulk of the solid, rather than on the surface. Interestingly, the aging protocol led to an increase in the *Si/Al* ratio on the surface of all samples – a more pronounced behavior being observed for the samples with lower *Si/Al* in the pristine samples (**Table 5.2.4**). It may be postulated that, when the samples are aged, carbon deposits preferentially at the vicinity of *Al*-centered tetrahedra, due to its higher acidity as compared to *Si*-centered tetrahedra, thus covering the surface and causing a decrease in the *Al* atomic concentration (see **Table 5.2.2**) (Moura et al., 2021). In addition, the migration of *Al* to the inner of the material occurs upon aging (Moura et al., 2021).

Table 5.2.2. Chemical Surface Composition (%mass concentration) Determined by XPS Analyses for the Samples S-CHA$_C$-SiAl (2, 5)- (Na, K) - (V, E30d*)

Sample	C1s	O1s	Al2p	Si2p	Na1s	K2p
S-CHAc-SiAl2-Na-V	17.8	59.0	5.5	11.9	5.2	0.6
S-CHAc-SiAl2-Na-E30d*	23.5	55.0	4.1	10.2	6.8	0.5
S-CHAc-SiAl5-Na-V	18.6	62.5	1.9	14.2	2.8	-
S-CHAc-SiAl5-Na-E30d*	22.1	59.8	1.7	14.0	2.5	-
S-CHAc-SiAl2-K-V	15.2	64.4	4.8	11.4	-	4.2
S-CHAc-SiAl2-K-E30d*	12.1	66.6	4.6	12.6	-	4.1

Table 5.2.3. Binding Energy values (eV) end Contributions for the Samples S-CHA$_C$-SiAl (2, 5)- (Na, K) - (V, E30d*)

Sample	Si2p	Al2p	C1s	O1s	Na1s	K2p3/2
S-CHAc-SiAl2-Na-V	102.6	74.6	285.0 286.6	531.8	1072.7	294.6
S-CHAc-SiAl2-Na-E30d*	102.5	74.1	284.7 285.9	531.6	1072.3	294.5
S-CHAc-SiAl5-Na-V	103.1	74.3	284.8 286.3	532.5	1072.8	-
S-CHAc-SiAl5-Na-E30d*	103.3	74.5	284.8 286.3	532.6	1073.0	-
S-CHAc-SiAl2-K-V	102.4	74.2	284.9 286.3	531.5	-	294.3
S-CHAc-SiAl2-K-E30d*	102.5	74.1	284.7 286.0	531.6	-	294.3

Table 5.2.4. Obtained *Si/Al* Atomic ratios Determined by XPS Analyses for the Samples S-CHA$_C$-SiAl (2, 5)- (Na, K) - (V, E30d*)

Sample	*Si/Al* atomic ratio
S-CHAc-SiAl2-Na-V	2.24
S-CHAc-SiAl2-Na-E30d*	2.60 (+13.8%)
S-CHAc-SiAl5-Na-V	7.93
S-CHAc-SiAl5-Na-E30d*	8.52 (+6.9%)
S-CHAc-SiAl2-K-V	2.40
S-CHAc-SiAl2-K-E30d*	2.85 (+12.2%)

The chemical composition of the samples, as obtained from ICP-OES (**Table 5.2.5**), allows quantifying the elements in the solid bulk. Acceptable deviations from the theoretical *Si/Al* ratio are observed (less than 5% for the samples with lower *Si/Al*). By comparing the *Si/Al* ratios found by XPS (**Table 5.2.4**) and ICP-OES (**Table 5.2.5**) for sample S-CHAc-SiAl5-Na-V, it becomes evident that *Al* atoms tend to migrate to the bulk of the solid. The content of elements *Na* and *K*, the compensating cations, is consistent with the composition of the respective synthesis gels mentioned in **Section 4.1**. From the column (*Na* + *K*)/*Al* in the **Table 5.2.5**, it is possible to conclude that all the negative charge generated in the structure by the *Al* atoms is compensated by the sum of *Na* and *K* cations in the samples with *Si/Al* = 2, in which case the presence of Bronsted acid sites is ruled off. In the case of the sample S-CHAc-SiAl5-Na-V, there are more *Al* atoms than compensating cations available, which is likely to produce a negative charge that must be neutralized by protons, possibly giving rise to Bronsted Acid Sites – BAS. On the other hand, this additional content of *Al* may be present as extra-framework *Al* (EFAl) or defective sites (Lewis's acidity). ^{27}Al NMR spectra for the samples S-CHAc-SiAl5-Na- (V, E30d*) (**Figure 5.2.2**) reveal *Al* content outside the cationic zeolite structure, represented by the peak at approximately 0 ppm in the **Figure 5.2.2**. From the pristine and aged materials, the EFAl's content remains approximately 4.1% in mass percentage (**Table 5.2.6**). The other pristine and aged zeolites with a *Si/Al* ratio ~ 2 only presented *Al* with tetrahedral coordination, i.e., located in the zeolite framework. The presence of EFAl is generally related to the zeolite acidity (C. Liu et al., 2015) and the key role of acidity in the coke formation has been addressed by (Guisnet et al., 1997), who state that the strength of the acid sites in zeolites impacts on

the coke deposition. It is also important to highlight that, in the case of the sample S-CHAc-SiAl5-Na-V, the mass percentages for each element of this material in the **Table 5.2.5** were obtained from the weighted average of 7 batches. The necessity of more than a single batch comes from the low reaction yield in the synthesis procedures (**Chapter 4.1**).

Table 5.2.5. ICP-OES for the Samples S-CHA$_C$-SiAl (2, 5)–(Na, K)– V [*% Weight*]

Sample	*Si*	*Al*	*Na*	*K*	*(Na + K) /Al*	*Si/Al* Ratio
S-CHAc-SiAl2-Na-V	49.2	24.8	16.9	9.0	1.0	1.9
S-CHAc-SiAl5-Na-V	74.8	16.5	10.2	0.1	0.7	4.4
S-CHAc-SiAl2-K-V	46.9	21.5	0.1	22.3	0.7	2.1

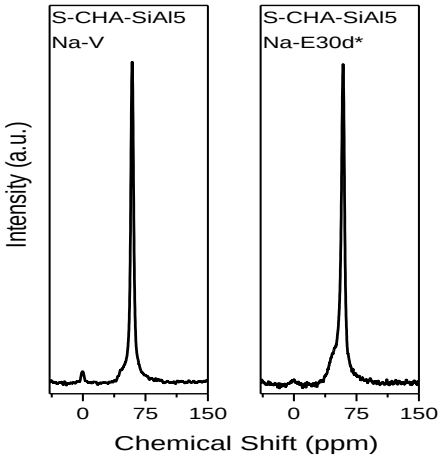

Figure 5.2.2. ^{27}Al NMR spectra for the sample S-CHAc-SiAl5-Na- (V, E30d*)

Table 5.2.6. The *EFAl's* content by ^{27}Al NMR spectra in the samples S-CHAc-SiAl5-Na- (V, E30d*)

Sample	*Al* content [% Mass]
S-CHAc-SiAl5-Na-V	4.4
S-CHAc-SiAl5-Na-E30d*	3.9

The *Si/Al* ratios were also estimated from NMR spectra (**Table 5.2.7**) for all CHA samples and values were consistent with those in the respective synthesis gels.

The variation of *Si/Al* ratio (2 and 5) and compensating cation (*Na* and K) in CHA samples do not seem to cause significant modification in the bulk *Si* and *Al* contents upon aging. Regarding the XPS results (**Table 5.2.4**), where the *Si/Al* ratio increases in all cases after aging, it is likely that *Al* migration is occurring from the external to the internal surface of the material (Moura et al., 2021).

Table 5.2.7. Si/Al Ratio by NMR Analyses for the S-CHAc-SiAl(2, 5) – (Na,K) - (V, E30d*) Samples

Sample	Si/Al ratio
S-CHAc-SiAl2-Na-V	2.1
S-CHAc-SiAl2-Na-E30d*	1.9
S-CHAc-SiAl5-Na-V	5.2
S-CHAc-SiAl5-Na-E30d*	5.1
S-CHAc-SiAl2-K-V	2.2
S-CHAc-SiAl2-K-E30d*	2.1

The results of the elemental analysis of the CHA samples are summarized in **Table 5.2.8** and, similarly to ICP-OES, they provide information on the carbon content in the bulk solid phase of the samples. For the samples with lower *Si/Al* ratio (S-CHAc-SiAl2-*Na* and S-CHAc-SiAl2-K), the increase in *C* content upon aging was negligible as compared to that measured for the sample with higher *Si/Al* ratio (S-CHAc-SiAl5-Na). The content of *C* in the latter sample augmented, which is counterintuitive because a higher density of *Si – O – Si* bonds is expected to provide a more neutral framework with less coke deposition. The presence of the EFAl (**Table 5.2.6**) probably had a huge impact in the material acidity. The key role of acidity in the coke formation has been addressed by (Guisnet et al., 1997), who state that the strength of the acid sites in zeolites impact on the coke development. The acid sites in the inner porosity of zeolites catalyze the reactions of adsorbed hydrocarbons and the formed coke tends to build up in the pores (Guisnet et al., 1997). On the other hand, the *C* content detected by *CNH* elemental analysis may not necessarily refer to coke, but physisorbed *n*-heptane if zeolite acidity is not strong enough to trigger coke formation.

Table 5.2.8. CHN analysis for the Samples S-CHAc-SiAl(2, 5)-(Na, K) - (V, E30d*)

Sample	*C content [%]* Measurement Uncertainty: ± 0.3
S-CHAc-SiAl2-Na-V	0.3
S-CHAc-SiAl2-Na-E30d*	0.5
S-CHAc-SiAl5-Na-V	0.3
S-CHAc-SiAl5-Na-E30d*	2.5
S-CHAc-SiAl2-K-V	0.3
S-CHAc-SiAl2-K-E30d*	0.3

It has been said that different synthesis batches were performed due to typically low yield, particularly for the higher *Si/Al* ratios. SEM images were obtained for the different batches of the same pristine zeolite materials to verify whether they had similar morphologies (**Figure 5.2.3**). The first and the second batches of the CHA sample with higher *Si/Al* ratio present similar crystal morphologies and tend to form clusters (**Figure 5.2.3(a)**). On the other hand, the characteristic orthorhombic shape is distorted at a lower Si/Al ratio (*Si/Al* = 2), possibly due to the increased concentration of *Al* atoms and thus framework charge (**Figure 5.2.3(b)** and **(c)**). In addition, the CHA sample having a higher content of sodium and potassium (S-CHAc-SiAl2-Na-V) - confirmed by ICP-OES analyses (**Table 5.2.5**) - presents also an undetermined structure (**Figure 5.2.3(b)**). The different bond lengths between *Si – O* and *Al – O* are likely to lead to a less well-defined structure, which has already been reported by (Lopez et al., 2003) and (Bressel et al., 2008). Broader peaks in the XRD diagrams of the two pristine materials (S-CHAc-SiAl2-Na-V) corroborate the fact that the *Al* amount may modify the zeolite morphology (**Figure 5.2.1**). Moreover, the different *K* content in the two CHA materials with Si/Al =2 may also lead to variations in the structure morphology.

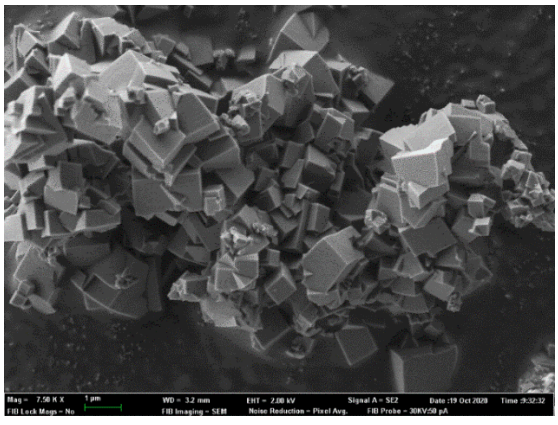

First Batch (mag. 7,500x)

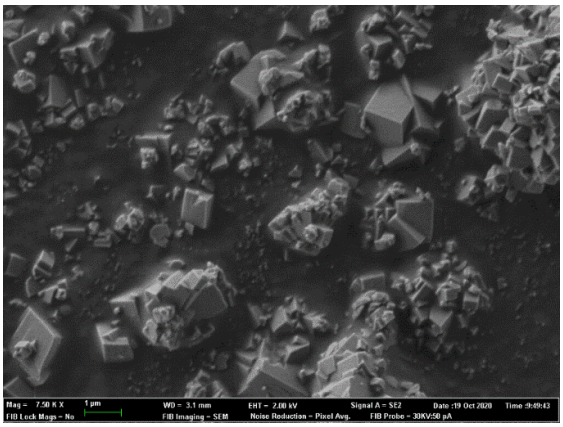

Second Batch (mag. 7,500x)

(a)

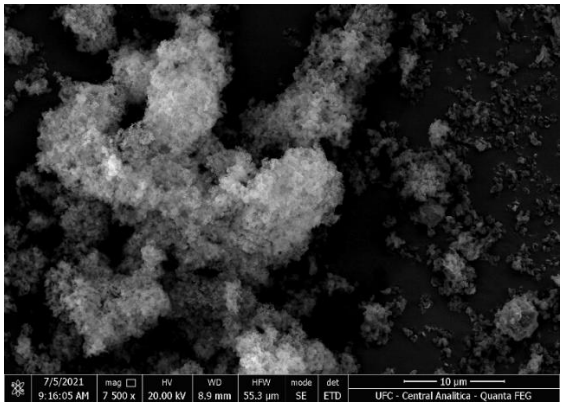

Single Batch (mag. 7,500x)

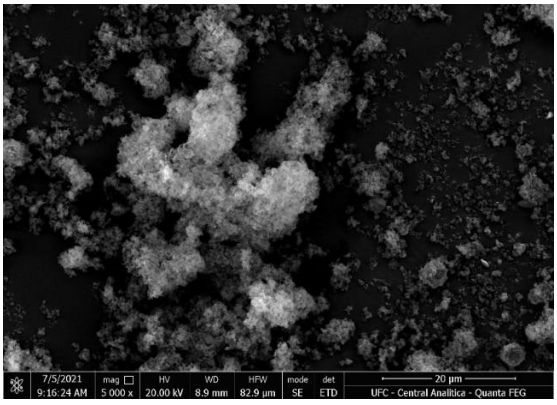

Single Batch (mag. 5,000x)

(b)

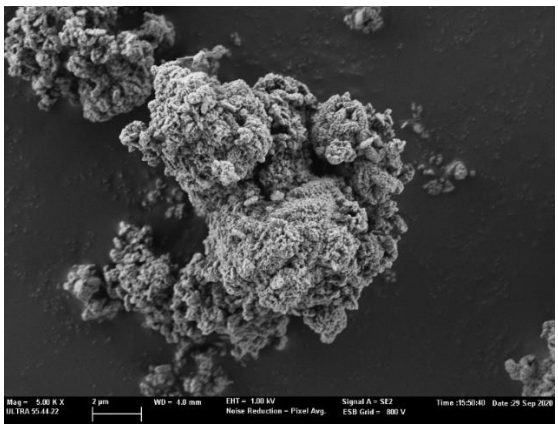

First Batch (mag. 5,000x)

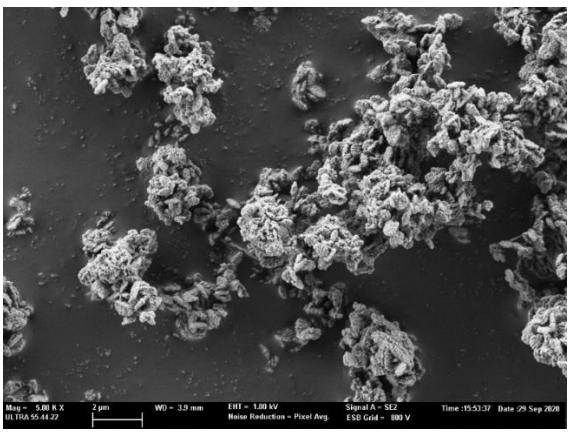

Second Batch (mag. 5,000x)

(c)

Figure 5.2.3. SEM analyses for S-CHAc-SiAl5-Na-V (a); S-CHAc-SiAl2-Na-V (b); S-CHAc-SiAl2-K-V (c)

From the NH_3 desorption profiles shown in **Figure 5.2.4**, it is clear that most ammonia is physically adsorbed because desorption majorly takes place at a relatively mild temperature (below 300 °C). This is especially true for the samples with *Si/Al* = 2, which is consistent with the balance observed between (*Na* + *K*) and *Al* (**Table 5.2.5**), thus ruling off the presence of Bronsted acid sites in these samples. In the sample with *Si/Al* = 2 containing *Na*, the deposition of carbon due to the aging protocol is therefore not due to Bronsted acid sites (BAS) in the fresh sample. Instead, BAS may be formed in the presence of water from Lewis sites in situ during the aging protocol, but this hypothesis requires further investigation. The sample showing the highest *C* deposition (S-CHAc-SiAl5-Na) (**Table 5.2.8**) was also the one with the highest amount of desorbed NH_3 at higher temperatures (above 300°C), suggesting the presence of Bronsted sites. This agrees well with the fact that there are more *Al* atoms than the sum of *Na* and *K* in this sample (**Table 5.2.5**). Interestingly, the aged sample (S-CHAc-SiAl5-Na-E30d*) is the one that undergoes the greatest reduction in desorbed NH_3 of all samples as compared to its fresh counterpart. This suggests that the carbon deposition brought about by aging may have partially deactivated the acid sites (those desorbing NH_3 above 300 ^oC) and considerably reduced the available pore volume for ammonia adsorption (desorbed below 300 ^oC).

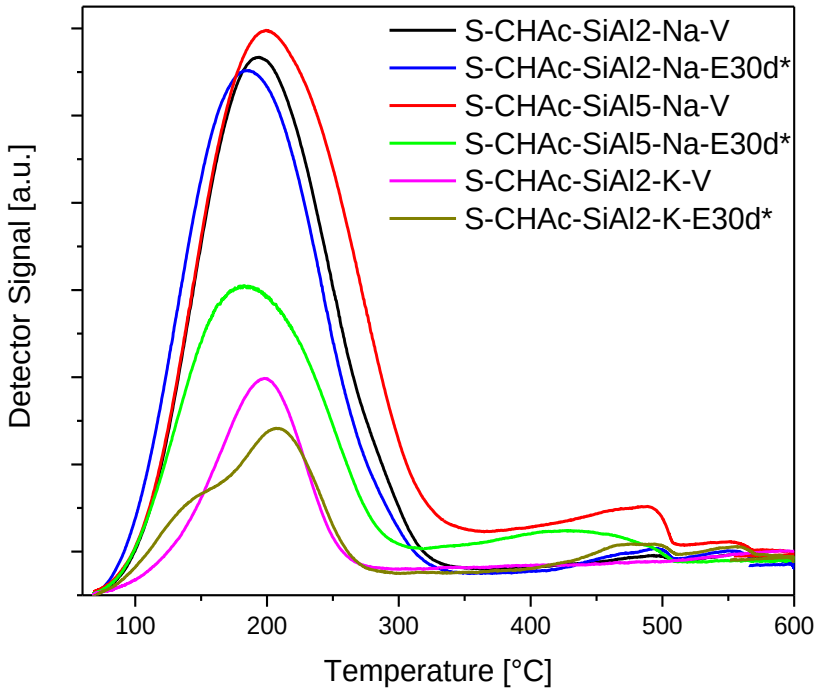

Figure 5.2.4. Detector signal in NH_3 temperature-programmed desorption for the S-CHAc-SiAl(2, 5) –(Na, K) - (V, E30d*) Samples

The samples using an OSDA to direct the structure formation in the synthesis (S-CHAc-SiAl5-Na) require a final step to remove the remaining OSDA located inside the zeolite (Menad et al., 2016). It is important to highlight that all aging protocols, isotherms measurements and physical-chemical characterization were performed only in calcined samples. However, thermogravimetric analysis was performed in the CHA sample with a high *Si/Al* ratio (S-CHAc-SiAl5-Na-V) prior to calcination to better understand the mass loss events with increasing temperature (**Figure 5.2.5(a)**). Two superimposed mass loss events can be observed up to 300 °C and they are associated to the desorption of water and weakly adsorbed species (Burris & Juenger, 2020). A third mass loss event can be observed from 300 °C up to 550 ºC and can be associated with the depletion of the organic compound (OSDA) that remained in the structure (Burris & Juenger, 2020). The calcination temperature was then chosen as 550 ^{o}C to ensure the elimination of all remaining OSDAs while not causing damage to the zeolite crystalline structure. A clear difference is found in the DTG analyses of samples prior (a) and after (b) calcination at 550^{o}C. The presence of organic compound (OSDA) ascribed to the mass loss event observed from 300 °C up to 550 ºC (**Figure 5.2.5(a)**) is no longer present in the calcined sample (**Figure 5.2.5(b)**). Instead, two

superimposed mass loss events are observed in the broad temperature range from 50 °C up to 400 °C, which is attributed to weakly bound atmospheric gases and mostly water desorbed from sites of different strengths in the crystal lattice. From the results obtained with this TG/DTG analysis, the calcination procedure was defined at the temperature of 550 °C for 3 hours to eliminate the remaining OSDAs and preserve the zeolite structure.

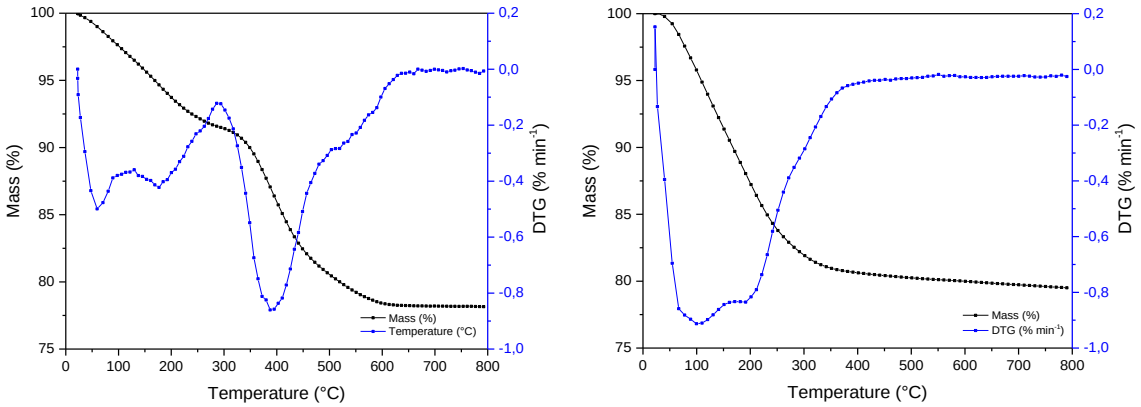

(a) **(b)**

Figure 5.2.5. TG/DTG for pre-calcinated S-CHAc-SiAl5-Na-V (a) and calcinated S-CHAc-SiAl5-Na-V (b)

From TG/DTG analyses, it is possible to infer important information of the samples regarding the variations on temperature. The behavior of this materials with swings in temperature is a keyhole to applications in TSA drying processes. On **Figure 5.2.6**, there are the TG/DTG curves for all pristine and aged CHA samples. In addition, on **Table 5.2.9**, there is data about the mass loss events before and after 300 °C. The temperature of 300 °C is known to be suitable for the desorption of water and weaker adsorbed species (such as CO_2) from zeolite structures. The DTG analyses for the CHA samples with different cations reveal that the mature of the cation impacts the thermal stability of the samples with *Si/Al* = 2 (**Figure 5.2.6**). The pristine material with potassium had a smaller total mass loss (**Table 5.2.9**), which was reached at around 280 °C, the lowest as compared to the other samples. The presence of *K* has a positive influence in the resistance to high temperatures in some zeolites (Cartlidge et al., 1984). Comparing the pristine materials with the same compensating cation (*Na*), but different *Si/Al* ratios, it is possible to infer that the increasing *Si* content leads the material with

earlier mass stabilization (**Figure 5.2.6**) (Cruciani, 2006), though a smaller total mass loss (**Table 5.2.9**). Analyzing aged materials, stabilization of the mass occurs at a higher temperature as compared to the respective pristine material. To corroborate this idea all aged materials presented a higher desorbed fraction above 300 °C, when comparing to the respective pristine material (**Table 5.2.9**), indicating the deposition of contents stronger adsorbed to the surface of the materials. In addition, the sample S-CHAc-SiAl5-Na shows the greatest discrepancy between desorbed mass above 300 °C for the pristine and aged samples. This is another evidence of the increased carbon deposition in this sample, due to EFAls that causes higher acidity in adsorption sites (**Table 5.2.6**).

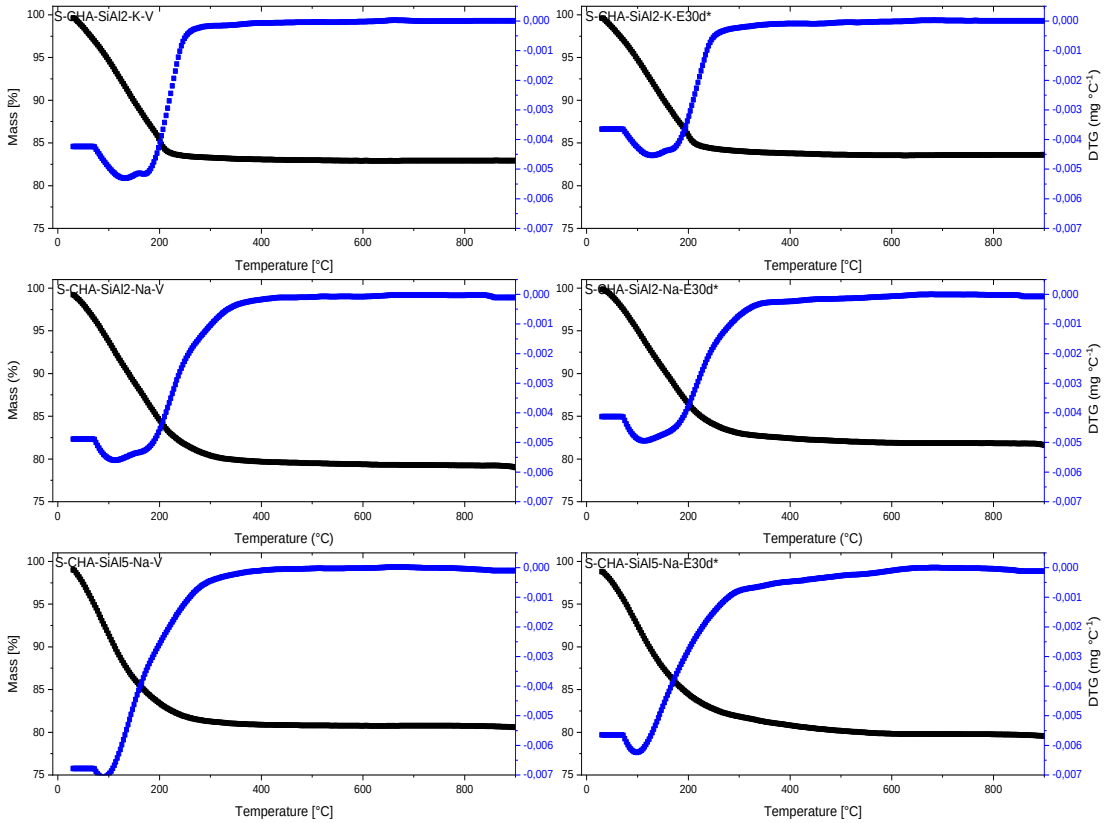

Figure 5.2.6. TG/DTG curves for S-CHAc-SiAl(2, 5)- (Na, K)- (V, E30d*)

Table 5.2.9. Thermal experiments (TG/DTG) for S-CHAc-SiAl(2, 5)- (Na, K)- (V, E30d*)

Sample	Mass Loss [%]	Temperature [°C]	Mass Loss Fraction [%]
S-CHAc-SiAl2-Na-V	19.7	Under 300 °C	93.3
		Above 300 °C	6.7
S-CHAc-SiAl2-Na-E30d*	18.0	Under 300 °C	91.4
		Above 300 °C	8.6
S-CHAc-SiAl2-K-V	16.6	Under 300 °C	97.1
		Above 300 °C	2.9
S-CHAc-SiAl2-K-E30d*	15.9	Under 300 °C	97.0
		Above 300 °C	3.0
S-CHAc-SiAl5-Na-V	18.1	Under 300 °C	97.0
		Above 300 °C	3.0
S-CHAc-SiAl5-Na-E30d*	19.0	Under 300 °C	91.7
		Above 300 °C	8.3

The N_2 isotherms at 77 K of the pristine and aged CHA samples are shown in **Figure 5.2.7**, *Na* containing samples featuring high uptakes at low relative pressures, a typical behavior of microporous solids (Silvestre-Albero et al., 2012). Beyond relative pressure 0.8, all samples show a steep increase in N_2 uptake, which is likely to be due to condensation in interstitial voids between crystals. Analyzing the pristine samples with *Si/Al* ratios 2 and 5 in *Na* form, more adsorbed volume (and hence larger pore volume) is found for the sample S-CHAc-SiAl5-Na-V, which has less cations in the crystalline framework (**Table 5.2.5**) thus allowing for more N_2 to be accommodated in the internal cages. A more drastic effect is observed when the samples with the same *Si/Al* and different compensation metals (*Na* and *K*) are compared. The adsorbed volume of N_2 in the plateau of the isotherm for the pristine *Na* sample is between 80 and 90 $cm^3\ g^{-1}$, whereas the pristine *K* sample adsorbs less than 20 $cm^3\ g^{-1}$. The critical kinetic diameter of cation K^+ is considerably larger than that of Na^+ (Theodore L. et al., 2017), thus hindering the access of N_2 molecules to the cavities. As expected, the aged samples show a decrease in the adsorbed volume in nearly the whole relative pressure range, as compared to the pristine solids, although the isotherm shape remains about the same.

The N_2 uptake reduction is more pronounced in the sample with the lower *Si/Al* ratio in *Na* form, which happens to be the one sample with the lower crystallinity and the largest build-up of carbon on the surface (**Table 5.2.2**). Sample S-CHAc-SiAl5-Na-V, with the highest N_2 uptake, showed a less severe reduction, even though the bulk *C* content was the highest of all samples (**Table 5.2.8**) after aging, indicating that N_2 uptake is mostly dictated by the structural integrity of the zeolite.

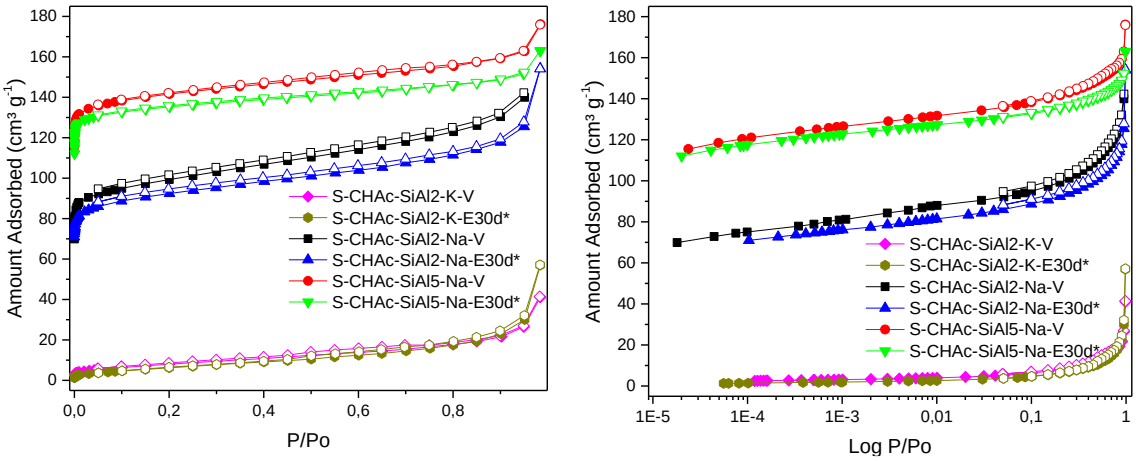

(a) **(b)**

Figure 5.2.7. N_2 isotherms at 77 K in linear (a) and logarithmic (b) scales for S – CHAc - SiAl(2, 5) - (Na, K) - (V, E30d*)

CO_2 isotherms at 273 K for the samples under study are illustrated in **Figure 5.2.8**. Pore windows in some zeolites are so narrow that N_2 would diffuse through in an infinitely long time (e.g. LTA zeolites). The presence of voluminous cations may also lead to this behavior. Hence, the choice of *CO_2* as a probe gas stem from the fact that the analysis is carried out at a considerably higher temperature than N_2 and hence, very small cavities/pores may be accessed with a reasonable analysis time. From the isotherms (**Figure 5.2.8**), it is possible to see that a higher *Si/Al* ratio leads to a higher adsorption capacity for *CO_2*, like N_2, but only at sufficiently high relative pressures. At *CO_2* relative pressure below 10^{-3}, the sample with a more polar surface (S-CHAc-SiAl2-Na) tends to retain more *CO_2*, due to a stronger adsorbent/adsorbate affinity. This affinity can also be explained by the high density of cations in the cage and the presence of both Na and K in significant amounts. As a matter of fact, it has been reported that

CO_2 may interact with more than one cation by forming linearly bridged CO_2 complexes on the dual-cation sites (Pulido et al., 2009). Beyond P/Po = 10^{-3}, larger available pore space becomes the dominant factor that renders sample S-CHAc-SiAl5-Na the highest *CO_2* uptakes. Once again, the samples containing potassium have a smaller adsorption capacity and the isotherm is the least impacted due to hydrothermal aging. The results corroborate that the thermal resistance of these materials is closely related to the *Si/Al* ratio. As the *Si* content increases, the difference between the maximum *CO_2* uptake between the pristine and aged sample decreases. In fact, (Cruciani, 2006) stated that zeolites with a *Si/Al* ratio higher than 3.80 are very stable upon heating.

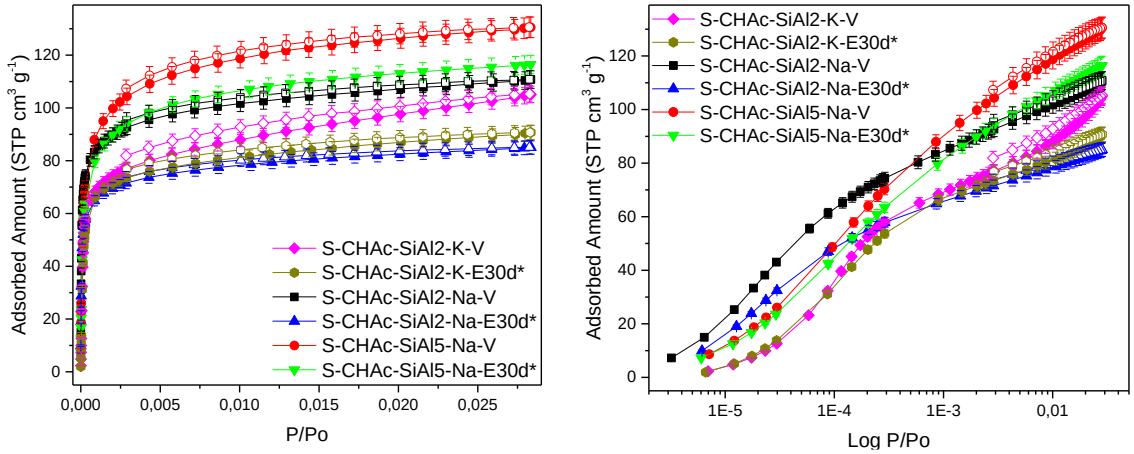

(a) **(b)**

Figure 5.2.8. CO_2 isotherms at 273 K in linear (a) and logarithmic (b) scales for S – CHAc - SiAl(2, 5) - (Na, K) - (V, E30d*)

On **Table 5.2.10**, important parameters to characterize the porous texture of the samples were determined from nitrogen and carbon dioxide adsorption isotherms at 77 and 273 K, respectively. The apparent (BET) specific surface area may be calculated from N_2 isotherms at 77 K and it has become a state-of-the-art methodology for porous solids (Rouquerol, F., Rouquerol, J., Sing, K., Llewellyn, P., Maurin, 2014). Although not physically meaningful for microporous crystalline adsorbents, the BET area may be a useful figure of merit for the sake of comparison of the pore structure of samples. In addition, if the sample contains pore cavities into which *N_2* adsorbs too slowly or does not adsorb at all, *CO_2* adsorption isotherms at 273 K allow for a more precise

calculation of the micropore volume (García-Martínez et al., 2000). The micropore volume of samples S-CHAc-SiAl2-Na, S-CHAc-SiAl5-Na, S-CHAc-SiAl2-K is reduced 22%, 11% and 8%, respectively, after undergoing the aging protocol. On one hand, the higher polarity brought about by the lower *Si/Al* content seems to lead to coke deposition, which obstructs the micropores to some extent (**Table 5.2.8** and **Table 5.2.10**) (Guisnet et al., 1997). On the other hand, even with a low *Si/Al*, the presence of *K* as compensating cation provides a protective effect against aging, also observed in (Sun et al., 2009). This is likely to be due to a sieving effect that prevents the coke precursor (in this case, n-heptane) from accessing the internal cages, *i.e.*, the compensating cation acts as a shape-selective protection against coke deposition. The total porosity (from N_2 isotherms) for the pristine and aged samples with the highest *Si/Al* (**Table 5.2.10**) remains approximately the same, although it retains the largest amount of bulk carbon (**Table 5.2.8**) upon aging. If the carbon content in sample S-CHAc-SiAl5-Na-E30d* refers to physisorbed n-heptane, it is plausible that it is desorbed in the degassing steps prior to the isotherm measurements.

Water vapor adsorption isotherms were measured up to 70 mbar for all CHA samples under study, which is close to the saturation pressure of water at 313 K (**Figure 5.2.9**). In the low-pressure zone (up to 10 mbar), there is a steep increase in uptake, indicating a high adsorbent-adsorbate interaction. A plateau on the adsorbed load is observed for all samples in the pressure range of 10 to 40 mbar. Zeolite S-CHAc-SiAl2-Na, both for the pristine and aged samples, shows a sharp increase at pressures beyond 40 mbar, which was less intense for the other four samples (S-CHAc-SiAl5-Na–(V, E30d*) and S-CHAc-SiAl2-K–(V, E30d*)) (**Figure 5.2.9**). The affinity of protonic zeolites for water molecules is mainly driven by the attraction between polar molecules (e.g. water) and the acid sites caused by unbalanced charges (A. Louis Allred, 1961; Poling et al., 2001), as previously discussed. However, the compensating cations in cationic zeolites also attract water molecules, an example is the zeolite 3A typically applied in drying processes for organics (Cadiau et al., 2017). The electronegativity in water molecules leads to positive and negative charges in *H* and *O*, respectively, and thus the *O* atom in water behaves as a Brönsted Basic Site. On the other hand, the AlO_4^- units that compose the zeolite framework act as a Bronsted Acid Site so that dipole-field interaction causes the retention of the water molecules in the

zeolite cage (Kawai & Tsutsumi, 1992). Therefore, the *Al* content (and hence the *Si/Al* ratio) is a determining factor in water uptake both in cationic and protonic zeolites (Corma & Martinez, 1995; Cruciani, 2006). This explains why the sample S-CHAc-SiAl2-Na-V has a higher adsorption capacity for water than the sample S-CHAc-SiAl5-Na-V, as a result of the higher density of cations. In addition, by comparing the samples S-CHAc-SiAl2-Na-V and the S-CHAc-SiAl2-K-V, the larger size of potassium cation is reflected in a lower water uptake for the latter sample which has practically no *Na* cations (**Table 5.2.5**).

Table 5.2.10. Apparent BET area, pore volume, adsorption capacity and micropore volume for S-CHA$_C$-SiAl(2, 5)-(Na, K)-(V, E30d*)

Sample	from N_2 Isotherms at 77 K		from CO_2 Isotherms at 273 K	
	Apparent BET Area [$m^2\ g^{-1}$]	Total Pore Volume [$cm^3\ g^{-1}$]	Adsorption Capacity * [$cm^3\ g^{-1}$]	Micropore Volume [$cm^3\ g^{-1-}$]
S-CHAc-SiAl2-Na-V	308	0.281	110.7	0.225
S-CHAc-SiAl2-Na-E30d*	267	0.164	85.0	0.174
S-CHAc-SiAl5-Na-V	444	0.227	130.5	0.282
S-CHAc-SiAl5-Na-E30d*	392	0.227	116.4	0.251
S-CHAc-SiAl2-K-V	31	0.031	105.1	0.200
S-CHAc-SiAl2-K-E30d*	13	0.013	90.7	0.184

* At a relative pressure of 0.029

References: (Brunauer et al., 1938; Dubinin, M.M., Radushkevich, 1947)

By comparing pristine and respective aged materials, for *Na*-containing samples, a higher content of *Si* promotes greater hydrothermal stability (Cruciani, 2006), which is confirmed by the isotherms of samples with different *Si/Al* ratios. For the sample with *Si/Al* ratio of 2, the maximum water vapor adsorption capacity decreases by 14% upon aging (**Table 5.2.11**) whereas it decreases by 10% for the sample with higher *Si/Al* ratio. This difference in stability is even more pronounced in the lower pressure range, as observed in the graph in logarithmic scale. Regarding the main compensation metal in the structure (*Na* and *K*), once again the presence of

potassium seems to provide greater thermal stability, as observed in the water isotherms of the pristine and aged sample S-CHAc-SiAl2-K, particularly in the low-pressure range (**Figure 5.2.9(b)**). Note that the size of the compensating cation has a crucial contribution to the adsorption capacity, which is significantly lower for the sample containing *K* than for the sample containing *Na* in the whole pressure range and considering the same *Si/Al* ratio in both pristine samples. Given the robustness of the sample with lower *Si/Al* ratio containing potassium, it may be the adsorbent of choice for prolonged use in cyclic TSA gas drying, despite the significantly higher water uptake of the pristine *Na*-containing zeolite. This is more evident at low relative humidities of the gas phase (below 5 mbar), in which case the loss in water uptake is much more pronounced for the Na-sample (S-CHAc-SiAl2-Na). For humidity values close to the saturation point, the latter sample keeps a relatively high-water uptake, despite a partial deactivation (**Table 5.2.11**).

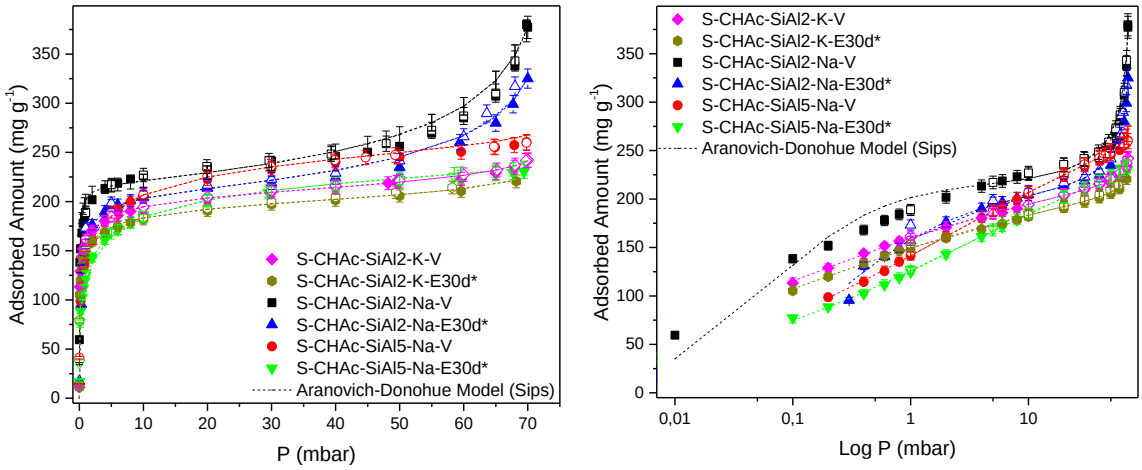

(a) **(b)**

Figure 5.2.9. H_2O isotherms at 313 K in linear (a) and logarithmic (b) scales for S-CHAc-SiAl(2, 5)-(Na, K)- (V, E30d*)

Table 5.2.11. Maximum Water Vapor Adsorption Capacity at 70 mbar for the Samples S-CHAc-SiAl(2, 5) – (Na, K) - (V, E30d*)

Sample		Maximum $H_2O_{(v)}$ Adsorption Capacity [mmol g^{-1}]
S-CHAc-SiAl2-Na	V	20.9
	E30d*	18.0
S-CHAc-SiAl5-Na	V	14.5
	E30d*	12.8
S-CHAc-SiAl2-K	V	13.4
	E30d*	11.7

Experimental data from all isotherms were adequately fitted by the Aranovich-Donohue (AD) model with calculated parameters summarized in **Table 5.2.12**. The (q_{max}) parameter was the highest for the sample with a higher *Si/Al* ratio, less cations and thus larger available micropore volume (**Table 5.2.10**). Parameter (*b*), which accounts for the adsorbent-adsorbate interaction, radically decreases when the *Si/Al* ratio increases, which is consistent with a less ionic framework. The parameter (*n*), which is qualitatively related to the homogeneity of the adsorbent surface, was reduced upon aging for all samples (**Table 5.2.12**). Unlike the Langmuir/Sips model, the AD model satisfactorily described the increase in uptake observed at pressures close to the water vapor saturation pressure, particularly for sample S-CHAc-SiAl2-Na (V and E30d*). Although parameter "e" has no precise physical meaning, it is an empirical constant associated to water clustering or condensation in larger pores or interstitial voids between the zeolite crystals, which seems to be the case for sample S-CHAc-SiAl2-Na.

Table 5.2.12. Parameters from the Aranovich-Donohue Model Fittings of H_2O adsorption isotherms at 313 K for S-CHAc-SiAl(2, 5)-(Na, K)-(V, E30d*)

Sample	Parameters			
	q_{max} [mg g^{-1}]	b [$mbar^{-1}$]	n	e
S-CHAc-SiAl2-Na-V	217.41	16.07	0.90	0.19
S-CHAc-SiAl2-Na-E30d*	208.96	4.09	0.80	0.15
S-CHAc-SiAl5-Na-V	313.59	0.59	0.37	0.02
S-CHAc-SiAl5-Na-E30d*	306.40	0.34	0.34	0.01
S-CHAc-SiAl2-K-V	233.45	9.25	0.35	0.05
S-CHAc-SiAl2-K-E30d*	224.86	7.60	0.34	0.04

SECTION 5.2 - PARTIAL CONCLUSIONS

Chabazite samples were synthesized under different *Si/Al* ratios containing two types of compensating cations in order to investigate the impact of these features in water uptake and their resistance to thermal aging. The aging protocol caused a mild degradation of the crystalline structure of the samples, which was much less severe for samples with higher *Si/Al* and greater content of *K*. All aged materials showed worsened textural characteristics, which seemed directly correlated to the increase in *C* content in the bulk, particularly for the samples with lower *Si/Al* ratio. Interestingly, the aging protocol affected the sample with the highest *Si/Al* (5) to a lesser extent in terms of textural properties and water uptake in spite of having the highest *C* content in the bulk. Despite the low *Al* content, this sample exhibited higher acidity, which was suggested by the unbalance with cations and confirmed by TPD-NH_3 experiments. This particular sample also showed a significant fraction of extra-framework Al, as indicated by RMN, which may be the cause of the observed acidity in NH3 desorption experiments. It may be postulated that the hydrocarbon present in the aging protocol (*n*-heptane) is adsorbed in the pores of the zeolite (Si/Al = 5), given its larger micropore volume and the framework acidity triggers coke formation, which is not severe enough to irreversibly block pores. The presence of potassium as compensating cation also has a great impact on the hydrothermal stability. Due to its larger size as compared to sodium, it is likely that only water molecules have access to the pores reversibly, and not the hydrocarbon present in the aging protocol. As a result, upon aging, it is the one sample with the lowest increase in *C* bulk content and less affected in textural properties and water uptake. Given these characteristics, for prolonged TSA operation, the sample with potassium is likely to provide a better trade-off between thermal stability and water uptake, particularly to dry gases with low relative humidities.

5.3 LINDE TYPE A - LTA

On **Figure 5.3.1**, the XRD diffractograms for all pristine and aged LTA materials are shown. The hydrothermal route adopted to synthesize the adsorbents successfully led to LTA structures, as demonstrated by the similar peaks in the pattern and the obtained samples (Treacy & Higgins, 2007). The main peaks located in the 2θ range from 20° to 32° for *Na*-containing samples with different *Si/Al* ratios (1, 2 and 5) remain in the pristine and aged materials (**Figure 5.3.1(b-d**). The differences in crystallinity are around 3%, which is marginal (**Table 5.3.1**). On the other hand, the *K* sample (**Figure 5.3.1(a)**) shows a drastic loss of crystallinity of approximately 90% upon aging (**Table 5.3.1**). Practically all the peaks vanish in the aged *K* sample diffractogram. Together with the drifting of the baseline, this is clear evidence of structure amorphization. It is known that, under a continuous thermal treatment, the zeolite structure may evolve to a new crystalline phase, which may be predicted by an amorphous phase (Kosanović et al., 1997). Previous studies indicate that LTA in potassium form undergoes amorphization at 960 °C, when heated for 0.5 hours (Kosanović et al., 1997); there may be re-crystallization into kaliophilite and kalsilite, when heated at temperatures above 1000 °C (Dondur et al., 1996). In the present study the S-LTAc-SiAl1-K sample amorphization occurred at a much lower temperature (300 °C), which was maintained for 720 hours (**Figure 5.3.1(a)**). Note that zeolites amorphization is also time dependent (Greaves et al., 2003), so it may have happened to sample S-LTAc-SiAl1-K, despite the relatively low aging temperature. It is generally accepted that the double four-membered oxygen rings (D4R) are the main responsible building unit for the LTA amorphization due to the reduction of the T – O – T bridges that causes the disruption of the sodalite cages (Gulín-González & Suffritti, 2004). In the FTIR spectra shown in **Figure 5.3.**2, the intense band at 558 cm^{-1} (red line) stands for vibrations from the D4R in the pristine materials (S-LTAc-SiAl1-Na-V and S-LTAc-SiAl1-K-V) (**Figure 5.3.2(a)** and **(b)**); a decrease in the intensity of this band is verified in the aged K-containing sample (S-LTAc-SiAl1-K-E30d*) (**Figure 5.3.2(c)**). The large size of the compensating cation (K^+) and the high density of cations at such low *Si/Al* ratio (=1) is expected to play an important role in the permanent structure deformation. Corroborating the previous statement, (Huang & Havenga, 2001) state that zeolites with

lower *Si/Al* ratios are commonly less thermally stable than those with higher *Si/Al* ratios.

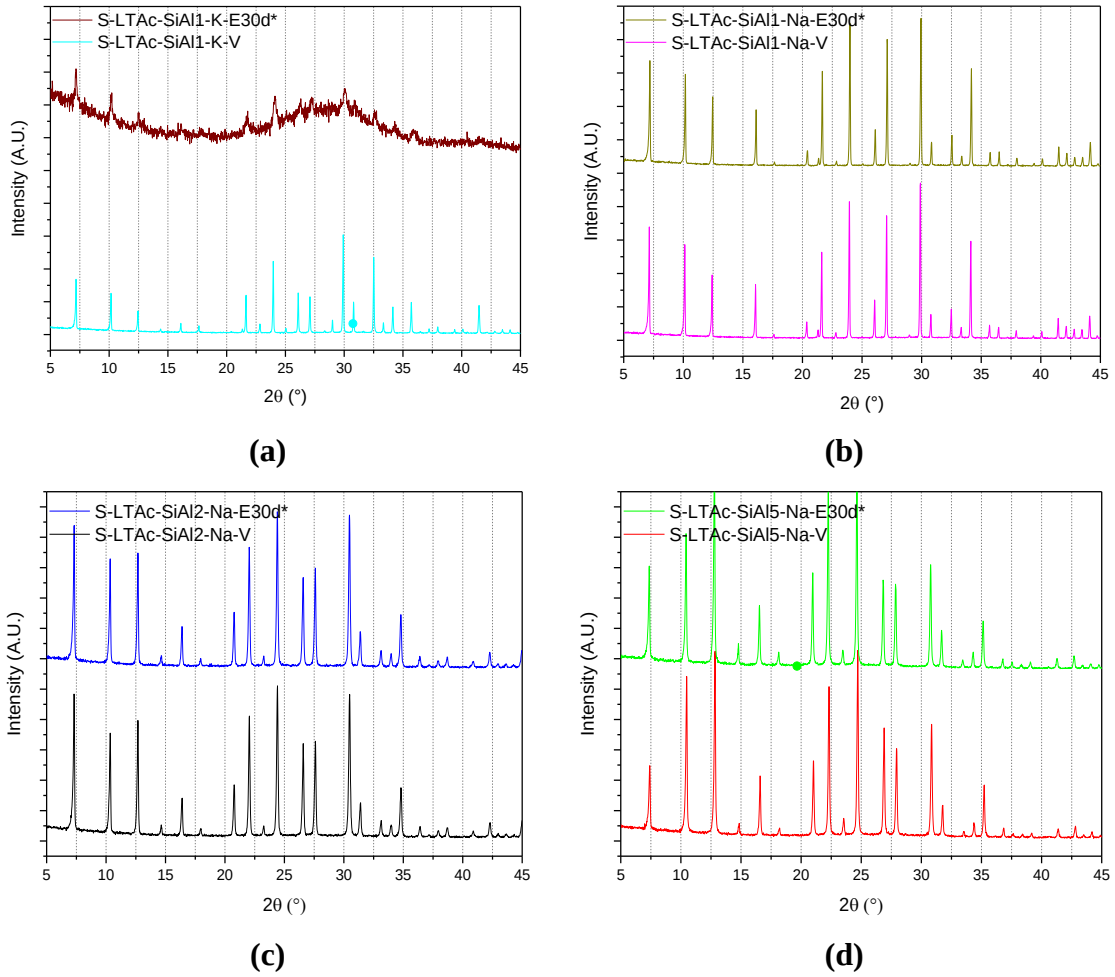

Figure 5.3.1. XRD diffractograms for S-LTA$_C$-SiAl1–K- (V, E30d*) (a), S-LTA$_C$-SiAl1–Na- (V, E30d*) (b), S-LTA$_C$-SiAl2–Na- (V, E30d*) (c) and S-LTA$_C$-SiAl5–Na- (V, E30d*) (d)

Table 5.3.1. Materials crystallinity determined by XRD diffractograms to S-LTAc-SiAl(1, 2, 5)- (Na, K) - (V, E30d*)

Sample	Crystallinity [%]
S-LTAc-SiAl1-K-V	100
S-LTAc-SiAl1-K-E30d*	11
S-LTAc-SiAl1-Na-V	100
S-LTAc-SiAl1-Na-E30d*	93
S-LTAc-SiAl2-Na-V	100
S-LTAc-SiAl2-Na-E30d*	99
S-LTAc-SiAl5-Na-V	100
S-LTAc-SiAl5-Na-E30d*	98

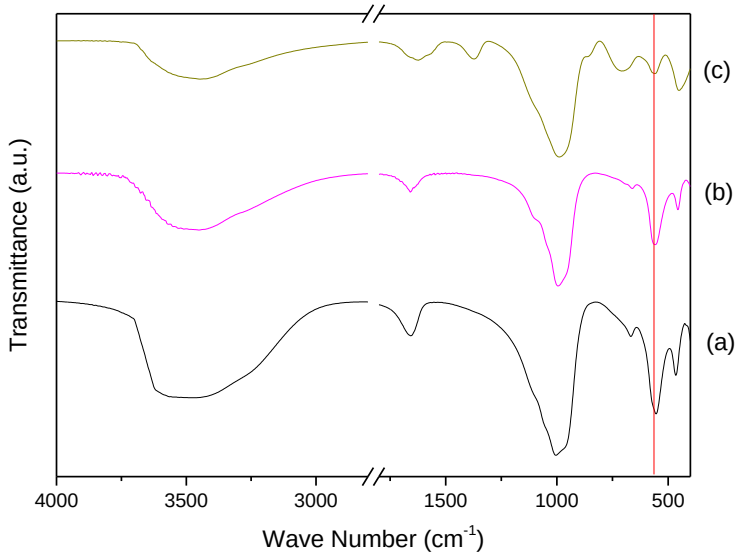

Figure 5.3.2. IR spectra for the *K* samples, S-LTAc-SiAl1-Na-V (a), S-LTAc-SiAl1-K-V (b) and S-LTA$_C$-SiAl1–K-E30d* (c)

The materials surface composition was determined by XPS analyses (**Table 5.3.2**). The carbon content on the surface of pristine materials stands for adventitious carbon, mostly of short chain hydrocarbons species with small amounts of both single and double bound oxygen functionalities (Barr & Seal, 1995; Evans, 1997). The carbon contributions (C *1s*) at binding energies other than ~284.6 eV generally stand for C – C and C – O bonds, respectively (**Table 5.3.3**) and may be related to the coke formation in

aged samples (Guisnet et al., 1997). When the *Si/Al* ratio (**Table 5.3.4**) is compared to the carbon content on the surface (**Table 5.3.2**), more intense carbon deposition is observed with decreasing *Si/Al* ratio. The *Si/Al* ratio is inversely proportional to the *Al* content and, in this turn, to the cation density on the structure. The contributions from *Si 2p* and *Al 2p* are typical of aluminosilicates and so is *O 1s* (Bare et al., 2016; C.D. Wagner, W.M. Riggs, L.E. Davis, J.F. Moulder, 1979). All spectra regions for all identified elements in pristine and aged samples is exposed in the **Supplementary Material**. The theoretical *Si/Al* ratios (from synthesis gels) agree with those found in the XPS analyzes (**Table 5.3.4**), except for the sample with the highest *Si/Al*. The *Si/Al* ratios found by XPS for the pristine and aged materials suggest that *Al* atoms tend to migrate to the bulk of the solid upon aging.

Table 5.3.2. Chemical Surface Composition (% mass concentration) Determined by XPS Analyses for the Samples S-LTA$_C$-SiAl (1, 2, 5)- (Na, K) - (V, E30d*)

Sample	C1s	O1s	Al2p	Si2p	Na1s	K2p
S-LTAc-SiAl1-K-V	36.5	46.2	5.7	6.9	-	4.8
S-LTAc-SiAl1-K-E30d*	25.6	55.6	6.5	8.0	-	4.1
S-LTAc-SiAl1-Na-V	29.0	49.1	6.2	6.2	9.4	-
S-LTAc-SiAl1-Na-E30d*	15.3	59.6	6.9	8.1	10.1	-
S-LTAc-SiAl2-Na-V	25.4	55.9	4.4	10.2	4.0	-
S-LTAc-SiAl2-Na-E30d*	19.6	61.1	4.8	10.9	3.5	-
S-LTAc-SiAl5-Na-V	14.5	68.2	2.2	14.1	1.1	-
S-LTAc-SiAl5-Na-E30d*	19.8	63.7	1.9	13.8	0.7	-

Table 5.3.3. Binding Energy values (eV) end Contributions for the Samples S-LTA$_C$-SiAl (1, 2, 5)- (Na-, K) - (V, E30d*)

Sample	Si2p	Al2p	C1s	O1s	Na1s	K2p3/2
S-LTAc-SiAl1-K-V	101.5	73.7	284.8	530.6	-	293.2
S-LTAc-SiAl1-K-E30d*	102.0	74.1	284.8	531.2	-	293.2
S-LTAc-SiAl1-Na-V	101.6	73.7	284.9 286.2 288.7	530.8 532.3	1072.0	-
S-LTAc-SiAl1-Na-E30d*	101.9	74.0	284.8 286.0	531.2	1072.3	-
S-LTAc-SiAl2-Na-V	102.7	74.6	284.8 286.5 289.2	531.9	1072.5	-
S-LTAc-SiAl2-Na-E30d*	102.7	74.6	284.6 286.0	531.9	1072.5	-
S-LTAc-SiAl5-Na-V	103.1	74.6	284.6 286.2 288.8	532.4	1072.6	-
S-LTAc-SiAl5-Na-E30d*	103.5	75.1	284.9 286.8	532.8	1072.9	-

Table 5.3.4. Obtained *Si/Al* Atomic ratios Determined by XPS Analyses for the Samples S-LTA$_C$-SiAl (1, 2, 5)- (Na, K) - (V, E30d*)

Sample	*Si/Al* atomic ratio
S-LTAc-SiAl1-K-V	1.3
S-LTAc-SiAl1-K-E30d*	1.3
S-LTAc-SiAl1-Na-V	1.0
S-LTAc-SiAl1-Na-E30d*	1.2
S-LTAc-SiAl2-Na-V	2.4
S-LTAc-SiAl2-Na-E30d*	2.4
S-LTAc-SiAl5-Na-V	6.8
S-LTAc-SiAl5-Na-E30d*	7.4

Bulk chemical compositions of the LTA pristine materials were obtained by XRF and ICP-OES (**Table 5.3.5**). X-Ray Fluorescence was also used to confirm the ion exchange procedure (*K* in exchange of *Na* ions*)* performed in the LTA sample with the lowest *Si/Al* ratio (~1.0) (**Table 5.3.5**). The analysis showed that nearly 90% cation exchange was achieved (**Table 5.3.5**). Note that the *Si* and *Al* contents obtained from

XRF analysis confirm the *Si/Al* ratio in the bulk close to 1.00. The carbon deposition upon aging may be affected by the nature of the compensating cations (*Na* and *K*), mainly due to pore accessibility issues posed by the different cation sizes. Furthermore, the cation density and residual acidity (e.g. caused by EFAl) in the framework are also expected to have a role in the carbon deposition (Guisnet et al., 1997). By checking the column *(Na + K)/Al* (**Table 5.3.5**), it is possible to observe that the negative charge generated by *Al* atoms was perfectly balanced in the *K* sample, preventing the formation of strong acid sites. The bulk composition for the samples S-LTAc-SiAl2-Na-V and S-LTAc-SiAl5-Na-V was determined by ICP-OES (**Table 5.3.5**). Small deviations (approximately 3%) from the initially proposed *Si/Al* ratios were found for both pristine samples. By comparing the results for the bulk *Si/Al* ratio (**Table 5.3.5**) obtained either by ICP-OES or XRF to the results found by XPS (**Table 5.3.4**), the *Al* migration from the surface to the inner structure of the solid is corroborated, particularly for the sample with a lower Al content (*Si/Al* = 5) (Moura et al., 2021). The samples with *Si/Al* greater than 1 show an excess of *Al* atoms as compared to the amount of compensating cations (**Table 5.3.5**). In the samples S-LTAc-SiAl5-Na- (V, E30d*) a fraction of the *Al* amount was identified by ^{27}Al NMR as EFAl (**Figure 5.3.3**). When this LTA sample is aged, the EFAls content increased from approximately 9 to 13% in mass (**Table 5.3.6**), increasing the general acidity of the material (C. Liu et al., 2015). On the other hand, no EFAl was identified for the sample with an intermediate *Si/Al* ratio (S-LTAc-SiAl2-Na), which means that excess framework *Al* charge must be neutralized by protons, thus giving rise to Bronsted acid sites.

^{27}Al and ^{29}Si NMR analyses were performed for all pristine and aged LTA adsorbents (**Table 5.3.6**). The presence of EFAl is restricted to the sample with the highest *Si/Al* ratio S-LTAc-SiAl5-Na- (V, E30d*) and it augments with the aging (**Table 5.3.6**). The *Si/Al* ratios were estimated, which remain approximately the same for the pristine and aged samples. Taking into account that *Al* content decreases in some cases on the surface, as indicated by XPS (**Table 5.3.4**), the proposal that *Al* migrates to the inner zeolite structure is plausible (Moura et al., 2021).

Table 5.3.5. XRF for the samples S-LTAc-SiAl1- (Na, K) -V and ICP-OES for the samples S - LTA_C – SiAl (2, 5)– Na– V [*% Weight*]					*(Na + K) /Al*	*Si/Al* Ratio
Sample	*Si*	*Al*	*Na*	*K*		
S-LTAc-SiAl1-Na-V	15.9	12.9	15.1	0.0	1.4	1.2
S-LTAc-SiAl1-K-V	15.8	12.4	0.5	20.0	1.2	1.2
S-LTAc-SiAl2-Na-V	56.7	28.44	14.8	0.0	0.6	1.9
S-LTAc-SiAl5-Na-V	81.0	15.98	3.0	0.0	0.2	4.9

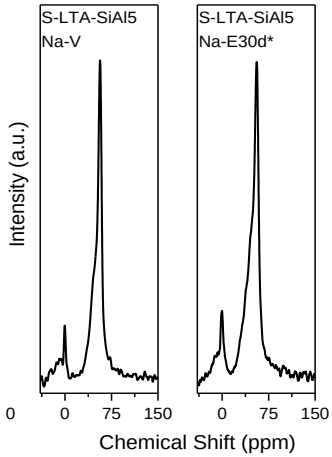

Figure 5.3.3. ^{27}Al NMR spectra for the sample S-LTAc-SiAl5-Na- (V, E30d*)

Table 5.3.6. Si/Al Ratio and EFAl's content [% mass] by NMR Analyses for the S – LTA_C – SiAl (1, 2, 5)– (Na, K) – (V, E30d*) Samples

Sample	Si/Al ratio	*Al* content as EFAls [% Mass]
S-LTAc-SiAl1-K-V	1.0	-
S-LTAc-SiAl1-K-E30d*	1.0	-
S-LTAc-SiAl1-Na-V	1.0	-
S-LTAc-SiAl1-Na-E30d*	1.0	-
S-LTAc-SiAl2-Na-V	2.0	-
S-LTAc-SiAl2-Na-E30d*	2.1	-
S-LTAc-SiAl5-Na-V	5.1	9.1
S-LTAc-SiAl5-Na-E30d*	5.1	13.3

The results of CHN analyses are summarized in **Table 5.3.7** and reveal an increasing content of the bulk carbon upon aging, except for the sample with *Si/Al* = 2. Both samples with the lowest *Si/Al* ratio (S-LTAc-SiAl1- (Na, K)) present a moderate buildup of *C* when compared to that measured for the sample S-LTAc-SiAl5-Na. The sample with an intermediate *Si/Al* ratio (S-LTAc-SiAl2-Na) present the lowest bulk *C* buildup, within the uncertainty of the measurement. In the sample with a high *Si/Al* ratio (**Table 5.3.7**), the significant concentration of extra-framework aluminum (**Table 5.3.6**) contributes to the general zeolite acidity by enhancing the Lewis Acid Sites (C. Liu et al., 2015). These acid sites probably catalyze the reactions of adsorbed hydrocarbons, which find plenty of pore space to be hosted in the zeolite cages (low cation density), thus leading to coke formation (Guisnet et al., 1997). By comparing the results from XPS (**Table 5.3.2**) and CHN (**Table 5.3.7**) for this sample, there is evidence that *C* deposition occurs both in the inner and outer material surface. This contradicts the expected trend that samples with higher *Si/Al* ratio would be more stable and less prone to coke deposition. In fact, this trend is observed for the samples with *Si/Al* ratios of 1 and 2 (the latter sample shows negligible coke formation). However, the trend is not confirmed to the sample with high *Si/Al* ratio, very likely due to the presence of extra-framework *Al* acting as a catalyst of coke formation.

Table 5.3.7. CHN analysis for the Samples S-LTAc-SiAl(1, 2, 5)-(Na, K) - (V, E30d*)

Sample	*C content [%]* Measurement Uncertainty: ± 0.3
S-LTAc-SiAl1-K-V	< 0.3
S-LTAc-SiAl1-K-E30d*	0.9
S-LTAc-SiAl1-Na-V	< 0.3
S-LTAc-SiAl1-Na-E30d*	1.2
S-LTAc-SiAl2-Na-V	< 0.3
S-LTAc-SiAl2-Na-E30d*	0.4
S-LTAc-SiAl5-Na-V	< 0.3
S-LTAc-SiAl5-Na-E30d*	6.9

As mentioned before, each adsorbent sample was obtained from several synthesis batches due to the synthesis low yield, mainly for the sample with a high *Si/Al* ratio (S-LTAc-SiAl5-Na). The verification of similar morphologies by SEM analyses from distinct batches is required before blending them (**Figure 5.3.4**). Cubic crystals, typical of the LTA structure, are large and well defined for the samples in the *K* and *Na*-forms and *Si/Al* ~1, as shown in **Figure 5.3.4 (a)** and **(b)**, respectively. In contrast, the sample with the highest *Si/Al* ratio (**Figure 5.3.4 (d)**) has a poorly defined cubic morphology and tends to form clusters.

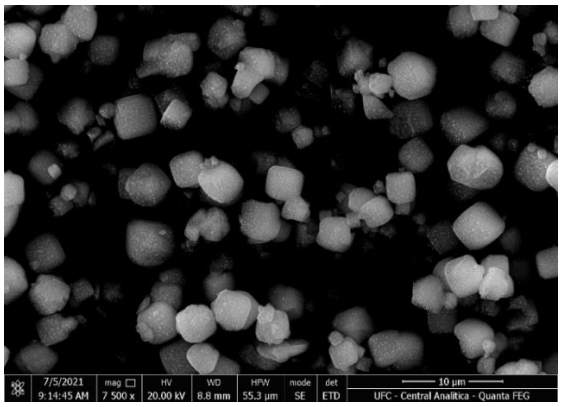

First Batch (mag. 7,500x)

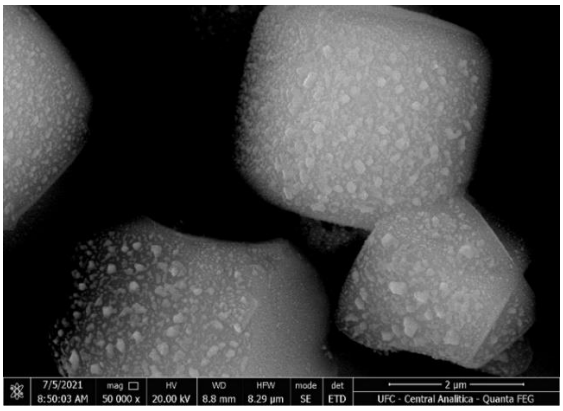

Second Batch (mag. 50,000x)

(a)

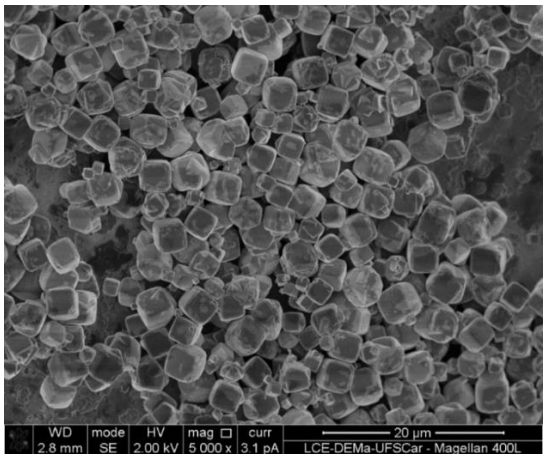

First Batch (mag. 5,000x)

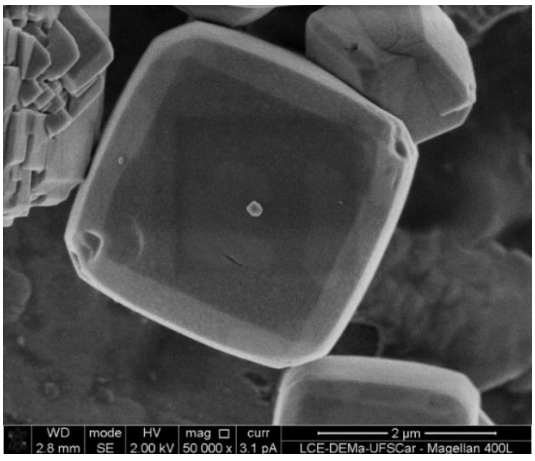

Second Batch (mag. 50,000x)

(b)

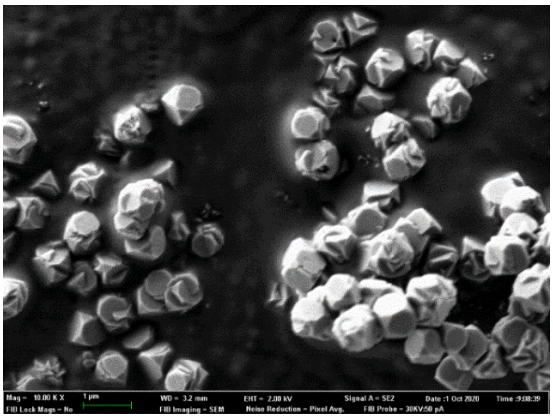

First Batch (mag. 10,000x)

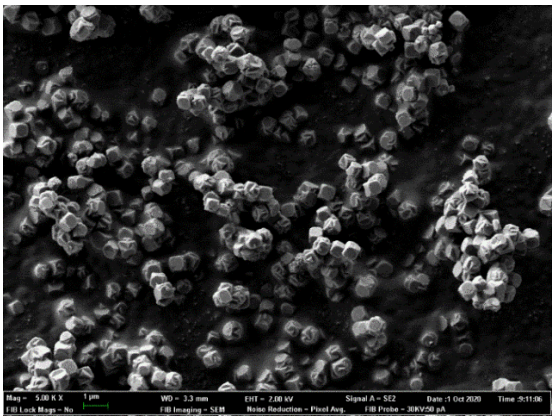

Second Batch (mag. 5,000x)

(c)

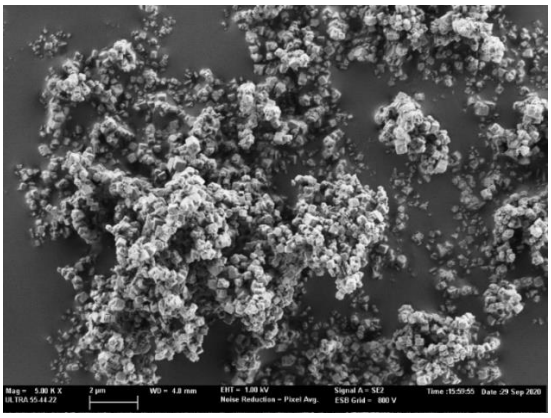

First Batch (mag. 5,000x)

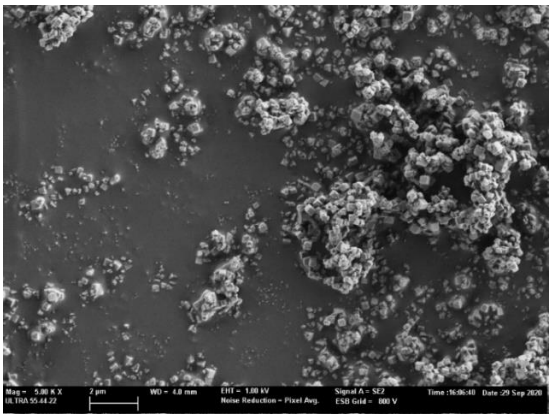

Second Batch (mag. 5,000x)

Figure 5.3.4. SEM analyses for S-LTAc-SiAl1-K-V (a), S-LTAc-SiAl1-Na-V (b), S-LTAc-SiAl2-Na-V (c) and S-LTAc-SiAl5-Na-V (d).

The TG/DTG profiles for all LTA series are exposed in the **Figure 5.3.5**. The summary of events is detailed in **Table 5.3.8**, distinguishing between two mass loss contributions, before and after 300 °C. The main compensating metal (*K*) clearly does not provide a higher stability to the LTA sample with *Si/Al* = 1, which is demonstrated in the nearly flat DTG curve of the aged sample. The curves obtained for the aged *K*-containing LTA corroborate with the amorphization observed in the XRD pattern. For the pristine samples containing *Na* at different *Si/Al* ratios (S-LTAc-SiAl (1, 2, 5)-Na-V), the average mass loss is similar and around 22.6% (**Figure 5.3.5**). However, the peak (before 300 °C) in the DTG curve is more pronounced and occurs at increasingly higher temperatures for decreasing *Si/Al* ratios, which suggests a higher affinity between adsorbed species (water vapor and atmospheric gases) and zeolite frameworks with a high *Al* content. Regarding aged materials, the samples with the lowest (S-LTAc-

SiAl1-Na-E30d*) and the highest (S-LTAc-SiAl5-Na-E30d*) *Si/Al* ratios show significant mass losses above 300 °C (**Table 5.3.8**), which is evident from the peaks shown in the DTG curves in this temperature range. In the sample with *Si/Al* = 5, acid sites are likely to be present in the structure, as suggested by the unbalance between *Na* and *Al* atoms (**Table 5.3.5**) and a considerable amount of EFAl detected by NMR. The higher carbon deposition (**Table 5.3.7**) corroborates with the hypothesis of Lewis acid sites due to EFAl (Jansen, 1998; C. Liu et al., 2015; Park & Seo, 2009). In turn, the sample with *Si/Al* = 1 also has a considerable mass loss above 300 °C, but less pronounced than that for sample with *Si/Al* = 5 and occurring at a less high temperature (lower than 400 °C). Actually, the DTG curve of the pristine sample (S-LTAc-SiAl1-Na-V) also shows a shoulder in the same temperature range. Therefore, the carbon deposit observed for this sample is probably due to the strong polarity brought about by a high density of *Al* and compensating cations in the structure. The strongly bound water may give rise to (Bronsted) acid sites that trigger the polymerization of n-heptane leading to "softer" coke than that formed in the sample with Si/Al = 5. The sample S-LTAc-SiAl2-Na-V also presents an unbalanced charge (**Table 5.3.5**), or excess *Al* in the framework. Nevertheless, negligible carbon deposition (**Table 5.3.7**) is observed, resulting in a modest mass loss above 300 °C (**Table 5.3.8**). Although there is excess *Al* in the structure, the density of cations is half that of the sample with *Si/Al*=1 and no EFAl is present, all of these rendering the sample a stability not found in all others.

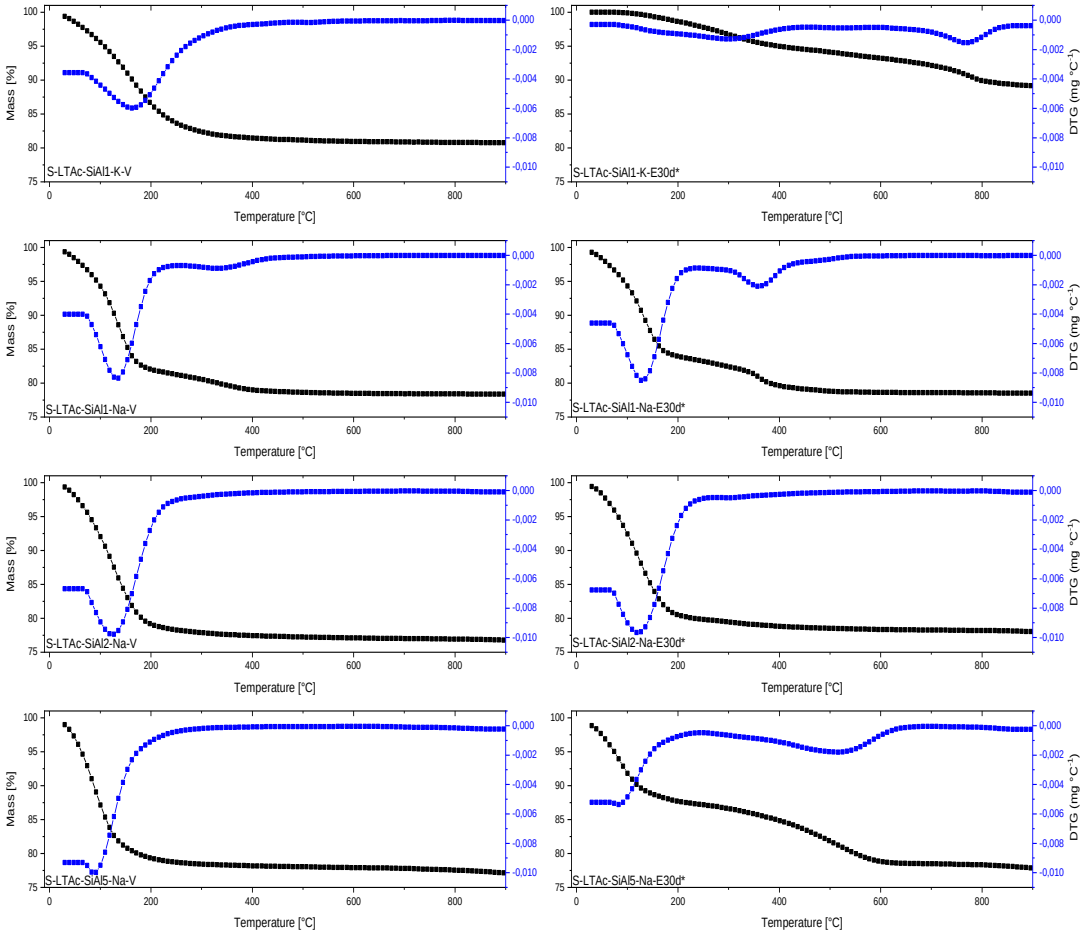

Figure 5.3.5. TG/DTG curves for S-LTAc-SiAl(1, 2, 5)- (Na, K)- (V, E30d*)

Table 5.3.8. Thermal experiments (TG/DTG) for S-LTAc-SiAl(1, 2, 5)- (Na, K)- (V, E30d*)

Sample	Mass Loss [%]	Temperature [°C]	Mass Loss Fraction [%]
S-LTAc-SiAl1-K-V	19.2	Under 300 °C	91.7
		Above 300 °C	8.3
S-LTAc-SiAl1-K-E30d*	11.0	Under 300 °C	30.0
		Above 300 °C	70.0
S-LTAc-SiAl1-Na-V	21.7	Under 300 °C	89.4
		Above 300 °C	10.6
S-LTAc-SiAl1-Na-E30d*	21.5	Under 300 °C	81.9
		Above 300 °C	18.1
S-LTAc-SiAl2-Na-V	23.2	Under 300 °C	95.2
		Above 300 °C	4.8
S-LTAc-SiAl2-Na-E30d*	22.0	Under 300 °C	93.6
		Above 300 °C	6.4
S-LTAc-SiAl5-Na-V	22.9	Under 300 °C	94.3
		Above 300 °C	5.7
S-LTAc-SiAl5-Na-E30d*	22.1	Under 300 °C	60.6
		Above 300 °C	39.4

From CO_2 isotherms at 273 K for all pristine and aged LTA samples (**Figure 5.3.6**), it is possible to see that the *Si/Al* ratio and the main compensating cations have a massive impact in the adsorbed concentrations as a function of pressure. The same group of isotherms is presented in linear (**Figure 5.3.6(a)**) and logarithmic scales (**Figure 5.3.6(b)**), the latter allowing to highlight the low-pressure range. The abrupt rise presented by the isotherms up to a relative pressure of 0.01 indicates a strong adsorbent-adsorbate interaction. The higher the content of *Al* is, or the lower the *Si/Al* ratio, the higher uptake is observed at low pressures (**Figure 5.3.6(b)**). This high adsorbate/adsorbent affinity may be explained by the high cations density, which enhances the affinity for CO_2 molecules. After $P/Po = 10^{-3}$, S-LTAc-SiAl(1, 2)-Na-(V, E30d*) samples reach a plateau of adsorbed concentration which do not present

expressive variations. At this point, the adsorption uptake is majorly dictated by the available pore volume in the zeolitic structures, which is higher for lower density of cations. For virgin zeolites, at sufficiently high pressures, the uptake of the *Na* sample with *Si/Al* = 2 surpasses that of the sample with *Si/Al* = 1 and an analogous trend is expected for the pristine sample with *Si/Al* = 5, if its isotherm could be extrapolated. The aged sample with an intermediate *Si/Al* ratio (~2) is not show a considerable variation in the CO_2 adsorption isotherm (**Figure 5.3.6**, **Table 5.3.9**). This result is corroborated by the lowest *C* deposition between all aged materials (**Table 5.3.7**) and the very similar TG/DTG curves between pristine and aged samples. The sample with a high *Si/Al* ratio (S-LTAc-SiAl5-Na) presents a modest adsorption capacity at low relative pressures (up to 10^{-3}), which agrees with the low *Al* content in the structure and hence much less polar framework. At relative pressures above 10^{-3}, the increase in adsorbed concentration presented by the S-LTAc-SiAl5-Na-V is much steeper than any other LTA material, which is better seen in the log scale (**Figure 5.3.6(b)**). The maximum adsorbed amount reaches the same level of the S-LTAc-SiAl1-Na-V sample (**Table 5.3.9**), with a trend to go beyond as a consequence of the much larger pore space in this sample. In the pristine and aged *Na* sample with *Si/Al* = 5 (**Figure 5.3.6(a)**), it is possible to observe much more smooth-growing isotherms in comparison to other similar materials. The rectangular character of the isotherms is proportional to the adsorbent/adsorbate affinity; hence a low affinity is confirmed for this sample containing lesser Al. The aged sample (S-LTAc-SiAl5-Na-E30d*) shows the lowest adsorption capacity of all *Na*-containing samples, mainly due to the highest carbon deposition (**Table 5.3.7**) whose formation is likely to be related to the EFAl content (**Table 5.3.6**). The larger cation size of K and its high density in the sample with *Si/Al* = 1 may have decreased significantly the accessibility of CO_2 molecules to the pores (Brown et al., 2012). With the aging protocol, the intermediary carbon deposition present by *K*-form sample (**Table 5.3.7**) together with the amorphization of the zeolite structure (**Figure 5.3.1**) led to an uptake reduction of approximately 90% (**Table 5.3.9**).

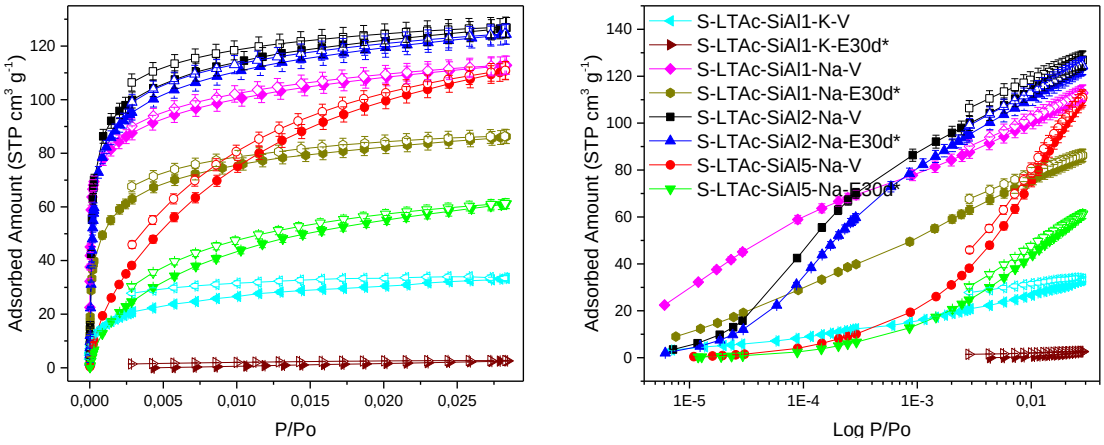

(a) **(b)**

Figure 5.3.6. CO_2 isotherms at 273 K in linear (a) and logarithmic (b) scales for S-LTAc-SiAl(1, 2, 5) - (Na, K) - (V, E30d*)

To measure the accessible micropore volume, the Dubinin-Radushkevich equation (Dubinin, M.M., Radushkevich, 1947)was applied to *CO₂* isotherms at 273 K (García-Martínez et al., 2000) (**Figure 5.3.6**) and the results are summarized on **Table 5.3.9**. The sample in *Na*-form with a *Si/Al* ratio of 1 presents a moderate decrease in the micropore volume from pristine to the aged material, approximately 15%. Possibly the high *Al* content (**Table 5.3.5**), enhance the acidity, this in turn, favors de coke deposition (**Table 5.3.7**) that obstruct the pores (Guisnet et al., 1997). The porosity of the sample S-LTAc-SiAl2-Na presented the lowest decrease in micropore volume upon aging (**Table 5.3.9**), which is corroborated by the lowest *C* deposition (**Table 5.3.7**). As expected, the pristine sample S-LTAc-SiAl5-Na-V has the highest micropore volume (**Table 5.3.9**) but undergoes the sharpest decrease in micropore volume of al *Na*-samples upon aging (**Table 5.3.9**), prompted by the *C* deposition (**Table 5.3.7**) associated with the excess *Al* in the form of EFAl. Concerning the *K*-containing sample (S-LTAc-SiAl1-K), the pristine material already has a small micropore volume, mainly due to the large compensating cation size (K^+). Not only the *C* deposition in the aged material obstructs the pores accessibility, but the destruction of the crystalline structure (amorphization) explains the drastic drop in the micropore volume.

Table 5.3.9. Adsorption capacity and micropore volume by CO_2 isotherms for S-LTA$_C$-SiAl (1, 2, 5)-(Na, K)-(V, E30d*)

Samples	Maximum Adsorption Capacity * [$cm^3\ g^{-1}$]	Micropore Volume [$cm^3\ g^{-1}$]
S-LTAc-SiAl1-K-V	33.5	0.086
S-LTAc-SiAl1-K-E30d*	2.7	0.005
S-LTAc-SiAl1-Na-V	112.9	0.240
S-LTAc-SiAl1-Na-E30d*	75.1	0.202
S-LTAc-SiAl2-Na-V	127.0	0.309
S-LTAc-SiAl2-Na-E30d*	124.5	0.278
S-LTAc-SiAl5-Na-V	110.9	0.430
S-LTAc-SiAl5-Na-E30d*	61.3	0.208

* At a relative pressure of 0.029

References: (Brunauer et al., 1938; Dubinin, M.M., Radushkevich, 1947)

Water vapor adsorption isotherms at 313 K were measured for all LTA samples in a pressure range up to 70 mbar (**Figure 5.3.7**). The high adsorbent/adsorbate interaction is demonstrated by the sharp rise in adsorbed concentration in all materials, except for the aged *K*-containing sample. In the pressure range up to 10 mbar, for Na-containing samples, the *Al* content is proportional to the framework polarity and hence its hydrophilicity, *i.e.*, the sample with *Si/Al* = 1 shows the highest H_2O uptakes, followed by that with *Si/Al* = 2 and that with *Si/Al* = 5. The attraction for water molecules in cationic zeolites is driven by a dipole-field interaction (Kawai & Tsutsumi, 1992). The different electronegativity presented by *H* and *O* in water molecules, makes *O* atom work as a Brönsted Acid Site (BAS). In contrast, the tetrahedral *Al* in the zeolites PBUs works as a Brönsted Basic Site, thus providing an acid and base interaction. Beyond 10 mbar, the low (1) and intermediate (2) *Si/Al* ratio samples reach a plateau on the adsorbed concentration, which is roughly constant in the range from 10 to 50 mbar. Above 50 mbar, the higher accessible volume of the *Na*-sample with *Si/Al* = 5 allows for a continuous increase in uptake. The sample containing *K* has a considerably lower uptake as compared to the *Na* sample of the same *Si/Al* ratio due to the larger size of the potassium cation. Following the previous discussion for the aged

K-sample, water uptake is also marginal. The XRD pattern clearly indicated the framework collapse due to the rupture of D4R rings (**Figure 5.3.1** e **5.3.2**), which had already been reported by (Kosanović et al., 1997).

Regarding the *Na*-containing samples, the one with intermediate (2) *Si/Al* ratio was less affected by aging than the sample with a low *Si/Al* ratio (1) (**Table 5.3.10**), which is more evident in the range from 5 to 50 bar. In fact, Cruciani, 2006 states that the *Si* forms a more stable bond with the *O* atom than *Al*, which enhances the hydrothermal stability. Therefore, the aging protocol, at least under the present conditions, did not lead to a considerable decrease in water adsorption for the sample with *Si/Al* = 2 (**Figure 5.3.7**). It would be expected that the sample with the highest *Si/Al* ratio (5) would be even more resistant to aging because of its much more neutral framework. Nevertheless, it is the one *Na*-containing samples with the highest drop in water uptake upon aging. As previously discussed, this is also the sample with the largest fraction of *Al* present outside the framework (**Table 5.3.6** and **Figure 5.3.3**). EFAl provides Lewis acid sites that probably catalyzed coke formation, indicated by the carbon deposition (**Table 5.3.7**) and decrease in textural properties (**Table 5.3.9**).

Experimental adsorption data **(Figure 5.3.7)** was adjusted by the AD model, which theoretically estimates the contribution from the monolayer (or adsorption in the crystalline framework) and subsequent layers (or adsorption in larger pores due to crystal defects or interstitial voids). The model parameters are summarized in **Table 5.3.11**. The parameter that accounts for the maximum adsorption uptake (q_{max}) is mainly influenced by the accessible pore volume. Hence, the sample S-LTA-SiAl5-Na-V - with the highest micropore volume (**Table 5.3.9**) due to the low cation density - has the highest (q_{max}) value (**Table 5.3.11**). On the other hand, the sample with a low *Si/Al* ratio (i.e., a high content of compensating cation) and a large cation size, S-LTAc-SiAl1-K, has the smallest available pore volume and thus, the smallest (q_{max}) parameter. The impact of aging in the *K* sample, S-LTAc-SiAl1-K-E30d*, reduces even more the (q_{max}) parameter (**Table 5.3.11**). The parameter (*b*) is related to the adsorbent/adsorbate interaction; it consistently decreases in magnitude for the aged samples as compared to the pristine counterparts. Concerning the non-aged materials, the S-LTAc-SiAl1-Na-V

sample has the highest value of *b* parameter (7.98) (**Table 5.3.11**), which is consistent with its sharpest rise in the adsorption isotherm in the low-pressure zone (**Figure 5.3.7**). The homogeneity of adsorption sites is qualitatively assessed by the parameter (*n*), which is reduced in all cases after aging, though very modestly for the *Na* samples with low and intermediate *Si/Al* (**Table 5.3.11**). Lastly, the (*e*) parameter is related to the clustering and condensation of water molecules in larger voids. The closer it gets to unity, the more intense will be the rise in uptake close to the saturation pressure. For the samples under study, all "e" values are relatively small, except for the aged *K* sample and the aged *Na* sample with the largest *Si/Al* (=5). As a matter of fact, these two aged samples experienced the most pronounced carbon deposition and are likely to adsorb much less water in voids other than the zeolite cavities, which have been mostly blocked by coke (S-LTAc-SiAl5-Na-E30d*) or collapsed (S-LTAc-SiAl1-K-E30d*).

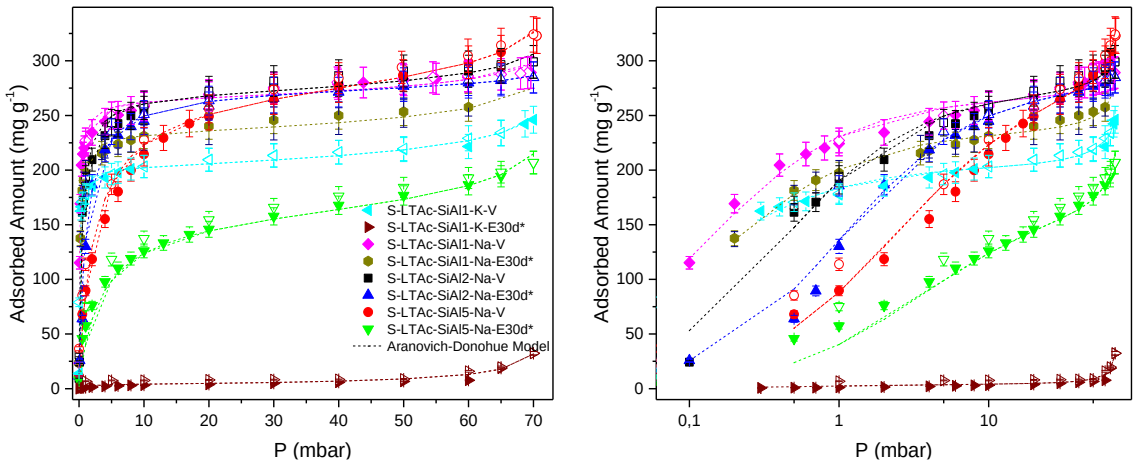

Figure 5.3.7. H_2O isotherms at 313 K in linear (a) and logarithmic (b) scales for S-LTAc-SiAl(1, 2, 5)- (Na, K) - (V, E30d*)

Table 5.3.10. Water Vapor Adsorption Capacity at 0.1, 1, 10 and 70 mbar for the Samples S-LTAc-SiAl(1, 2, 5) – (Na, K) - (V, E30d*)

Sample		$H_2O_{(v)}$ Adsorption Capacity [mmol g^{-1}]			
		0.1 mbar	1.0 mbar	10.0 mbar	70.0 mbar
S-LTAc-SiAl1-K	V	6.17	10.21	11.23	13.75
	E30d*	0.04	0.13	0.23	1.76
S-LTAc-SiAl1-Na	V	6.61	12.80	14.55	16.50
	E30d*	5.54	11.14	12.85	15.27*
S-LTAc-SiAl2-Na	V	2.95	10.57	14.47	17.00
	E30d*	1.36	7.55	13.92	15.93
S-LTAc-SiAl5-Na	V	0.83*	4.89	12.40	18.27
	E30d*	0.33*	2.24	6.88	11.93

* Estimated from the Aranovich-Donohue model

Table 5.3.11. Parameters Used in Aranovich-Donohue Model Fitting for H_2O Isotherms at 313 K for S-LTAc-SiAl (1, 2, 5) – (Na, K) - (V, E30d*)

Sample	Parameters			
	q_{max} [mg g^{-1}]	b [$mbar^{-1}$]	n	e
S-LTAc-SiAl1-K-V	202.79	12.36	0.90	0.07
S-LTAc-SiAl1-K-E30d*	4.15	1.38	0.80	0.70
S-LTAc-SiAl1-Na-V	265.30	7.98	0.91	0.04
S-LTAc-SiAl1-Na-E30d*	234.48	7.17	0.90	0.06
S-LTAc-SiAl2-Na-V	270.13	2.41	0.99	0.04
S-LTAc-SiAl2-Na-E30d*	275.01	0.97	0.98	0.02
S-LTAc-SiAl5-Na-V	281.05	0.42	0.91	0.06
S-LTAc-SiAl5-Na-E30d*	165.32	0.30	0.90	0.11

SECTION 5.3 – PARTIAL CONCLUSIONS

In order to assess water adsorption and hydrothermal stability, LTA samples were synthesized under three different *Si/Al* ratios (1, 2 and 5), one of them containing two types of compensating cations (*Na, K*). The aging protocol caused a moderate to intense degradation in LTA adsorbents, which was found to be related to the framework polarity, extra-framework *Al* and cation size. The *Si/Al* ratio per se did not impact in the crystallinity upon aging, but the presence of a high density of potassium (*Si/Al* = 1) led to the amorphization of the zeolite structure. The results from the XPS and NMR techniques indicate that *Al* migration from the outer surface to the inner cages is occurring with aging. Chemical analysis by XRF and ICP-OES associated with ^{27}Al NMR analysis reveal that the presence of EFAl is particularly significant in the sample with the largest *Si/Al* ratio and is correlated to a much larger *C* deposition upon aging. Contrary to what would be expected for a nearly apolar framework, the aged *Na* sample with *Si/Al* = 5 had the most drastically affected textural features, such as, the available micropore volume, identified by the CO_2 isotherms at 273 K. In addition, SEM images showed the evolution of the classical cubic morphology of LTA crystals into clusters/aggregates as the *Si/Al* ratio increases. Likewise, these findings were reflected in the water adsorption isotherms of pristine and aged samples. The *Al* content showed is proportional to the water adsorption uptake, particularly at low pressures (below 10 mbar). The samples with an intermediate (2) and low (1) *Si/Al* ratios presented a high affinity for water molecules, giving rise to very rectangular-shaped isotherm. The material with an intermediate *Si/Al* ratio and in *Na*-form (S-LTAc-SiAl2-Na) combines excellent hydrothermal stability to a high water affinity and uptake. Though a longer aging protocol is still required, for prolonged TSA operation, the sodium sample with *Si/Al* = 2 seems to be the best choice.

5.4 CHABAZITES (CHA) x LINDE TYPE A (LTA)

On **Figure 5.4.1**, a summary of the adsorption experimental data from CHA and LTA materials for CO_2 at 273 K and H_2O at 313 K isotherms are exposed. On **Figure 5.4.1**, all black points stand for CHA experimental data and red points account for LTA experimental data. Analyzing the water adsorption capacity of both zeolite structures (**Figure 5.4.1(a)** and **(b)**), experimental evidence indicates that LTA samples are more susceptible to hydrothermal aging than CHA samples. This finding is also corroborated by (Park & Seo, 2009) who report that CHA materials have a slower deactivation. Possibly, the faster deactivation presented by LTA samples is mainly caused by the large cages (α cages) that allow for the formation of branched species (e.g. as a result of condensation/polymerization reactions), enhancing the deactivation by coke deposition. In contrast, the more compact cages from CHA structure would suppress the formation of larger compounds (Park & Seo, 2009). Framework Density (FD), which relates the number of tetrahedral units (*T*) per unit volume (nm^3), is higher for CHA (14.5) than LTA (12.9) and also contributes to the higher stability presented by the former material upon aging (Ch. Baerlocher, Lynne B. McCusker, 2007). In general, all pristine and aged materials presented a steep increase in water uptake at the low-pressure range, indicating a strong adsorbent/adsorbate affinity, followed by a plateau from 10 to 50 mbar. Some samples show another uptake rise close to the saturation pressure (above 50 mbar at 313 K), as a result of water clustering/condensation in large voids (e.g. interstitial pores). From CO_2 at 273 K isotherms (**Figure 5.4.1(c)** and **(d)**), the superior hydrothermal stability of CHA over LTA can be also observed. As expected, the isotherm shape of nearly all samples confirms that they are essentially microporous (Thommes et al., 2015), all pristine materials present a higher adsorption capacity than aged samples.

Legend: [black] Chabazite and [red] LTA materials.

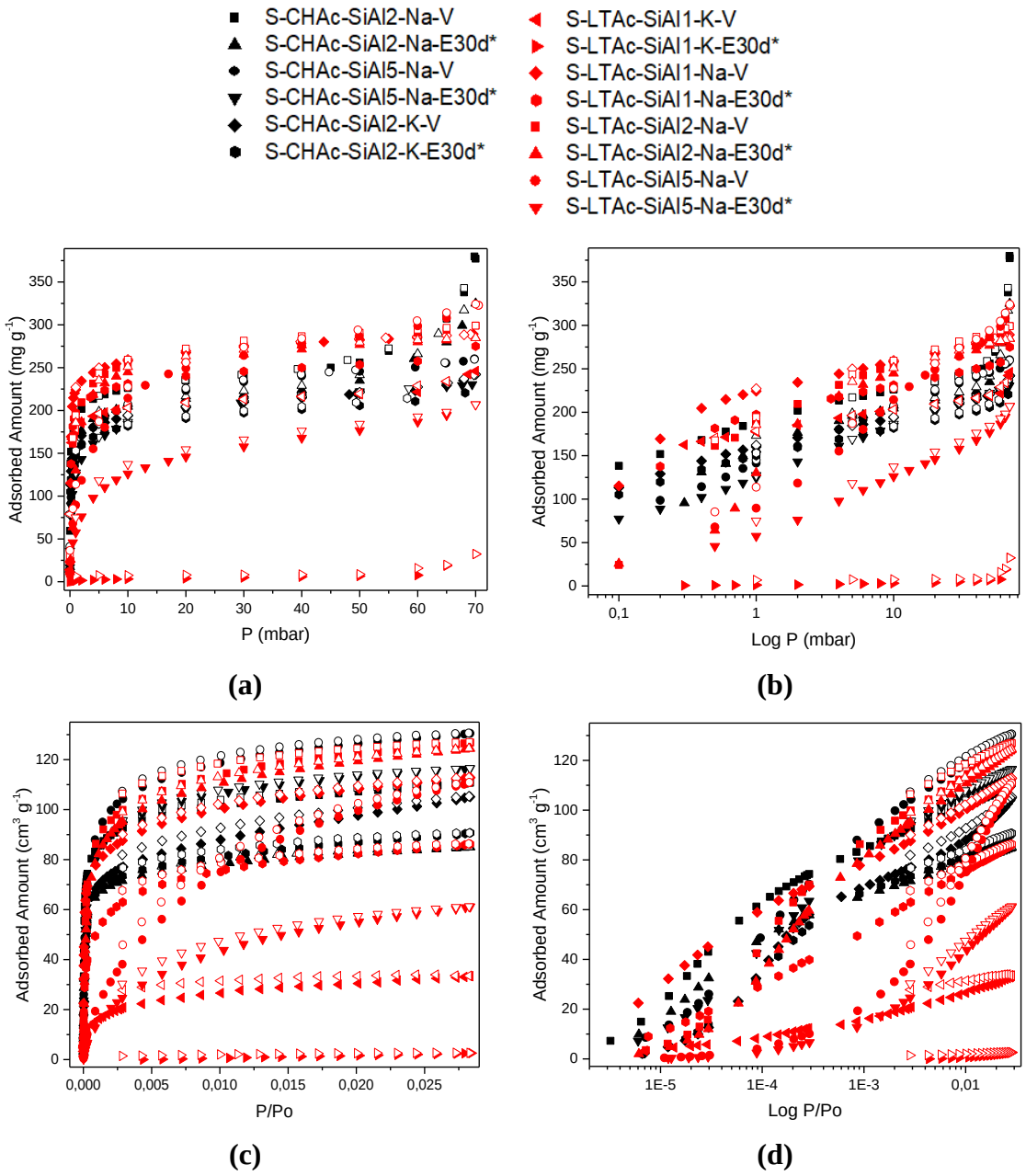

Figure 5.4.1. H_2O isotherms at 313 K in linear (a) and logarithmic (b) scales and CO_2 isotherms at 273 K in linear (c) and logarithmic (d) scales for all studied samples

Except for LTA sample with *K* as compensating cation (S-LTAc-SiAl1-K), XRD diffractograms for all other materials (**Figure 5.2.1** and **5.3.1**) showed no massive impact on crystallinity upon aging. XPS analysis showed an increase in *Si/Al* ratio at the external surface of aged zeolite materials proportional to aging time, *i.e.*, the material (S-CHAc-SiAl2-Na-E60d) that was aged for 60 days (longest time) presented the higher *Si/Al* ratio increase (**Table 5.1.3**). On the other hand, NMR results presented a

constant value for this ratio in the bulk composition of all samples. Therefore, it is possible to infer that the aging protocol causes the *Al* migration from the external surface to the inner cavities of the adsorbents. Another important feature also verified by XPS (**Table 5.2.2** and **5.3.2**) and CHN (**Table 5.2.8** and **5.3.7**) analyses was the *C* deposition, which has a key role in the sample deactivation (Guisnet & Magnoux, 1989) (**Figure 5.4.2**). Pristine materials present a negligible *C* content, however most aged materials present a considerable amount of carbon (**Figure 5.4.2**). Both zeolite structures (CHA and LTA) with a high *Si/Al* ratio (=5) show excess *Al* (as compared to the amount of compensating cations) located outside the framework (EFAl), which leads to an appreciable increase of carbon content in the bulk compositions (Guisnet & Magnoux, 1989), this trend being more pronounced in LTA. The material S-CHAc-SiAl2-K has the lowest carbon deposition between all aged materials, preventing the coke formation with a protective sieving effect of the cation (*K*) into the CHA structure against the carbon deposition. The same did not happen to the *K*-containing LTA sample, which suffered from amorphization of the structure upon aging, possibly because of the low *Si/Al* content and much higher (large) cation concentration than in the case of the potassium CHA. Although there was also an unbalanced charge between *Al* and (*Na* + *K*) cations in the *Na*-LTA sample with *Si/Al* ratio equal to 2, the excess *Al* was not associated to EFAl content and did not have a considerable impact on the carbon deposition upon aging. It would be enlightening to identify the nature of the carbon deposition in the LTA samples with Si/Al equal to 1 (low) and 5 (high) because they seem to have a different nature, as suggested by the TG/DTG profiles. While the former (*Si/Al* = 1) seems to be due to the framework high polarity, the latter (*Si/Al* = 5) is likely to be caused by the acid character of the EFAl. To identify the composition of the carbon deposition (coke formation) is not an easy task however, due to a mixed content of organic compounds and the need to remove them from the zeolite lattice (Guisnet & Magnoux, 1989). (Nascimento et al., 2021) identified (alkyl) aromatic compounds in aged LTA materials and aliphatic compounds in aged CHA materials.

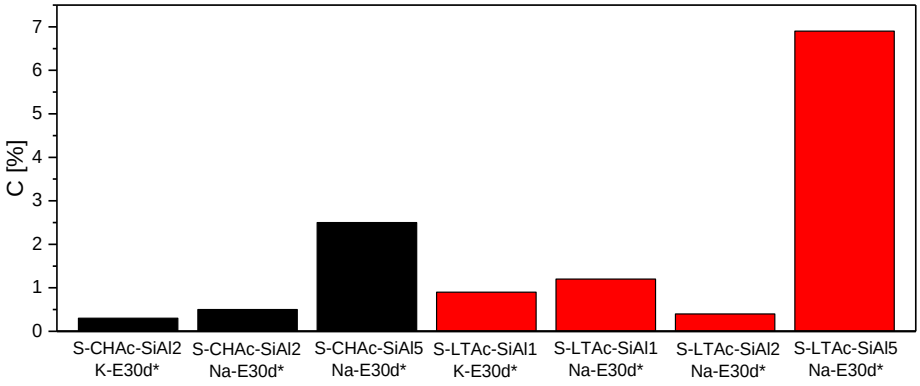

Figure 5.4.2. *C* bulk content in the aged CHA and LTA samples

In order to compare the carbon deposition during the aging protocol in the different zeolite structures (CHA and LTA), the main compensating cations (*Na* and *K*) and the *Si/Al* ratio (1, 2 and 5) are suggested as indicators. First, the (φ) parameter was proposed (**Table 5.4.1**) as the difference in the water uptake at 70 mbar and 313 K between the pristine and the respective aged sample (**Table 5.2.11** and **5.3.10**) divided by the bulk *C* concentration in the aged sample (**Table 5.2.8** and **5.3.7**). Second, the (λ) parameter (**Table 5.4.1**) stands for the loss in micropore volume upon aging, as obtained from CO_2 isotherms at 273 K (**Table 5.2.10** and **Table 5.3.9**), divided by the bulk *C* deposition (**Table 5.2.8** and **5.3.7**). The φ and λ parameters are not shown for material (i) because of the negligible *C* deposition in the inner (**Table 5.2.8**) and outer (**Table 5.2.2**) surfaces. From **Table 5.4.1**, φ parameter indicates that materials (iii), (v) and (vii) were the least affected by carbon deposition in terms of water uptake. These samples maintain a strong hydrophilicity despite aging. Possibly the affinity for water molecules is associated with the acid sites caused by *Al* in EFAl in high *Si/Al* ratio samples (**Table 5.2.6** and **5.3.6**). The materials (iii) and (vii) (**Table 5.4.1**) maintained the porosity and hydrophilicity upon aging, which is corroborated by (Cruciani, 2006) who claim that materials with *Si/Al* ratio > 3.8 have a high thermal stability. The EFAl content in both materials demonstrated to have a key role in the carbon deposition, enhancing the general acidity of the material. However, the excess *Al* may cause pore blocking, decreasing the adsorption capacity (M.-C. Silaghi et al., 2016). Regarding the sample (v), no EFAl content was identified, but the high content of *Al* in the framework renders it a high polar character. Nevertheless, the *C* deposition upon aging had a modest impact on water adsorption of the sample (v), which is also corroborated by a high adsorbent/adsorbate *b* parameter both for the pristine and aged samples (**Table**

5.3.11). The sample (vi) has unbalanced charge between *Na* and *Al* revealed by ICP-OES analyzes (**Table 5.3.5**) and no EFAl were identified by NMR analyses. Hence, BAS are possibly the main source of the acidity in this sample as bridged hydroxyls (Boronat & Corma, 2019; Busca, 2017a). It is common knowledge that the acidity and hydrophilicity in zeolites are proportional (C. Liu et al., 2015), possibly the acid sites impact in the hydrophilicity maintenance. The high φ parameter for the sample (ii) is associated with little carbon deposition upon aging, as a consequence of no excess *Al* in the zeolite structure and no *EFA*l. Besides that, the partial amorphization of the sample (iv) produced a disorganization into the zeolite structure, then the adsorption capacity was also affected. The second proposed parameter (λ) (**Table 5.4.1**) assesses the effect caused by the carbon deposition in the material porosity, however the intensity to attract this carbon also must be taken in account. The porosity of samples (iii), (v) and (vii) were the least affected by the *C* deposition. This corroborates with the low impact on water adsorption reached by φ parameter. The sample (vi) had the highest effect in the internal volume caused by the carbon deposition, despite having the lowest carbon deposition upon aging, among LTA materials. The sample (ii) also have a high impact in the porosity volume that was clearly reflected in the hydrophilicity, parameter (φ). The results from material (iv) should be deeply analyzed in view that the amorphization of the material (**Figure 5.3.1(a)**), may cause modifications in the zeolite structure.

Table 5.4.1. The carbon deposition effect in the zeolitic materials characterized by (φ) and (λ) parameters

Sample		φ	λ
i	S-CHAc-SiAl2-K	*	*
ii	S-CHAc-SiAl2-Na	13.81	0.24
iii	S-CHAc-SiAl5-Na	0.77	0.01
iv	S-LTAc-SiAl1-K	19.51	0.13
v	S-LTAc-SiAl1-Na	0.77	0.04
vi	S-LTAc-SiAl2-Na	7.27	0.28
vii	S-LTAc-SiAl5-Na	0.97	0.03

* not applicable due to approximately no *C* deposition in the aged sample

The maximum water vapor adsorption at 10 and 70 mbar and 313 K for all samples, are summarized in the **Table 5.4.2**. Before starting compare the adsorbent materials, the possible presence of *EFAls* and acid sites should be taken in account, due to impacts on the carbon deposition, textural properties and adsorption capacity. Regarding CHA materials, the S-CHAc-SiAl2-Na was the pristine and aged materials that presented the higher hydrophilicity. However, upon aging, the CHA and *K*-form sample presented a low carbon deposition, hence a low decrease in the adsorption capacity upon aging. For LTA adsorbents, the pristine material that presents the highest adsorbed amount was S-LTAc-SiAl5-Na-V, however, upon aging, the textural properties and water vapor adsorption capacity had decreased in more than 35%. On the other hand, both *Na* samples with a low and intermediate *Si/Al* ratio have a low adsorption deactivation around 5%.

Table 5.4.2. Water Adsorption at 10 and 70 mbar and 313 K for the CHA and LTA Studied Materials

CHA			LTA		
Sample	Adsorption Capacity [mmol g^{-1}]		Sample	Adsorption Capacity [mmol g^{-1}]	
	10.0 mbar	70.0 mbar		10.0 mbar	70.0 mbar
			S-LTAc-SiAl1-Na-V	14.55	16.50
			S-LTAc-SiAl1-Na-E30d*	12.85	15.27*
S-CHAc-SiAl2-K-V	10.81	13.40	S-LTAc-SiAl1-K-V	11.23	13.75
S-CHAc-SiAl2-K-E30d*	10.18	12.31	S-LTAc-SiAl1-K-E30d*	0.23	1.76
S-CHAc-SiAl2-Na-V	12.28	20.74	S-LTAc-SiAl2-Na-V	14.47	17.00
S-CHAc-SiAl2-Na-E30d*	11.29	18.06	S-LTAc-SiAl2-Na-E30d*	13.92	15.93
S-CHAc-SiAl5-Na-V	11.48	14.84	S-LTAc-SiAl5-Na-V	12.40	18.27
S-CHAc-SiAl5-Na-E30d*	10.25	13.00	S-LTAc-SiAl5-Na-E30d*	6.88	11.93

SECTION 5.4 – PARTIAL CONCLUSIONS

The proposed aging protocol effectively caused a mild degradation in both zeolite structures under study (CHA and LTA). All zeolite materials present an affinity for CO_2 at 273 K and H_2O at 313 K with a more intense adsorbent/adsorbate affinity as the content of Aluminum increases and the framework becomes more polar. This is clearly demonstrated in the isotherms at low pressures. From experimental isotherms data, it was possible to infer a superior resistance of CHA materials in general upon aging. This CHA superior resistance to thermal aging is explained by a higher framework density, which enhances the material stability, and the smaller internal cages, suppressing coke formation and thus the material deactivation. LTA structure is thus more prone than CHA to accumulate *C,* whose concentration is on average twice as much in LTA upon aging for the same *Si/Al* ratio. Another factor that contributes to the carbon deposition into the zeolite surface is the local acidity brought about by extra-framework Aluminum, which is present in both CHA and LTA samples with a high *Si/Al* ratio (5). The samples containing potassium had different behaviors upon aging, although different *Si/Al* ratios were taken into account (1 for LTA, 2 for CHA). While this cation had a protective effect in the CHA sample (with *Si/Al* = 2), the K-LTA underwent amorphization, very likely due to the high density of *Al-O* bonds (less thermally stable than *Si-O*) and bulky potassium cations. In addition, the two parameters (φ and λ) showed a strong correlation between the maintenance of the micropore volume and the water adsorption capacity in all materials.

6 CONCLUSIONS

Two groups of zeolite materials (CHA and LTA) with different *Si/Al* ratios (1, 2 and 5) and compensating cations (*Na* and *K*) were successfully synthetized via hydrothermal routes, in some cases with the aid of an Organic Structure Direct Agent. Chemical and physical-chemical techniques were able to measure different textural and compositional (superficial and bulk) properties in such materials. Both Premature Aging Protocols (PAP- 1 and 2) led to a mild degradation in textural and water adsorption properties in the two groups of adsorbents, which allowed for a deeper investigation about the hydrothermal stability of cationic zeolites in drying TSA processes. The presence of hydrocarbons (n-heptane) associated with high temperatures showed to have a key-role in the material deactivation. The PAP-2 in comparison to the PAP-1, is more convenient for smaller lab-scale synthesized samples and it provides homogeneous pre-adsorption of n-heptane and water vapors. An aging time (PAP-2) of 30 days was chosen as effective to cause sensible textural modifications in the materials.

The samples containing potassium had different behaviors upon aging, although different *Si/Al* ratios were taken into account (1 for LTA, 2 for CHA). Potassium in CHA (*Si/Al* = 2) enhanced the thermal stability, shown by an unchanging XRD pattern of aged sample, unlike the sample with *Na*. In addition, this compensation cation in the CHA structure developed a sieving effect, hindering the *C* deposition in the framework cavities, which is one of the main reasons for the adsorbent deactivation. CHN elemental analysis revealed that S-CHAc-SiAl2-K sample retained the least *C* bulk content among all LTA and CHA analyzed materials. On the other hand, the *K* content in LTA (*Si/Al* = 1) led to the structure amorphization, caused by the rupture of *T* – *O* – *T* bonds containing Al, and hence the detachment of sodalite cages. FT-IR analysis revealed that the signal corresponding to the D4R primary building unit decreases in intensity from pristine to aged materials.

All pristine and aged zeolite samples show tetrahedral coordination of *Al* (typical of aluminosilicates) by XPS analysis. On both samples with the highest *Si/Al*

ratio (=5), however, besides tetrahedral *Al*, *EFAl* were identified by NMR. The presence of *EFAl* had a key role in *C* deposition upon aging because samples with such a high *Si/Al* were expected to be much more robust to aging than those with a higher content of framework *Al* and they actually aged more. It may be postulated that the *C* deposition occurs into the inner and outer surfaces, as identified in XPS and CHN Elemental Analysis. In addition, the *Al* migration from the external to the internal bulk of the adsorbent material was observed in all aged solids. Also, from XPS experiments, the *Si/Al* ratio in the external surface increases after the aging protocol, while the *Si/Al* ratio identified by NMR and XRF experiments remains approximately the same. The aging duration is proportional to the extent of *Al* migration.

The increasing polarity in cationic zeolites caused by a higher density of framework *Al* is a double-edged sword. While it enhances the hydrophilicity and hence the water uptake, it also leads to higher carbon deposition upon aging. Zeolite materials with unbalanced charges (excess framework *Al* as compared to cations) may give rise to Bronsted Acid Sites (BAS) that are composed by bridged hydroxyls, the strongest acid site in zeolites. In this way, these acid sites may trigger polymerization reactions of adsorbed hydrocarbons (e.g. n-heptane) leading to coke deposition that may block the pores, thus decreasing the accessibility to the micropore volume. In most of the analyzed materials in this thesis, BAS acidity was not clearly characterized, although the LTA sample with *Si/Al* 2 showed excess framework *Al* and no *EFAl*. Actually, the sample S-LTAc-SiAl2-Na was the one with the best tradeoff between water uptake and hydrothermal stability, with a low carbon deposition upon aging. Further studies in this sample need to be performed, in order to observe the continuous *C* accumulation and the effect produced in the hydrothermal stability in the long term. It is also yet to be investigated if potassium in this sample would be as deleterious as in the LTA sample with *Si/Al* = 1 or it would provide the protective effect observed for CHA (at the same *Si/Al* ratio).

Generally speaking, experimental evidence has shown a better stability for CHA over LTA samples upon aging. The superior thermal resistance may be explained by a higher framework density of the CHA structure associated with smaller cavities

that prevent the formation of larger compounds from hydrocarbons previously adsorbed. This seems to be the main effect to explain the robustness of the potassium CHA (*Si/Al* = 2). The ideal features of a drying adsorbent in long-term TSA operation should take in account not only the water vapor adsorption capacity, but also hydrothermal robustness and the ability to prevent the *C* deposition in the framework.

7. SUPPLEMENTARY MATERIAL

7.1. CHA – XPS SPECTROGRAMS

Figure 7.1.1. XPS spectrograms for all contributions in the chabazite samples S-CHA$_C$-SiAl2-Na-V

Contribution (eV)	Spectrogram
Si2p (102.6)	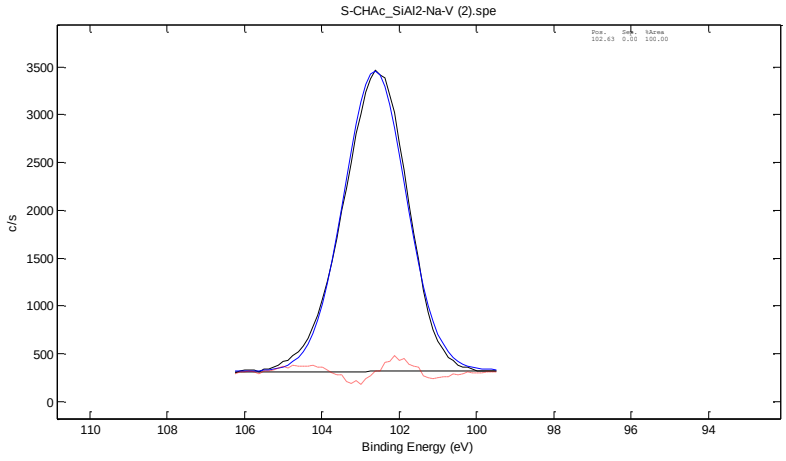
Al2p (74.6)	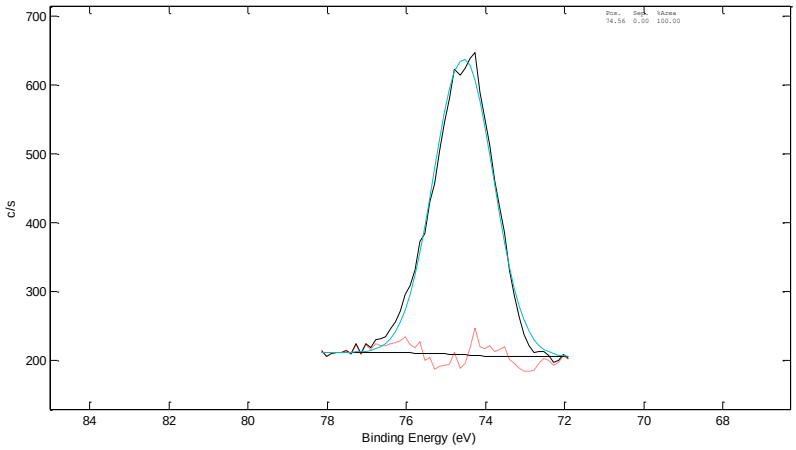
C1s (285.0; 286.6) K2p3/2 (294.6)	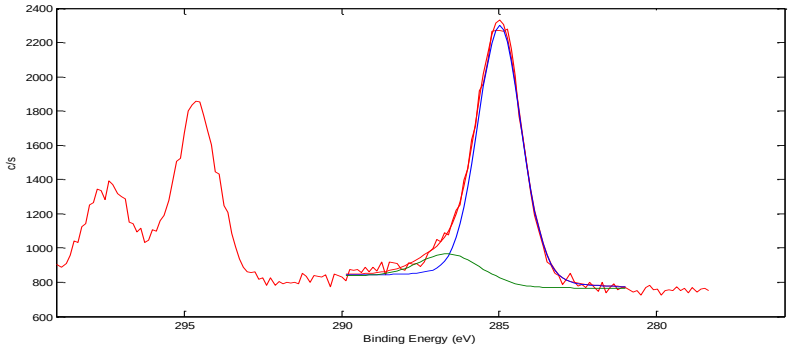

O1s (531.8)

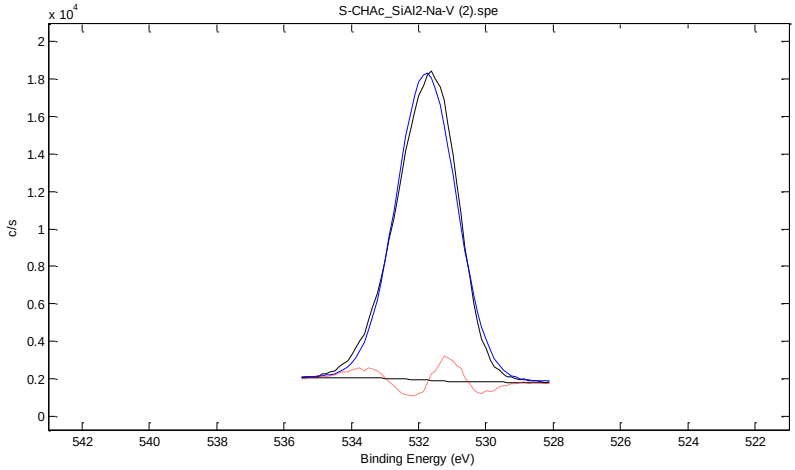

Na1s (1072.7)

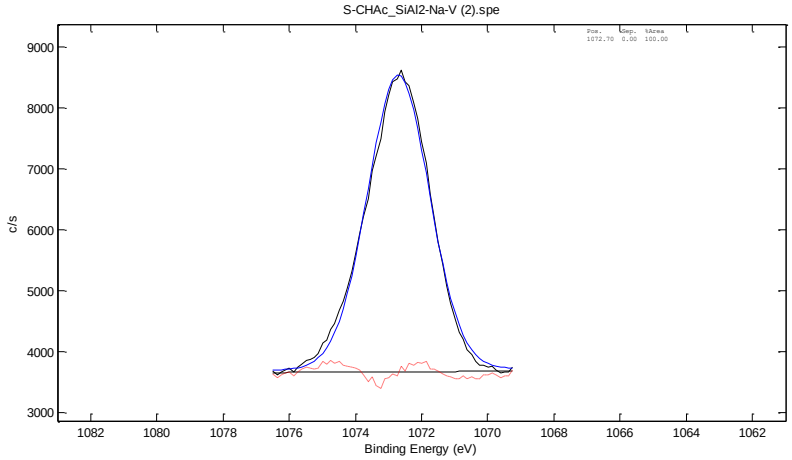

Figure 7.1.2. XPS spectrograms for all contributions in the chabazite samples S-CHA$_C$-SiAl2-Na-E30d*

Contribution (eV)	Spectrogram
Si2p (102.5)	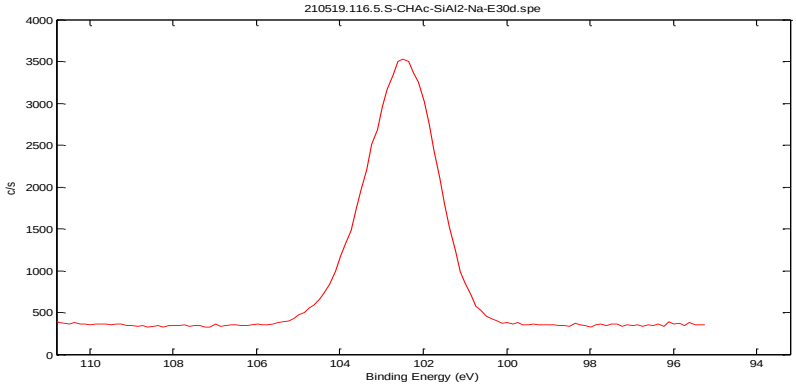

Al2p (74.1)

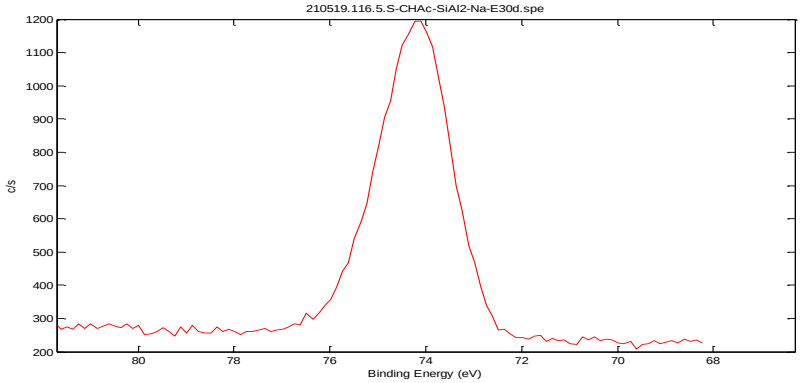

C1s (284.7; 285.9) K2p3/2 (294.5)

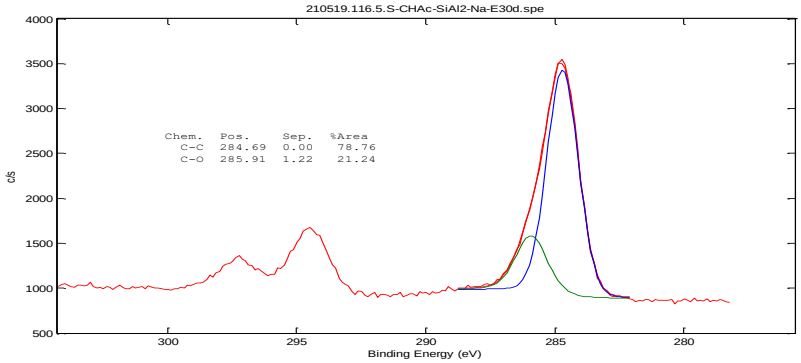

O1s (531.6)

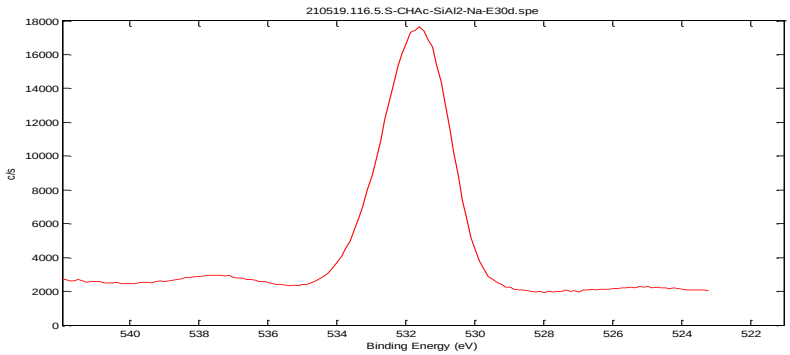

Na1s (1072.3)

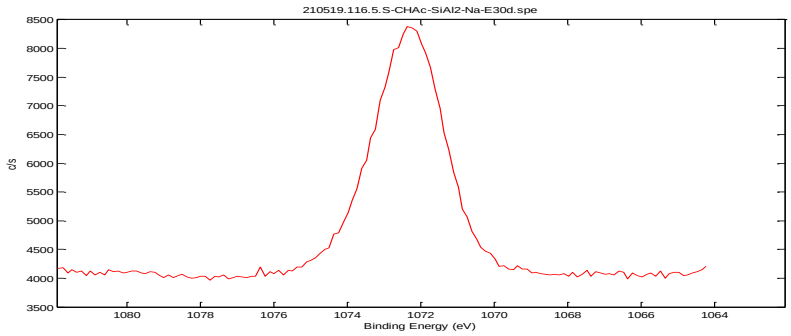

Figure 7.1.3. XPS spectrograms for all contributions in the chabazite samples S-CHA$_C$-SiAl5-Na-V

Contribution (eV)	Spectrogram
Si2p (103.1)	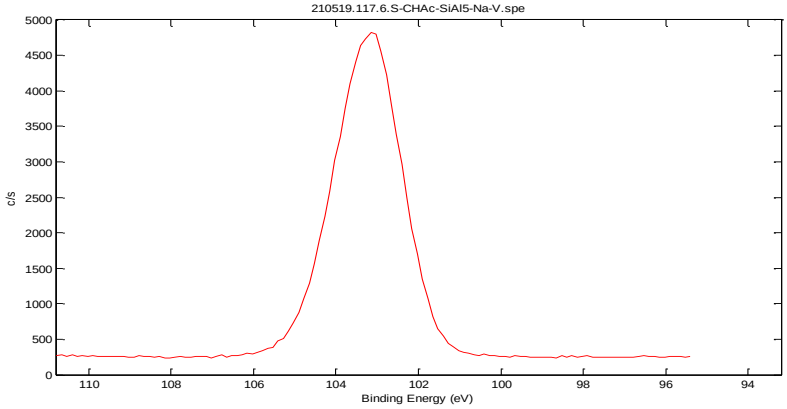
Al2p (74.3)	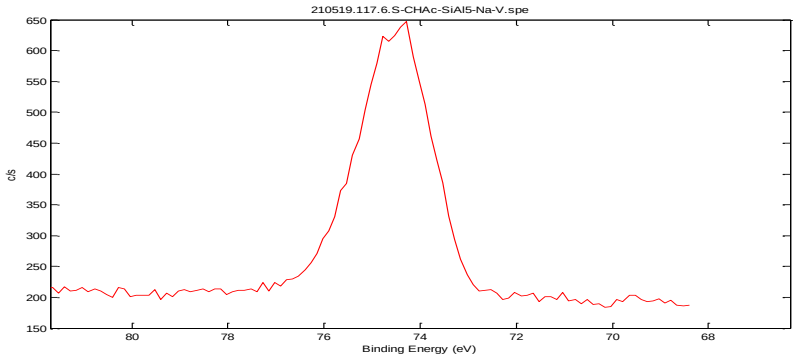
C1s (284.8; 286.3)	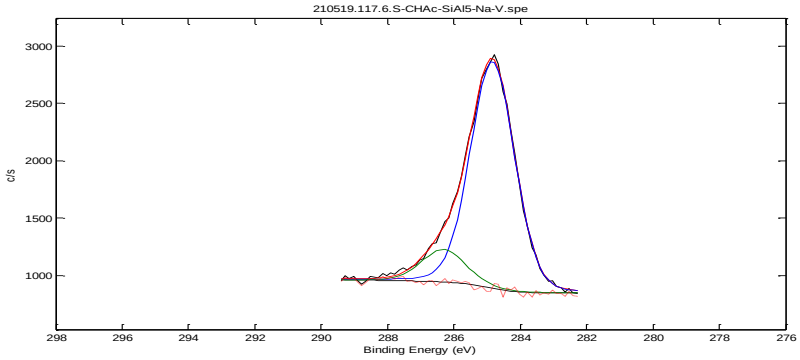
O1s (532.5)	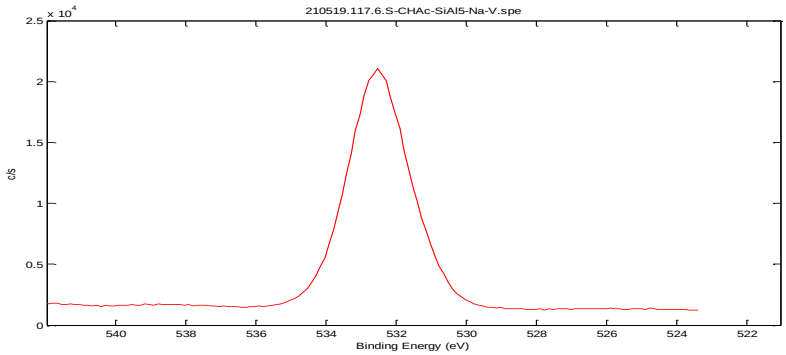

Na1s (1072.8)

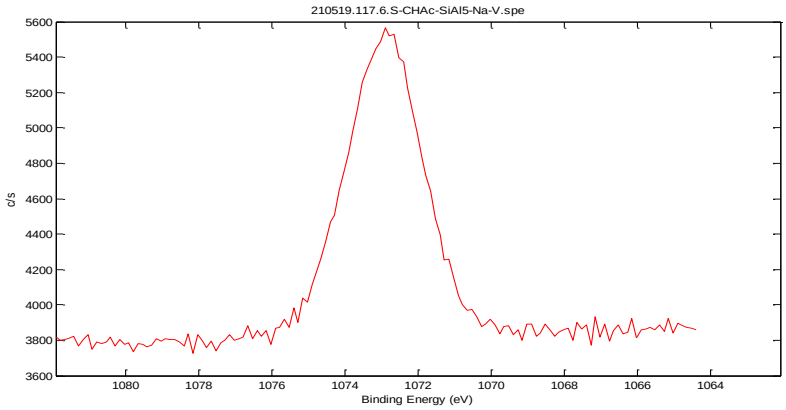

Figure 7.1.4. XPS spectrograms for all contributions in the chabazite samples S-CHA$_C$-SiAl5-Na-E30d*

Contribution (eV)	Spectrogram
Si2p (103.3)	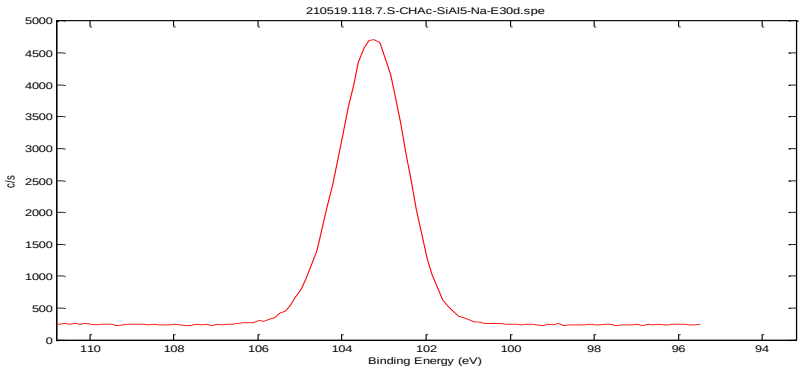
Al2p (74.5)	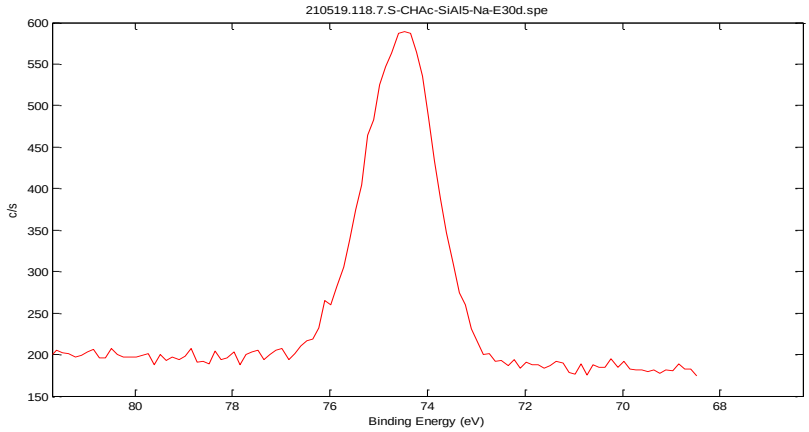
C1s (284.8; 286.3)	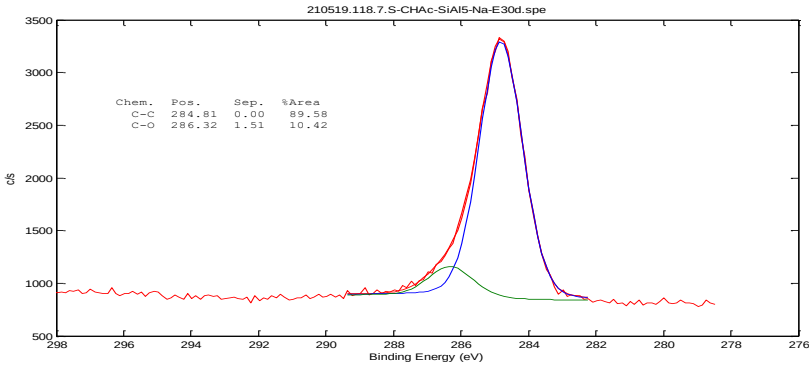

O1s (532.6)

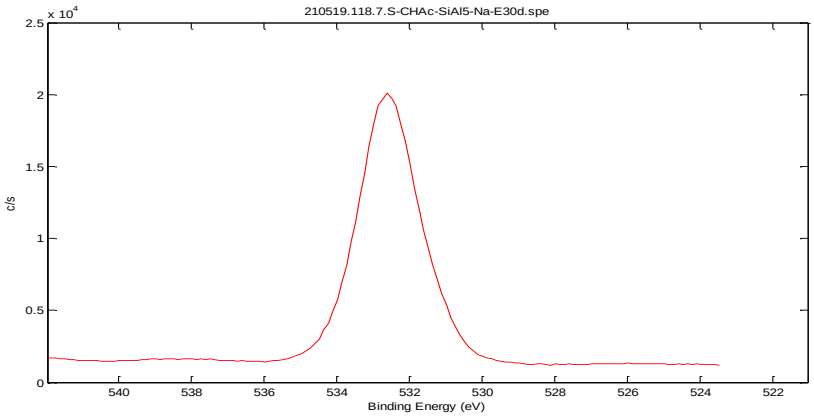

Na1s (1073.0)

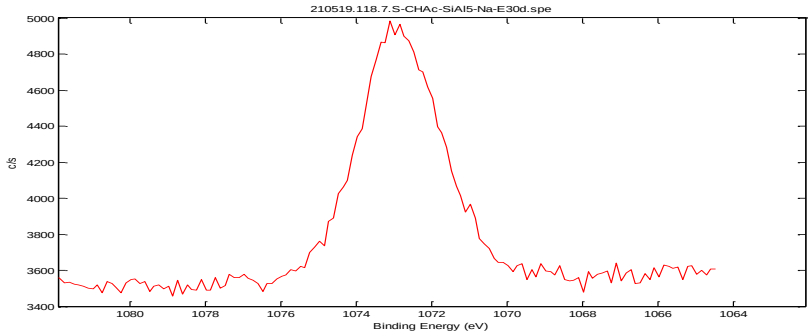

Figure 7.1.5. XPS spectrograms for all contributions in the chabazite samples S-CHA$_C$-SiAl2-K-V

Contribution (eV)	Spectrogram
Si2p (102.4)	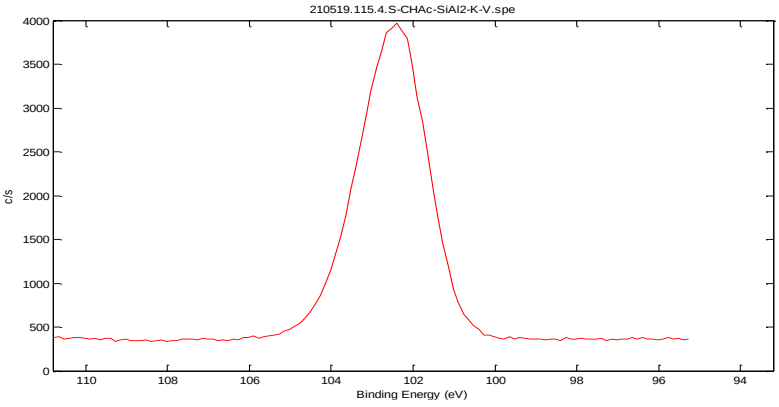
Al2p (74.2)	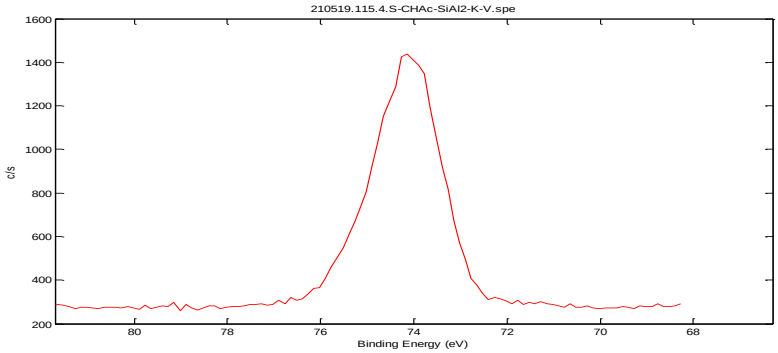

C1s (284.9; 286.3) K2p3/2 (294.3)

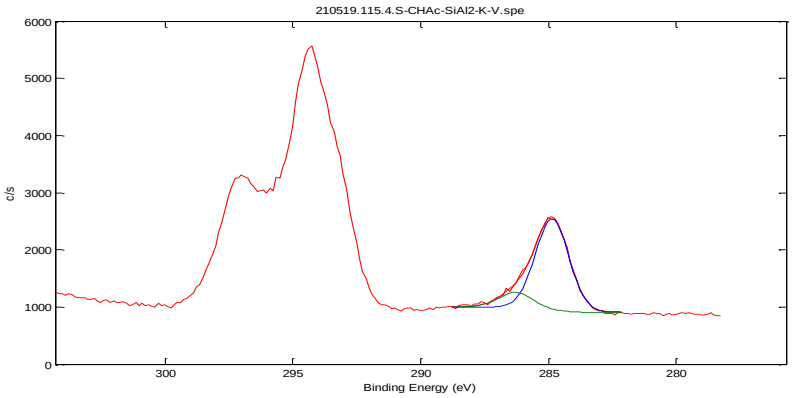

O1s (531.5)

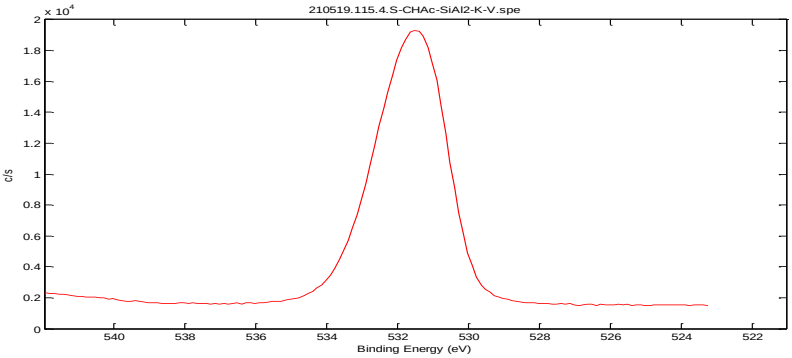

Figure 7.1.6. XPS spectrograms for all contributions in the chabazite samples S-CHA$_C$-SiAl2-K-E30d*

Contribution (eV)	Spectrogram
Si2p (102.5)	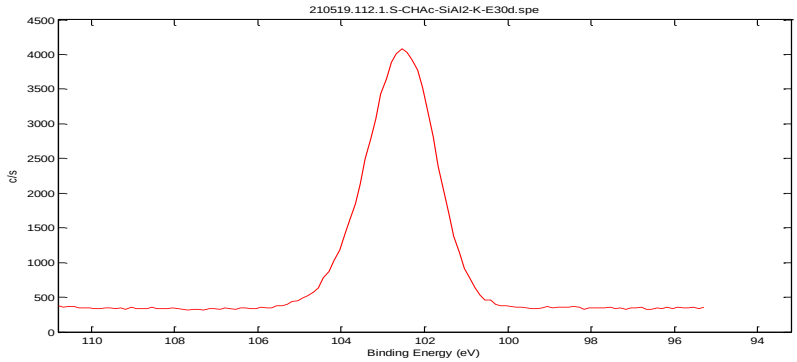
Al2p (74.1)	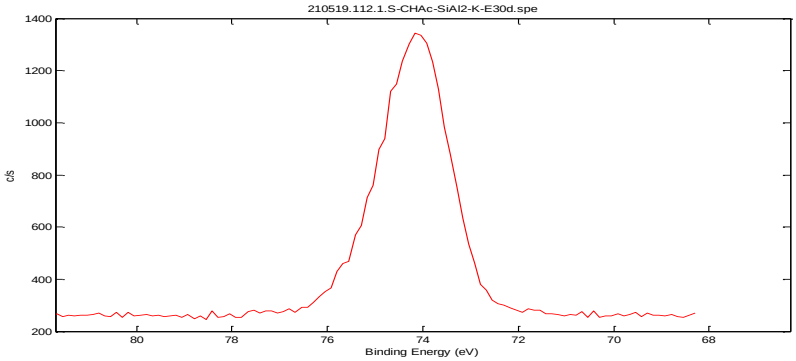

C1s (284.7; 286.0) K2p3/2 (294.3)

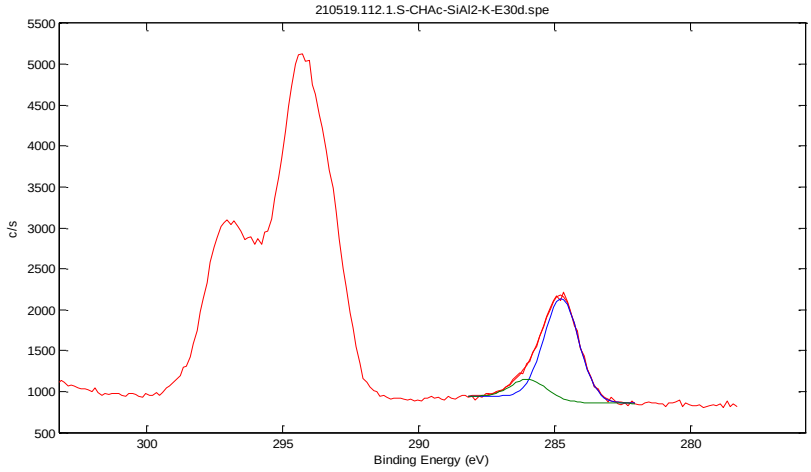

O1s (531.6)

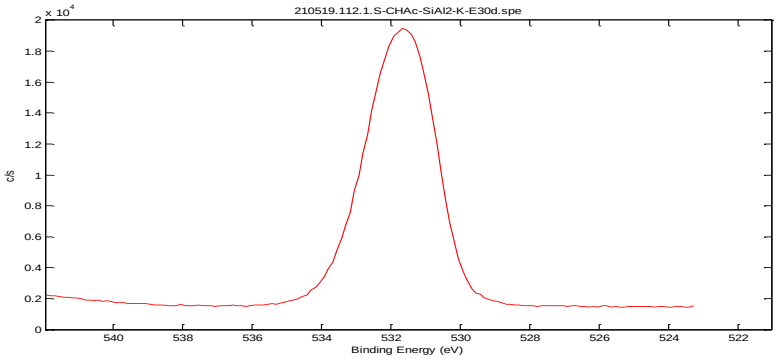

7.2. LTA – XPS SPECTROGRAMS

Figure 7.2.1. XPS spectrograms for all contributions in the chabazite samples S-LTA$_C$-SiAl1-Na-V

Contribution (eV)	Spectrogram
Si2p (101.6)	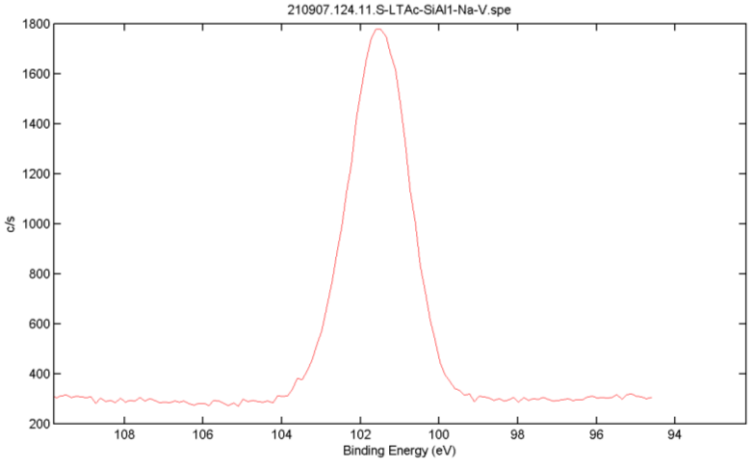

Al2p (73.7)

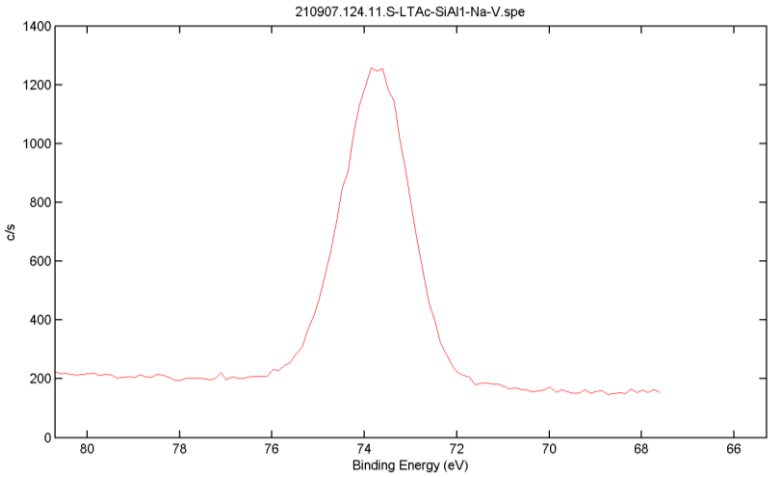

C1s (284.9; 286.2; 288.7)

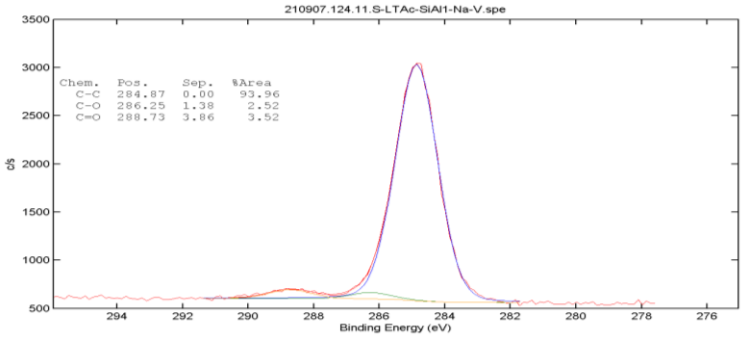

O1s (530.8; 532.3)

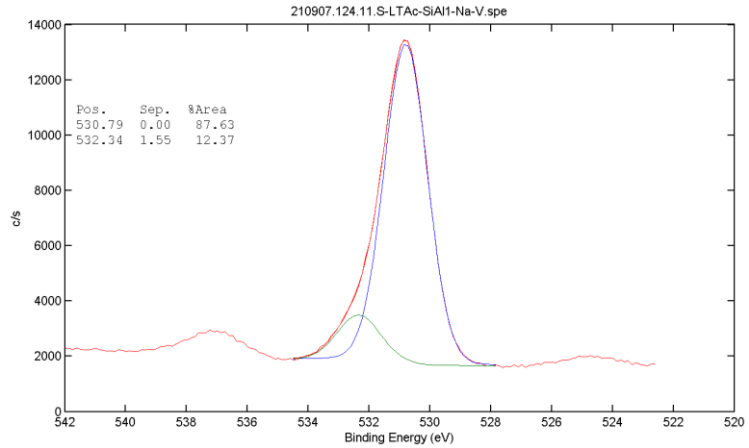

Na1s (1072.0)

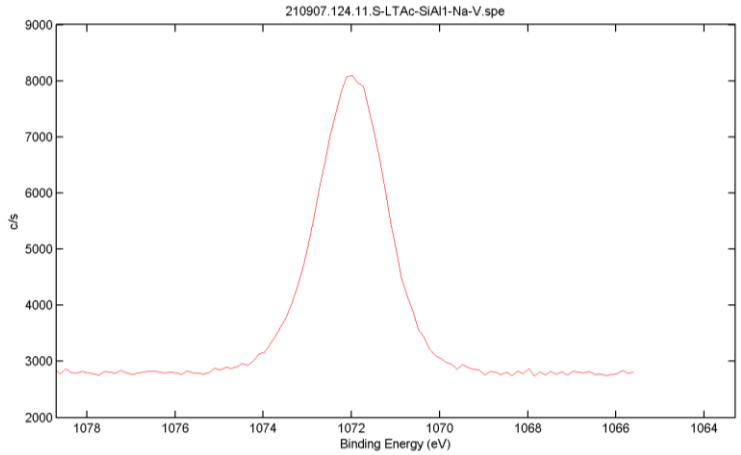

Figure 7.2.2. XPS spectrograms for all contributions in the chabazite samples S-LTA$_C$-SiAl1-Na-E30d*

Contribution (eV)	Spectrogram
Si2p (101.9)	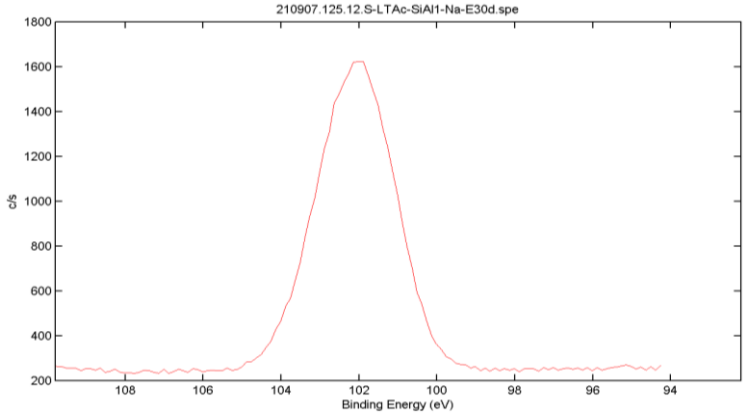
Al2p (74.0)	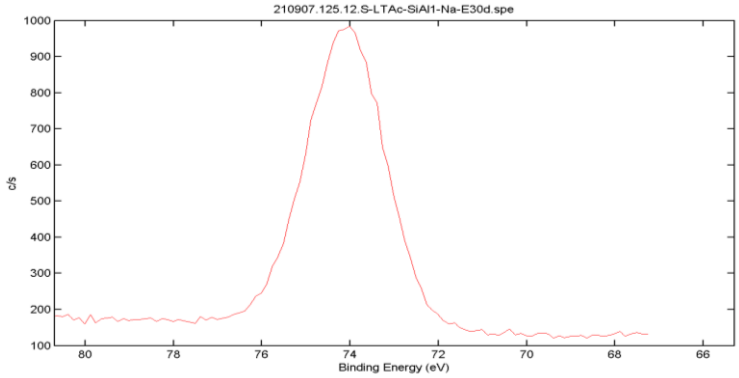
C1s (284.8; 286.0)	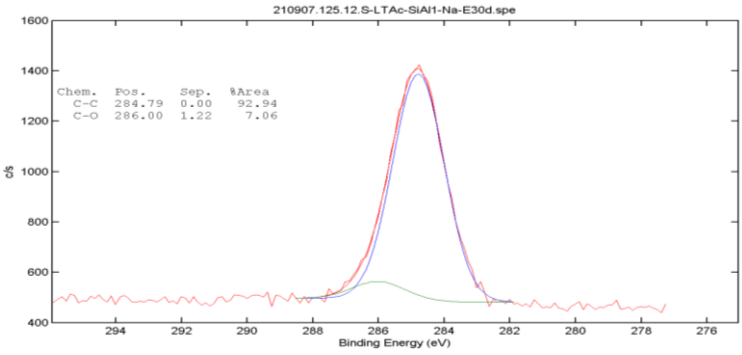
O1s (531.2)	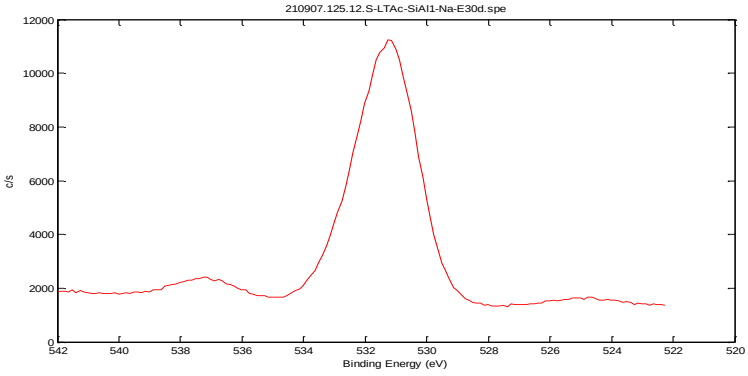

Na1s (1072.3)

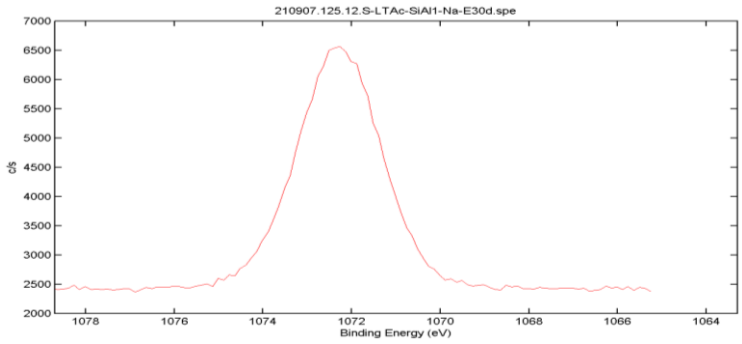

Figure 7.2.3. XPS spectrograms for all contributions in the chabazite samples S-LTA$_C$-SiAl1-K-V

Contribution (eV)	Spectrogram
Si2p (101.5)	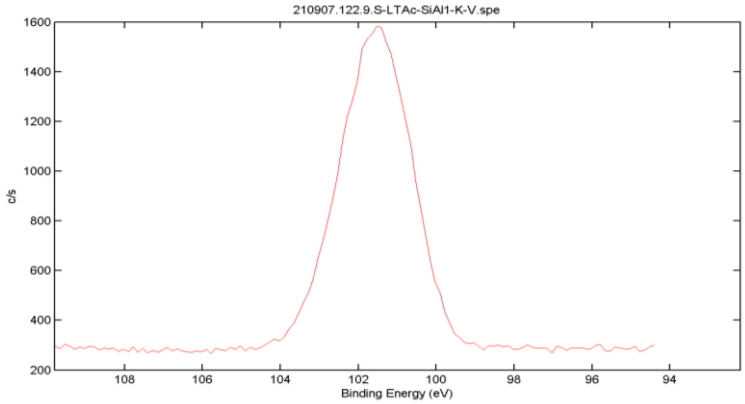
Al2p (73.7)	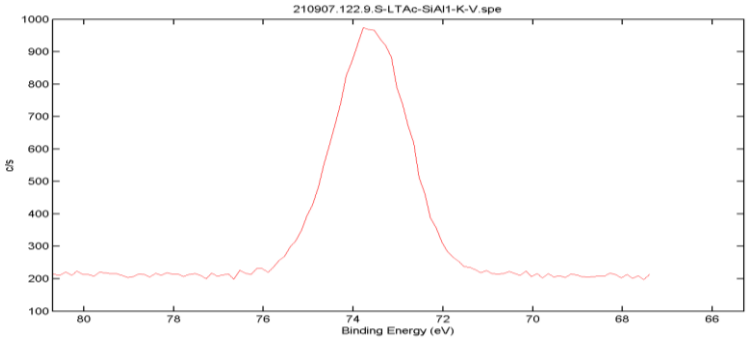
C1s (284.8) K2p3/2 (293.2)	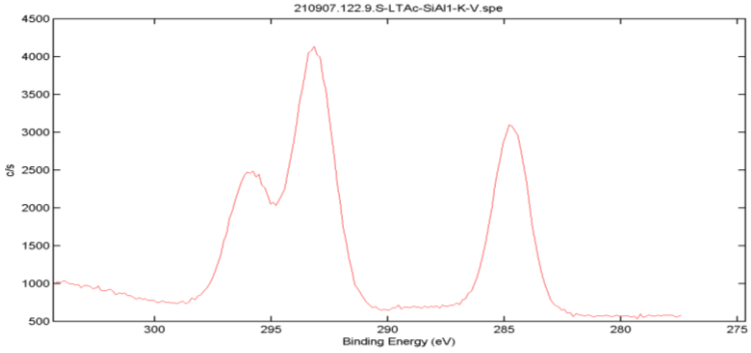

O1s (530.6)

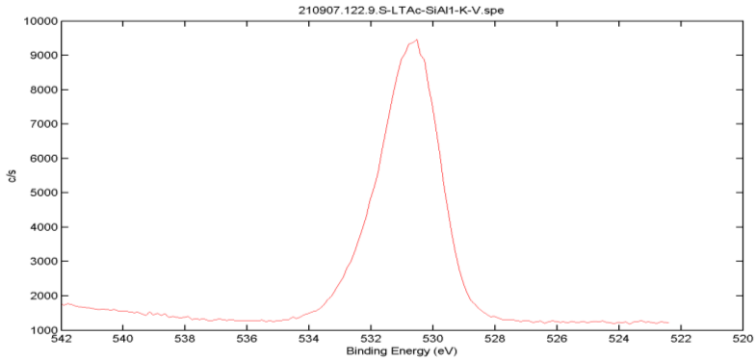

Figure 7.2.4. XPS spectrograms for all contributions in the chabazite samples S-LTA$_C$-SiAl1-K-E30d*

Contribution (eV)	Spectrogram
Si2p (102.0)	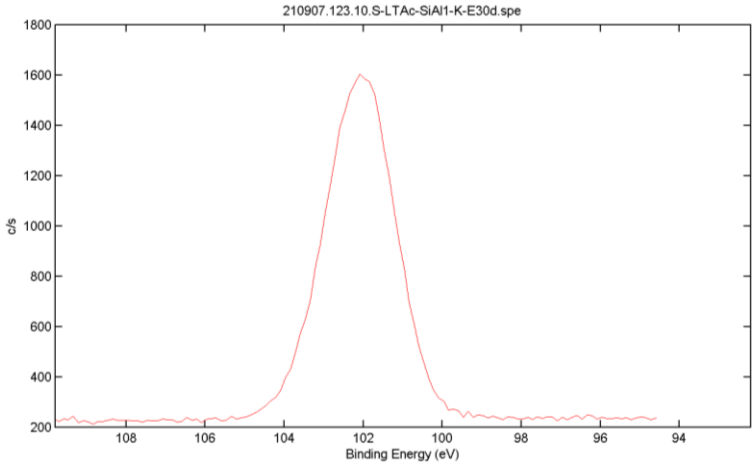
Al2p (74.1)	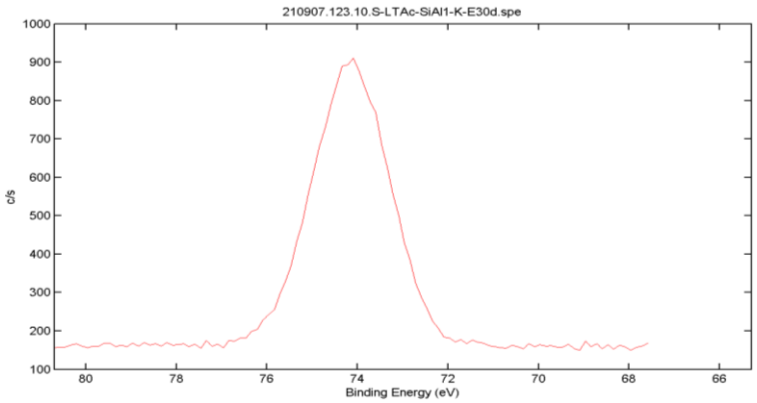
C1s (284.8) K2p3/2 (293.2)	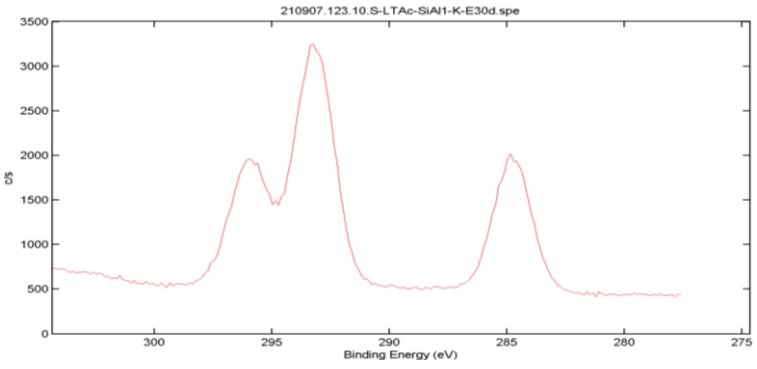

O1s (531.2)

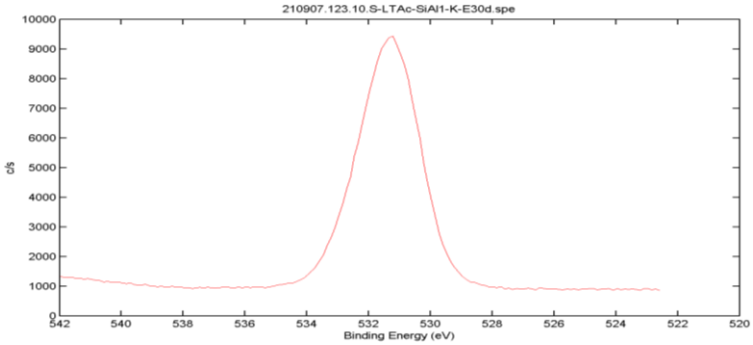

Figure 7.2.5. XPS spectrograms for all contributions in the chabazite samples S-LTA$_C$-SiAl2-Na-V

Contribution (eV)	Spectrogram
Si2p (102.7)	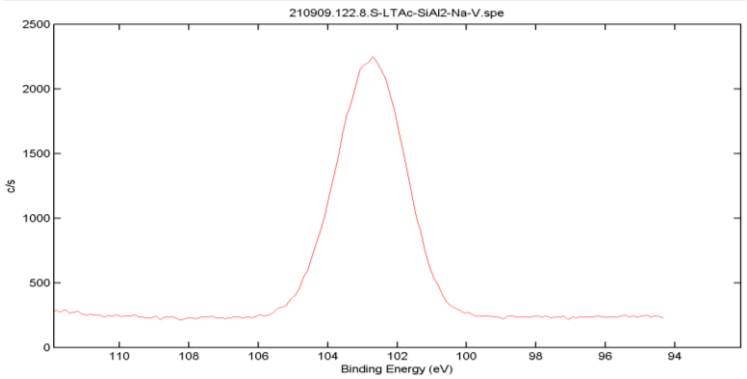
Al2p (74.6)	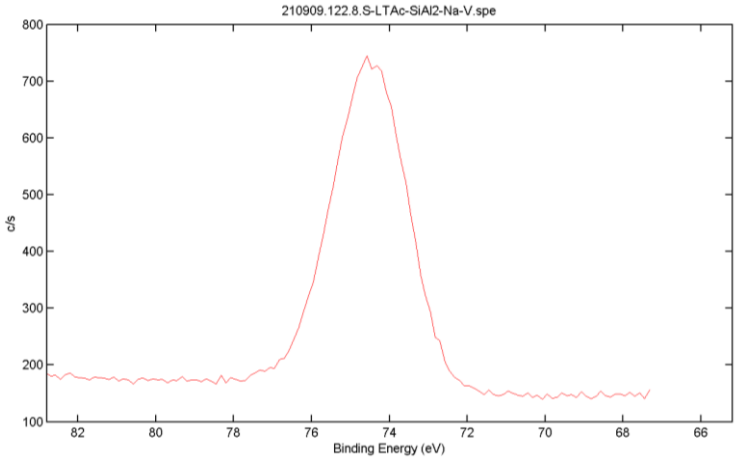
C1s (284.8; 286.5; 289.2)	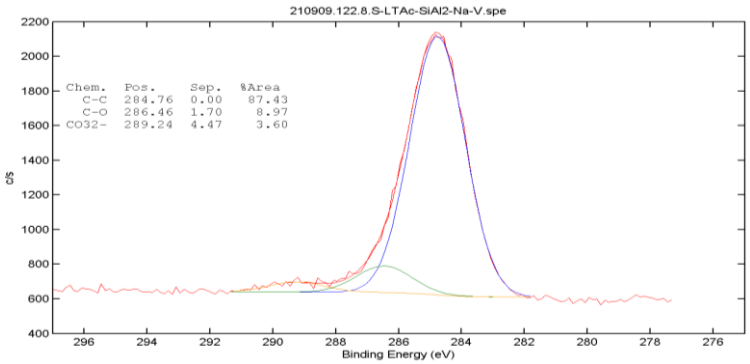

O1s (531.9)

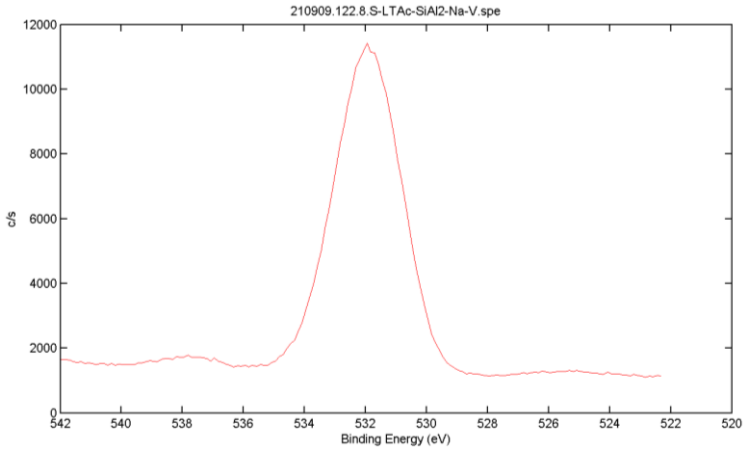

Na1s (1072.5)

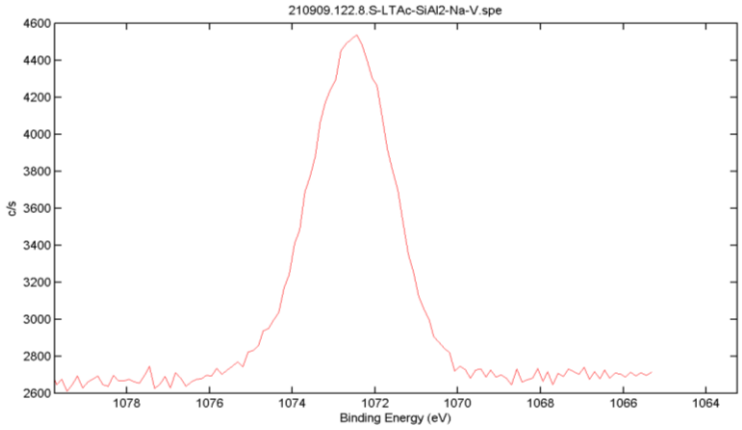

Figure 7.2.6. XPS spectrograms for all contributions in the chabazite samples S-LTA$_C$-SiAl2-Na-E30d*

Contribution (eV)	Spectrogram
Si2p (102.7)	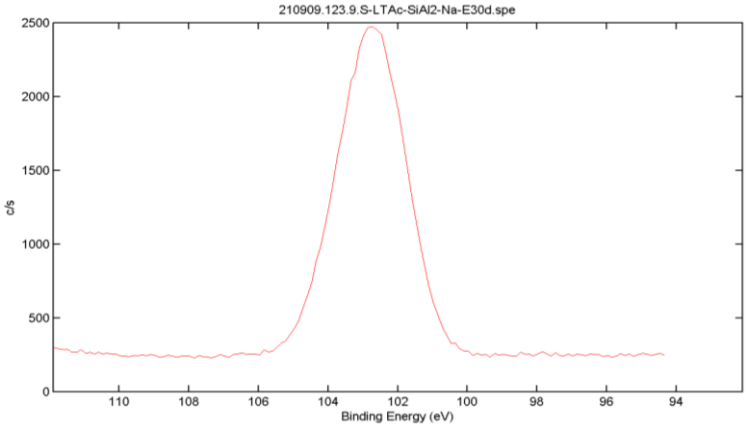

Al2p (74.6)

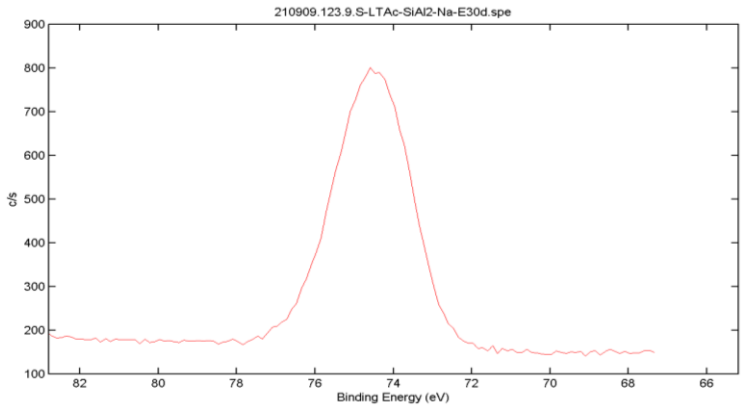

C1s (284.6; 286.0)

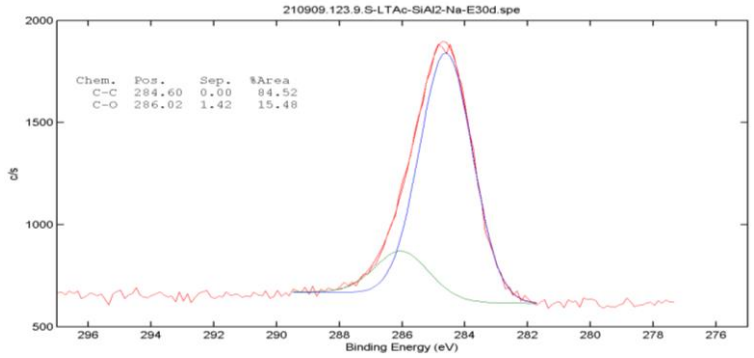

O1s (531.9)

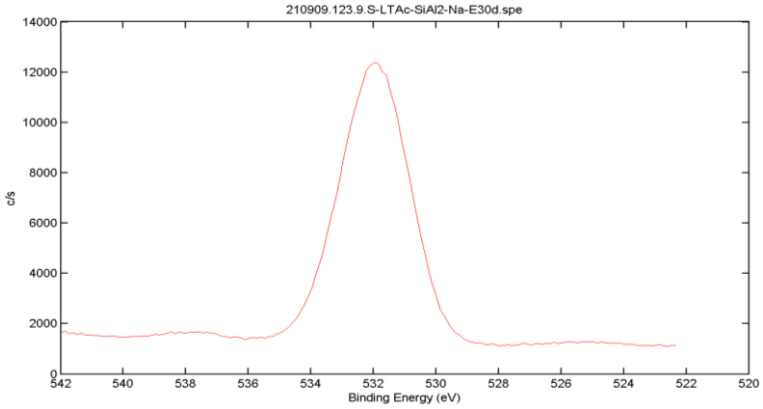

Na1s (1072.5)

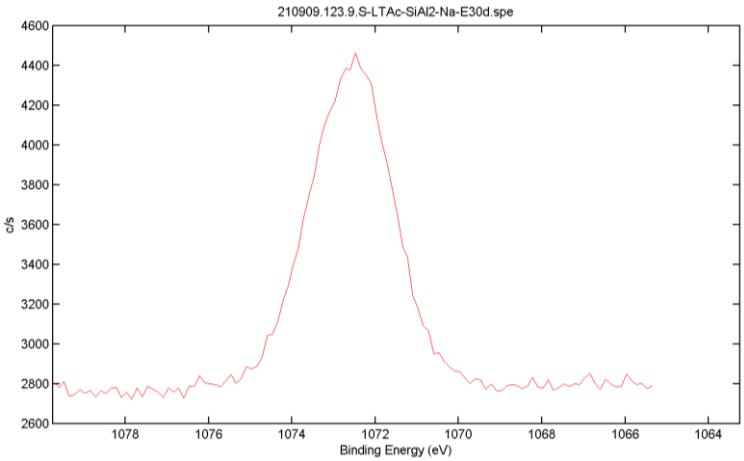

Figure 7.2.7. XPS spectrograms for all contributions in the chabazite samples S-LTA$_C$-SiAl5-Na-V

Contribution (eV)	Spectrogram
Si2p (103.1)	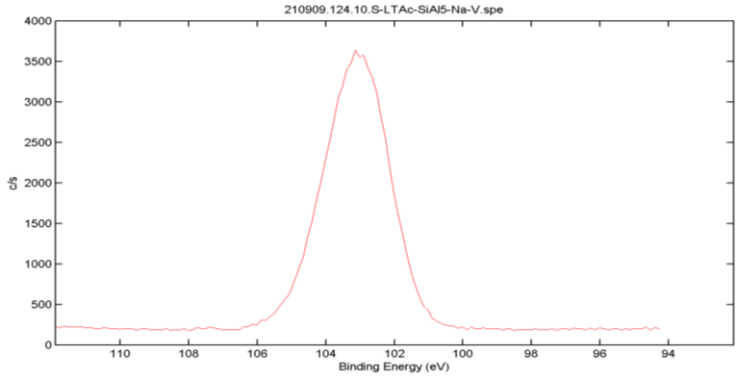
Al2p (74.6)	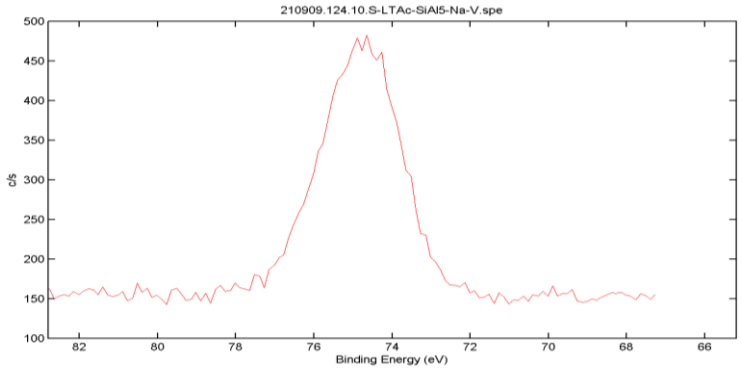
C1s (284.6; 286.2; 288.8)	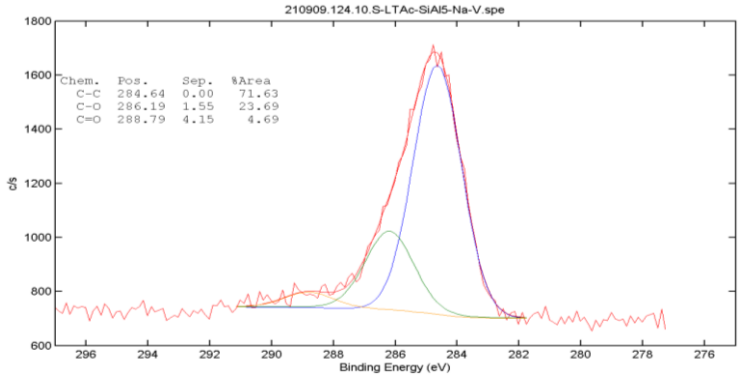
O1s (532.4)	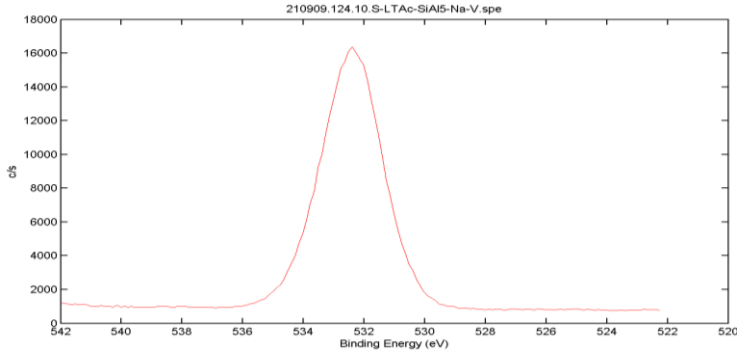

Na1s (1072.6)

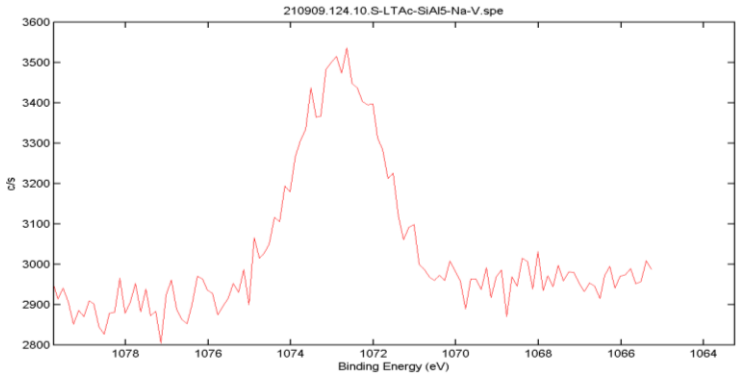

Figure 7.2.8. XPS spectrograms for all contributions in the chabazite samples S-LTA$_C$-SiAl5-Na-E30d*

Contribution (eV)	Spectrogram
Si2p (103.5)	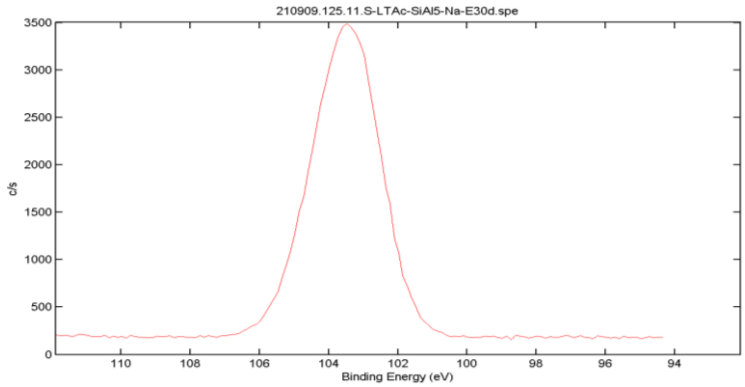
Al2p (75.1)	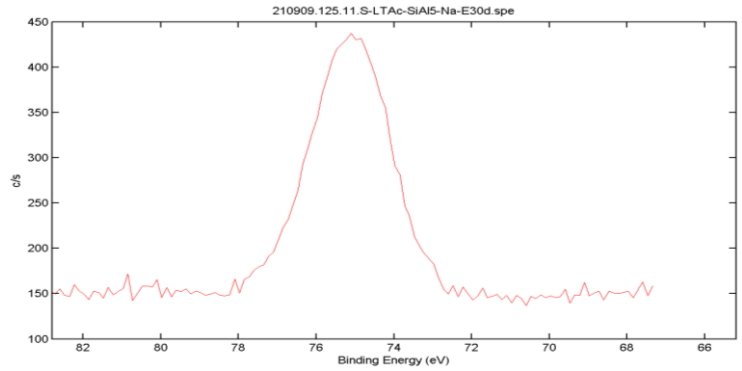
C1s (284.9; 286.8)	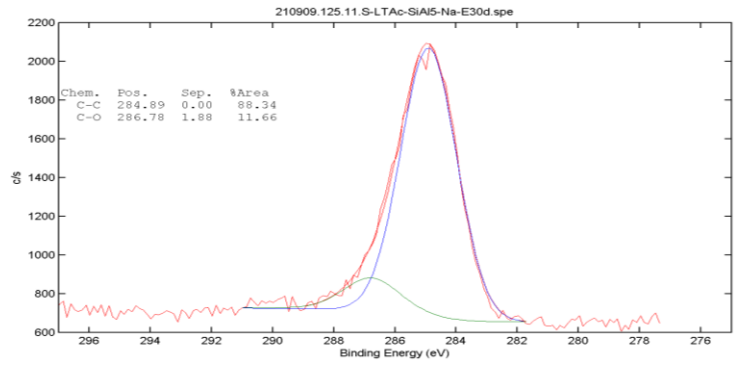

O1s (532.8)

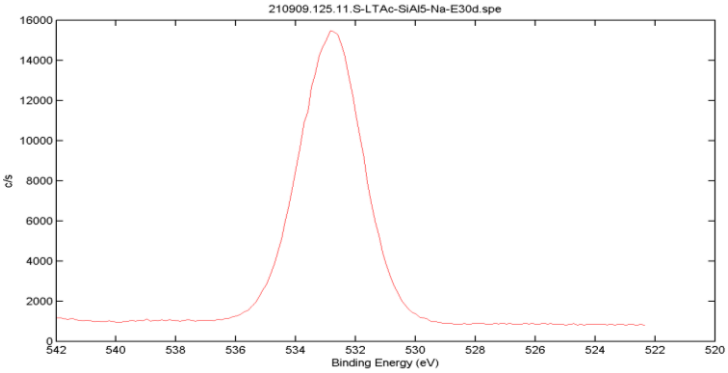

Na1s (1072.9)

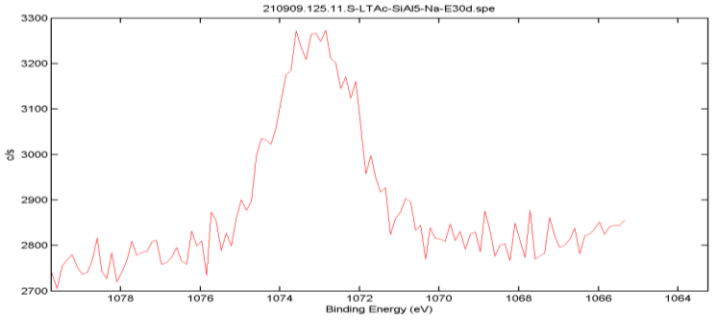

7.3. CHA – *^{27}Al* and *^{29}Si* NMR Spectrum

Figure 7.3.1. *^{27}Al* and *^{29}Si* NMR spectrum for S-CHA$_C$-SiAl2-Na

S-CHAc-SiAl2-Na-V

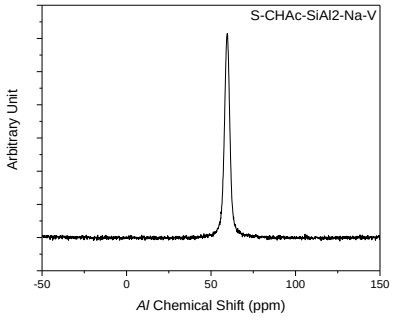

^{27}Al NMR Spectra

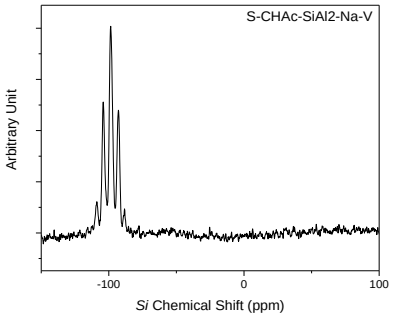

^{29}Si NMR Spectra

S-CHAc-SiAl2-Na-E30d*

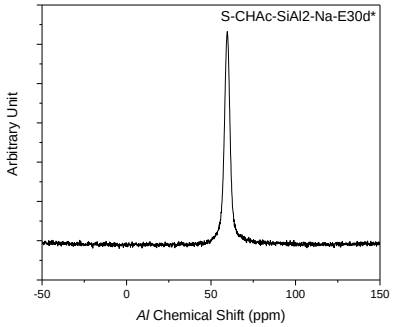

^{27}Al NMR Spectra

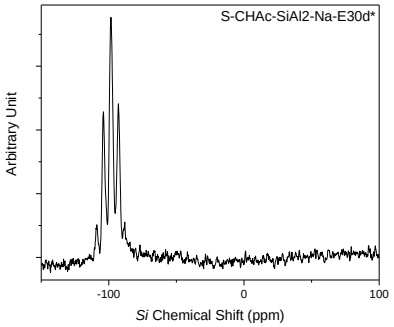

^{29}Si NMR Spectra

S-CHAc-SiAl2-Na-E35c

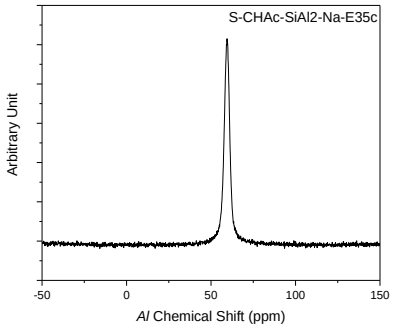

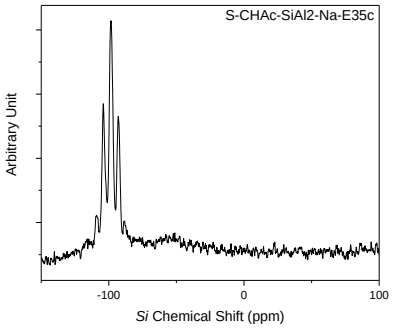

^{27}Al NMR Spectra ^{29}Si NMR Spectra

S-CHAc-SiAl2-Na-E60d

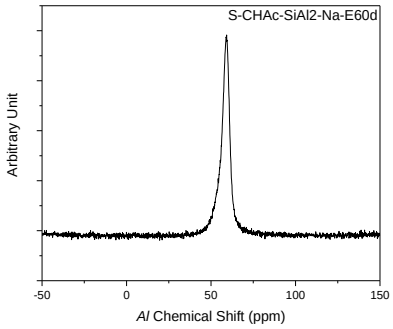

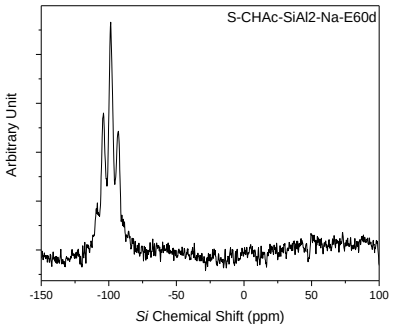

^{27}Al NMR Spectra ^{29}Si NMR Spectra

Figure 7.3.2. ^{27}Al and ^{29}Si NMR spectrum for S-CHA$_C$-SiAl5-Na

S-CHAc-SiAl5-Na-V

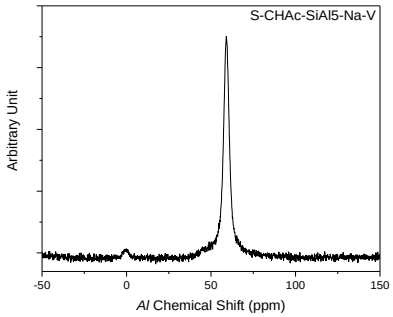

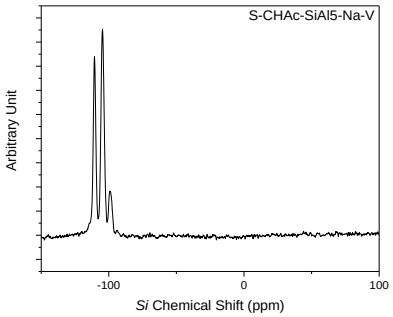

^{27}Al NMR Spectra ^{29}Si NMR Spectra

S-CHAc-SiAl5-Na-E30d*

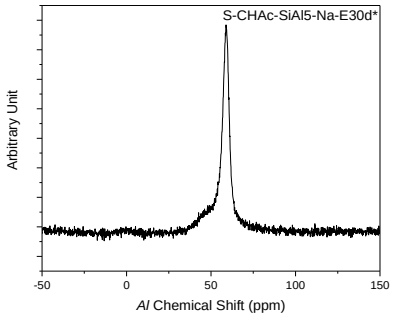

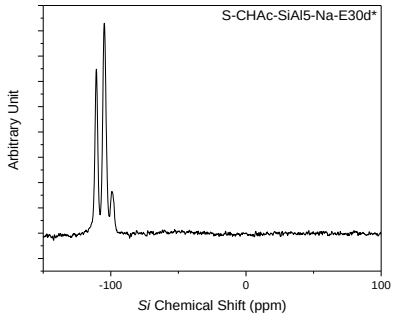

^{27}Al NMR Spectra ^{29}Si NMR Spectra

Figure 7.3.3. ^{27}Al and ^{29}Si NMR spectrum for S-CHA$_C$-SiAl2-K

S-CHAc-SiAl2-K-V

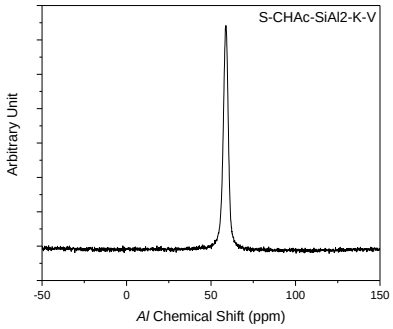

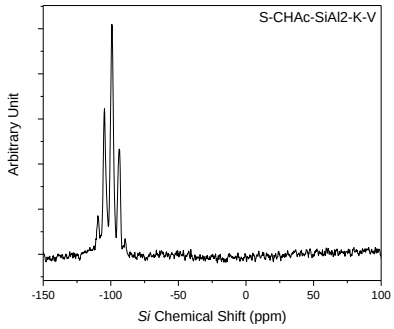

^{27}Al NMR Spectra ^{29}Si NMR Spectra

S-CHAc-SiAl2-K-E30d*

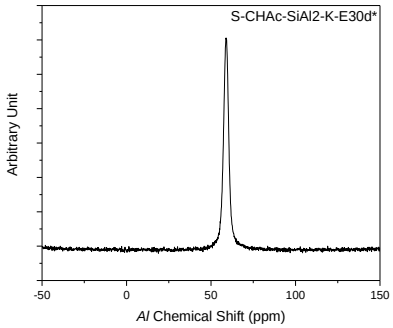

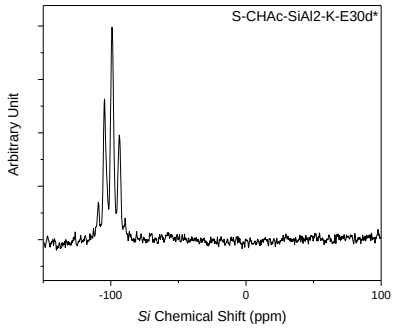

^{27}Al NMR Spectra ^{29}Si NMR Spectra

7.4. LTA – *27Al* and *29Si* NMR Spectras

Figure 7.4.1. *27Al* and *29Si* NMR spectrum for S-LTA$_C$-SiAl1-K

S-LTAc-SiAl1-K-V

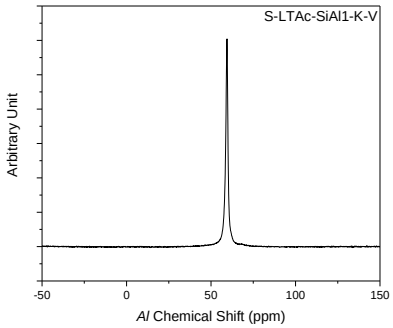

27Al NMR Spectra

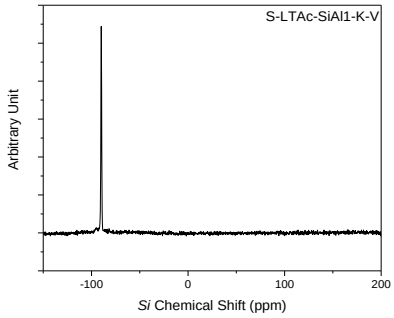

29Si NMR Spectra

S-LTAc-SiAl1-K-E30d*

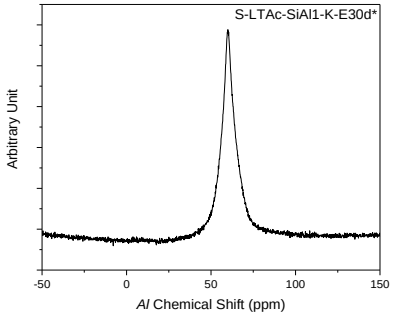

27Al NMR Spectra

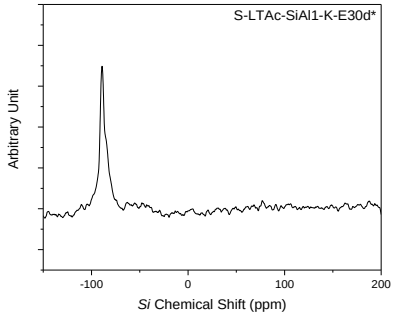

29Si NMR Spectra

Figure 7.4.2. *27Al* and *29Si* NMR spectrum for S-LTA$_C$-SiAl1-Na

S-LTAc-SiAl1-Na-V

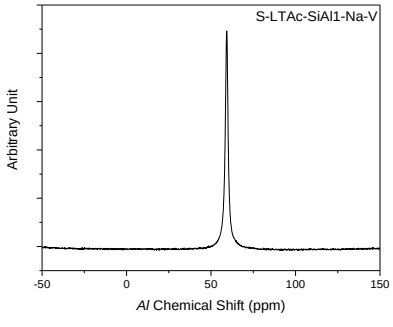

27Al NMR Spectra

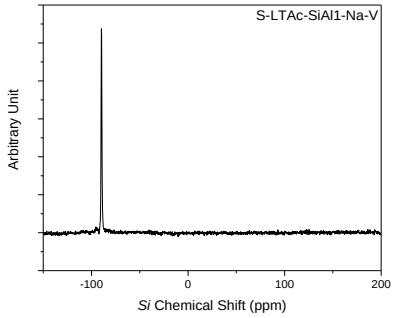

29Si NMR Spectra

S-LTAc-SiAl1-Na-E30d*

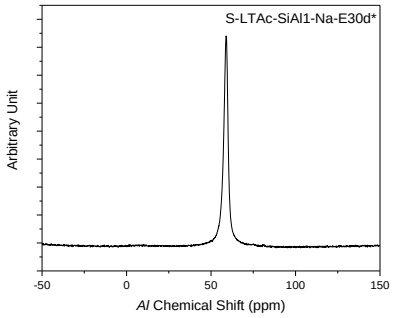

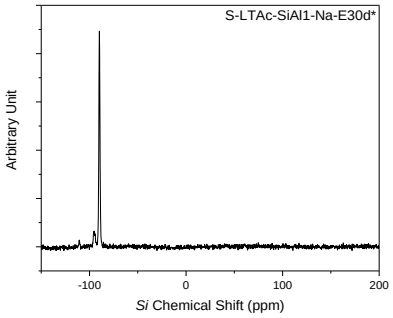

^{27}Al NMR Spectra ^{29}Si NMR Spectra

Figure 7.4.3. ^{27}Al and ^{29}Si NMR spectrum for S-LTA$_C$-SiAl2-Na

S-LTAc-SiAl2-Na-V

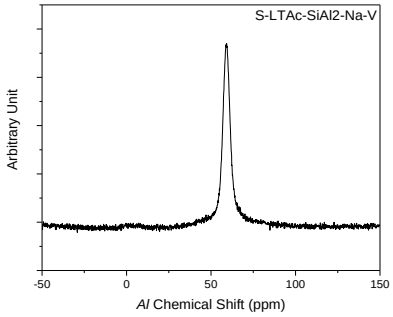

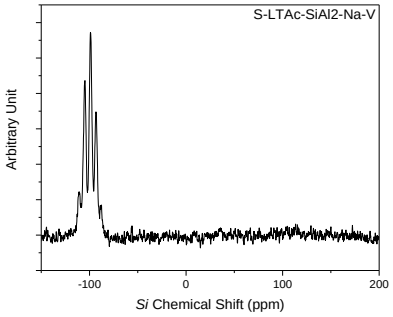

^{27}Al NMR Spectra ^{29}Si NMR Spectra

S-LTAc-SiAl2-Na-E30d*

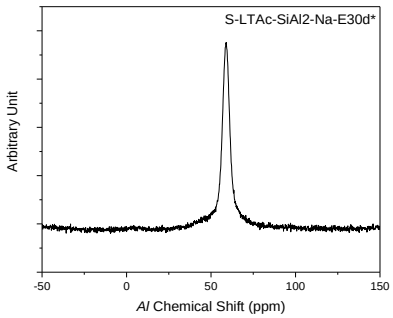

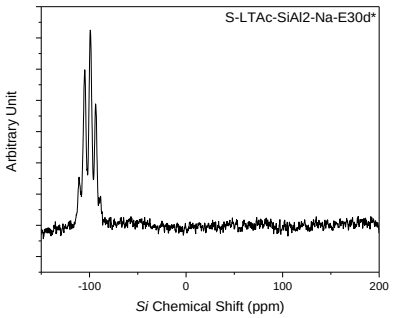

^{27}Al NMR Spectra ^{29}Si NMR Spectra

Figure 7.4.4. *[27]Al* and *[29]Si* NMR spectrum for S-LTA$_C$-SiAl5-Na

S-LTAc-SiAl5-Na-V

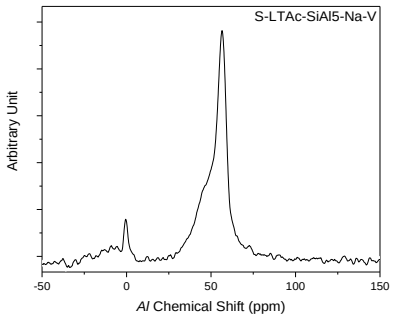

[27]Al NMR Spectra

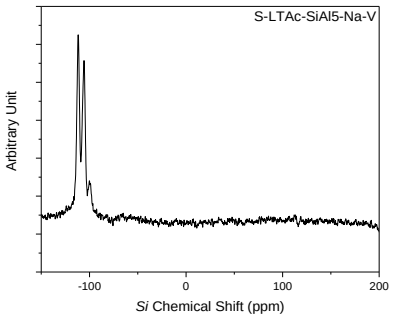

[29]Si NMR Spectra

S-LTAc-SiAl5-Na-E30d*

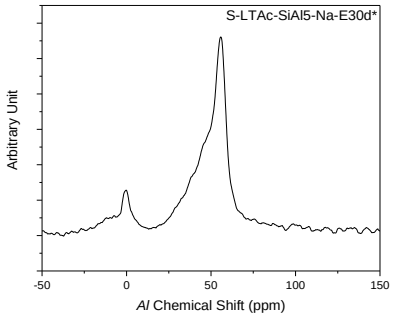

[27]Al NMR Spectra

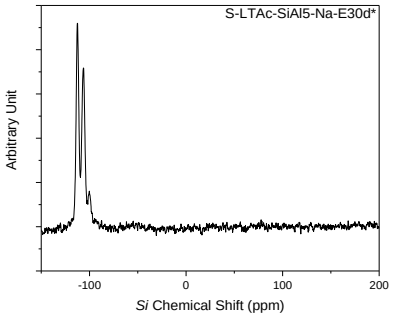

[29]Si NMR Spectra

8. PROPOSED FUTURE WORKS

Despite chronological and mechanical boundaries during a doctorate thesis, some research topics were not investigated and are just suggested for future works. Concerning interesting issues that were reveled throughout this run and themes associated with NG drying, hydrothermal stability and TSA topics.

Two interesting materials in this thesis that should be further analyzed are the S-LTAc-SiAl2-Na and S-CHAc-SiAl2-K. The sodium and potassium samples present an intermediate-low and low depositions of carbon, respectively, upon the aging protocol. In addition, both aged samples maintained the water vapor adsorption capacity. In order to assess the adsorption capacity, premature aging protocols must be performed for a longer extent to observe the carbon accumulation into the materials surface upon aging. In addition, other impurities commonly in NG produced in offshore plants, such as sulfur compounds and *CO*, must be consider in aging protocols.

The adsorbent deactivation is enhanced mainly by thermal stress associated to gas impurities, such as hydrocarbons. To improve the understanding of samples amorphization, XRD in situ analyses should be performed to better correlate the deactivation in a specific temperature range.

REFERENCES

A. Louis Allred. (1961). Electronegativity values from thermochemical data. *Journal of Inorganic and Nuclear Chemistry*, *17*(1949), 215–221. https://doi.org/10.1021/jp020500+

Alberti, A., Galli, E., Vezzalini, G., Passaglia, E., & Zanazzi, P. F. (1982). Position of cations and water molecules in hydrated chabazite. Natural and Na-, Ca-, Sr- and K-exchanged chabazites. *Zeolites*, *2*(4), 303–309. https://doi.org/10.1016/S0144-2449(82)80075-4

Aranovich, G. L., & Donohue, M. D. (1995). A New Approach to Analysis of Multilayer Adsorption. In *Journal of Colloid And Interface Science* (Vol. 173, Issue 2, pp. 515–520). https://doi.org/10.1006/jcis.1995.1353

Araújo, O. de Q. F., Reis, A. de C., de Medeiros, J. L., Nascimento, J. F. do, Grava, W. M., & Musse, A. P. S. (2017). Comparative analysis of separation technologies for processing carbon dioxide rich natural gas in ultra-deepwater oil fields. *Journal of Cleaner Production*, *155*, 12–22. https://doi.org/10.1016/j.jclepro.2016.06.073

Baghban, A., Kashiwao, T., Bahadori, M., Ahmad, Z., & Bahadori, A. (2016). Estimation of natural gases water content using adaptive neuro-fuzzy inference system. *Petroleum Science and Technology*, *34*(10), 891–897. https://doi.org/10.1080/10916466.2016.1176039

Baker, R. W., & Lokhandwala, K. (2008). Natural Gas Processing with Membranes: An Overview. *Industrial & Engineering Chemistry Research*, *47*(7), 2109–2121. https://doi.org/10.1021/ie071083w

Bare, S. R., Knop-Gericke, A., Teschner, D., Hävacker, M., Blume, R., Rocha, T., Schlögl, R., Chan, A. S. Y., Blackwell, N., Charochak, M. E., ter Veen, R., & Brongersma, H. H. (2016). Surface analysis of zeolites: An XPS, variable kinetic energy XPS, and low energy ion scattering study. *Surface Science*, *648*, 376–382. https://doi.org/10.1016/j.susc.2015.10.048

Barr, T. L., & Seal, S. (1995). Nature of the use of adventitious carbon as a binding energy standard. *Journal of Vacuum Science & Technology A: Vacuum, Surfaces, and Films*, *13*(3), 1239–1246. https://doi.org/10.1116/1.579868

Barry Crittenden, W. J. T. Fe. (1998). *Adsorption Technology Design*. Butterworth-Heinemann.

Bastos-Neto, M., Azevedo, D. C. S., & Lucena, S. M. P. (2020). Adsorption. In *Kirk-Othmer Encyclopedia of Chemical Technology* (pp. 1–59). Wiley. https://doi.org/10.1002/0471238961.0104191518212008.a01.pub3

Bevilacqua, M., Montanari, T., Finocchio, E., & Busca, G. (2006). Are the active sites of protonic zeolites generated by the cavities? *Catalysis Today*, *116*(2), 132–142. https://doi.org/10.1016/j.cattod.2006.01.024

Bhering, D. L., Ramírez-Solís, A., & Mota, C. J. A. (2003). A density functional theory based approach to extraframework aluminum species in zeolites. *Journal of Physical Chemistry B*, *107*(18), 4342–4347. https://doi.org/10.1021/jp022331z

Boronat, M., & Corma, A. (2019). *What Is Measured When Measuring Acidity in Zeolites with Probe*. https://doi.org/10.1021/acscatal.8b04317

Bourgogne, M., Guth, J.-L., & Wey, R. (1985). Process for the preparation of synthetic zeolites, and zeolites obtained by said process (Patent No. 4,503,024). In *US Patent: Vol. US* (4,503,024).

BPSTATS. (2019). BP Statistical Review of World Energy Statistical Review of World, 68th edition. *The Editor BP Statistical Review of World Energy*, 1–69. https://www.bp.com/content/dam/bp/business-sites/en/global/corporate/pdfs/energy-economics/statistical-review/bp-stats-review-2019-full-report.pdf

Bressel, A., Donauer, T., Sealy, S., & Traa, Y. (2008). Influence of aluminum content, crystallinity and crystallite size of zeolite Pd/H-ZSM-5 on the catalytic performance in the dehydroalkylation of toluene with ethane. *Microporous and Mesoporous Materials*, *109*(1–3), 278–286. https://doi.org/10.1016/j.micromeso.2007.05.002

Brönsted, J. N. (1923). Einige Bemerkungen über den Begriff der Säuren und Basen. *Recueil Des Travaux Chimiques Des Pays-Bas*, *42*(8), 718–728. https://doi.org/10.1002/recl.19230420815

Brown, T. L., H. Eugene LEMay, Jr., Bursten, B. E., Murphy, C. J., & Woodward, P. M. (2012). Chemistry - Central science. In *Chemical and Engineering News* (Twelfth Ed, Vol. 57, Issue 46). Pearson.

Brunauer, S., Deming, L. S., Deming, W. E., & Teller, E. (1940). On a Theory of the van der Waals Adsorption of Gases. *J. Am. Chem. Soc.*, *62*(7), 1723–1732. https://doi.org/10.1021/ja01864a025

Brunauer, S., Emmett, P. H., & Teller, E. (1938). Adsorption of Gases in Multimolecular Layers. *Journal of the American Chemical Society*, *60*(2), 309–319. https://doi.org/10.1021/ja01269a023

Bukhtiyarova, M. V., & Echevskii, G. V. (2020). Coke Formation on Zeolites Y and Their Deactivation Model. *Petroleum Chemistry*, *60*(4), 532–539. https://doi.org/10.1134/S0965544120040039

Burris, L. E., & Juenger, M. C. G. (2020). Effect of calcination on the reactivity of natural clinoptilolite zeolites used as supplementary cementitious materials. *Construction and Building Materials*, *258*, 119988. https://doi.org/10.1016/j.conbuildmat.2020.119988

Busca, G. (2017a). Acidity and basicity of zeolites: A fundamental approach. *Microporous and Mesoporous Materials*, *254*(June 2016), 3–16. https://doi.org/10.1016/j.micromeso.2017.04.007

Busca, G. (2017b). Acidity and basicity of zeolites: A fundamental approach. *Microporous and Mesoporous Materials*, *254*(June 2016), 3–16. https://doi.org/10.1016/j.micromeso.2017.04.007

Cadiau, A., Belmabkhout, Y., Adil, K., Bhatt, P. M., Pillai, R. S., Shkurenko, A., Martineau-Corcos, C., Maurin, G., & Eddaoudi, M. (2017). Hydrolytically stable fluorinated metal-organic frameworks for energy-efficient dehydration. *Science*, *356*(6339), 731–735. https://doi.org/10.1126/science.aam8310

Capasso, S., Coppola, E., Iovino, P., Salvestrini, S., & Colella, C. (2007). Sorption of humic acids on zeolitic tuffs. *Microporous and Mesoporous Materials*, *105*(3), 324–328. https://doi.org/10.1016/j.micromeso.2007.04.017

Capasso, S., Salvestrini, S., Coppola, E., Buondonno, A., & Colella, C. (2005). Sorption of humic acid on zeolitic tuff: a preliminary investigation. *Applied Clay Science*, *28*(1–4), 159–165. https://doi.org/10.1016/j.clay.2004.01.010

Cartlidge, S., Keller, E. B., & Meier, W. M. (1984). Role of potassium in the thermal stability of CHA- and EAB-type zeolites. *Zeolites*, *4*(3), 226–230. https://doi.org/10.1016/0144-2449(84)90028-9

Cavenati, S., Grande, C. A., & Rodrigues, A. E. (2006). Removal of carbon dioxide from natural gas by vacuum pressure swing adsorption. *Energy and Fuels*, *20*(6), 2648–2659. https://doi.org/10.1021/ef060119e

C.D. Wagner, W.M. Riggs, L.E. Davis, J.F. Moulder, G. E. M. (1979). *Handbook of X-Ray Photoelectron Spectroscopy*. Perkin-Elmer Corporation, Physical Eletronics Division.

Cejka, J., Bekkum, H. van, Corma, A., & Schüth, F. (2007). Introduction to Zeolite Science and Practice. In *Studies in Surface Science and Catalysis* (3rd Revise, Vol. 168). Elsevier.

Cejka, J., Xinjin, L., Bourgogne, M. M., Materials, S., Recovery, P., Characterization, P., Size, C., Bourgogne, M., & Wey, R. (1985). *IZA - Chabazite Synthesis* (Vol. 024, Issue 68).

Ch. Baerlocher, Lynne B. McCusker, D. H. O. (2007). Atlas of Zeolite Framework Types. In *Elsevier*. Elsevier Science.

Company, U. (2015). *Purification of olefin and polymer process streams (UOP Report 2015)*.

Corma, A. (1995). Inorganic Solid Acids and Their Use in Acid-Catalyzed Hydrocarbon Reactions. *Chemical Reviews*, *95*(3), 559–614. https://doi.org/10.1021/cr00035a006

Corma, A., & Martinez, A. (1995). Zeolites and Zeotypes as catalysts. *Advanced Materials*, *7*(2), 137–144. https://doi.org/10.1002/adma.19950070206

Corma, A., & Zones, S. (2010). Zeolites and Catalysis. In *Wiley-VCH Verlag GmbH & Co. KGaA*.

Cruciani, G. (2006). Zeolites upon heating: Factors governing their thermal stability and structural changes. *Journal of Physics and Chemistry of Solids*, *67*(9–10), 1973–1994. https://doi.org/10.1016/j.jpcs.2006.05.057

Cundy, C. S., & Cox, P. A. (2005). *The hydrothermal synthesis of zeolites : Precursors , intermediates and reaction mechanism*. *82*, 1–78. https://doi.org/10.1016/j.micromeso.2005.02.016

Dean, J. A. (1998). *Lange's Handbook of Chemistry* (Fifteenth). McGraw-Hill Professional.

Dent, L. S., & Smith, J. v. (1958). Crystal Structure of Chabazite, a Molecular Sieve. *Nature*, *181*(4626), 1794–1796. https://doi.org/10.1038/1811794b0

Doetsch, I. H., Ruthven, D. M., & Loughlin, K. F. (1974). Sorption and Diffusion of n -Heptane in 5A Zeolite. *Canadian Journal of Chemistry*, *52*(15), 2717–2724. https://doi.org/10.1139/v74-396

Dondur, V., Petranović, N., & Dimitrijevic, R. (1996). High Temperature Phase Transformations of Cation Exchanged Zeolites: A New Route for Synthesis of Aluminosilicate Materials. *Materials Science Forum*, *214*, 91–98. https://doi.org/10.4028/www.scientific.net/MSF.214.91

Dubinin, M.M., Radushkevich, L. V. (1947). Equation of the characteristic curve of activated charcoal. *Proc. Acad. Sci. Phys. Chem. Sec. USSR*, *55*, 331–333.

Duer, M. J. (2001). *Solid-State NMR Spectroscopy Principles and Applications* (B. Science, Ed.; First publ).

Evans, S. (1997). Correction for the effects of adventitious carbon overlayers in quantitative XPS analysis. *Surface and Interface Analysis*, *25*(12), 924–930. https://doi.org/10.1002/(SICI)1096-9918(199711)25:12<924::AID-SIA317>3.0.CO;2-2

Farag, H. A. A., Ezzat, M. M., Amer, H., & Nashed, A. W. (2011). Natural gas dehydration by desiccant materials. *Alexandria Engineering Journal*, *50*(4), 431–439. https://doi.org/10.1016/j.aej.2011.01.020

Feng, X., Zong, Z., Elsaidi, S. K., Jasinski, J. B., Krishna, R., Thallapally, P. K., & Carreon, M. A. (2016). Kr/Xe Separation over a Chabazite Zeolite Membrane. *Journal of the American Chemical Society*, *138*(31), 9791–9794. https://doi.org/10.1021/jacs.6b06515

Fernández-Barquín, A., Casado-Coterillo, C., Valencia, S., & Irabien, A. (2016). Mixed Matrix Membranes for O2/N2 Separation: The Influence of Temperature. *Membranes*, *6*(2), 28. https://doi.org/10.3390/membranes6020028

Freeman, B., Yampolskii, Y., & Pinnau, I. (2006). *Materials Science of Membranes for Gas and Vapor Separation* (Y. Yampolskii, I. Pinnau, & B. Freeman, Eds.). John Wiley & Sons, Ltd. https://doi.org/10.1002/047002903X

Funke, H. H., Argo, A. M., Baertsch, C. D., Falconer, J. L., & Noble, R. D. (1996). Separation of close-boiling hydrocarbons with silicalite zeolite membranes. *Journal of the Chemical Society - Faraday Transactions*, *92*(13), 2499–2502. https://doi.org/10.1039/ft9969202499

Gaffney, T. R., & Coe, C. G. (1991). *Processfor the Preparation of an Improved Chabazite for the Purification of Bulk Gases* (Patent No. 5,026,532).

García-Martínez, J., Cazorla-Amorós, D., & Linares-Solano, A. (2000). Further evidences of the usefulness of CO2 adsorption to characterize microporous solids. In *Encyclopedia of volcanoes.* (Issue 1995, pp. 485–494). https://doi.org/10.1016/S0167-2991(00)80054-3

Getu, M., Mahadzir, S., Long, N. V. D., & Lee, M. (2013). Techno-economic analysis of potential natural gas liquid (NGL) recovery processes under variations of feed compositions. *Chemical Engineering Research and Design*, *91*(7), 1272–1283. https://doi.org/10.1016/j.cherd.2013.01.015

Gomes Santiago, R., Ferreira dos Santos, B., Gomes Lima, I., Oliveira Moura, K., Carrijo Melo, D., Mantovani Grava, W., Bastos-Neto, M., Pereira de Lucena, S. M., & Cristina Silva de Azevedo, D. (2019). Investigation of premature aging of zeolites used in the drying of gas

streams. *Chemical Engineering Communications*, *206*(11), 1378–1385. https://doi.org/10.1080/00986445.2018.1533468

Greaves, G. N., Meneau, F., Sapelkin, A., Colyer, L. M., Gwynn, I. ap, Wade, S., & Sankar, G. (2003). The rheology of collapsing zeolites amorphized by temperature and pressure. *Nature Materials*, *2*(9), 622–629. https://doi.org/10.1038/nmat963

Guisnet, M., & Magnoux, P. (1989). Coking and deactivation of zeolites. *Applied Catalysis*, *54*(1), 1–27. https://doi.org/10.1016/S0166-9834(00)82350-7

Guisnet, M., Magnoux, P., & Martin, D. (1997). *Roles of acidity and pore structure in the deactivation of zeolites by carbonaceous deposits* (pp. 1–19). https://doi.org/10.1016/S0167-2991(97)80138-3

Gulín-González, J., & Suffritti, G. B. (2004). Amorphization of calcined LTA zeolites at high pressure: A computational study. *Microporous and Mesoporous Materials*, *69*(1–2), 127–134. https://doi.org/10.1016/j.micromeso.2004.02.002

Hammerschmidt, E. G. (1934). Formation of Gas Hydrates in Natural Gas Transmission Lines. *Industrial and Engineering Chemistry*, *26*(8), 851–855. https://doi.org/10.1021/ie50296a010

Huang, Y., & Havenga, E. A. (2001). Why do zeolites with LTA structure undergo reversible amorphization under pressure? *Chemical Physics Letters*, *345*(1–2), 65–71. https://doi.org/10.1016/S0009-2614(01)00856-9

IEA. (2021). *World Energy Outlook 2021 - revised version October 2021*.

IMF. (2019). International Monetary Fund 2019. In *International Monetary Fund 2019*.

Jansen, J. C. M. M. G. H. J. C. (1998). DSC and TG Study of Water Adsorption and Desorption on Zeolite NaA. *Journal of Thermal Analysis*, *53*, 449–466. https://doi.org/https://doi.org/10.1023/A:1010137307816

Karge, H. G. (1991). Chapter 14 Coke Formation on Zeolites. *Studies in Surface Science and Catalysis*, *58*(C), 531–570. https://doi.org/10.1016/S0167-2991(08)63612-5

Kawai, T., & Tsutsumi, K. (1992). Evaluation of hydrophilic-hydrophobic character of zeolites by measurements of their immersional heats in water. *Colloid & Polymer Science*, *270*(7), 711–715. https://doi.org/10.1007/BF00654048

Kennedy, D. A., & Tezel, F. H. (2018). Cation exchange modification of clinoptilolite – Screening analysis for potential equilibrium and kinetic adsorption separations involving

methane, nitrogen, and carbon dioxide. *Microporous and Mesoporous Materials*, *262*(September 2018), 235–250. https://doi.org/10.1016/j.micromeso.2017.11.054

Kerr, G. T. (1967). Intracrystalline rearrangement of constitutive water in hydrogen zeolite Y. *The Journal of Physical Chemistry*, *71*(12), 4155–4156. https://doi.org/10.1021/j100871a079

Koningsveld, H. van. (2007). *Compendium of Zeolite Framework Types*.

Kosanović, C., Subotić, B., Šmit, I., Čižmek, A., Stubičar, M., & Tonejc, A. (1997). Study of structural transformations in potassium-exchanged zeolite a induced by thermal and mechanochemical treatments. *Journal of Materials Science*, *32*(1), 73–78. https://doi.org/10.1023/A:1018514929882

Kubesh, J., King, S. R., & Liss, W. E. (1992). Effect of gas composition on octane number of natural gas fuels. *SAE Technical Papers*. https://doi.org/10.4271/922359

Langmuir, I. (1918). The Adsorption of Gases on Plane Surfaces of Glass, Mica and Platinum. *Journal of the American Chemical Society*, *40*(9), 1361–1403. https://doi.org/10.1021/ja02242a004

Lewis, G. N. (1916). THE ATOM AND THE MOLECULE. *Journal of the American Chemical Society*, *38*(4), 762–785. https://doi.org/10.1021/ja02261a002

Liu, C., Li, G., Hensen, E. J. M., & Pidko, E. A. (2015). Nature and Catalytic Role of Extraframework Aluminum in Faujasite Zeolite: A Theoretical Perspective. *ACS Catalysis*, *5*(11), 7024–7033. https://doi.org/10.1021/acscatal.5b02268

Liu, L., Wang, L., Liu, D., Yang, Q., & Zhong, C. (2020). High-Throughput Computational Screening of Cu-MOFs with Open Metal Site for Efficient C2H2/C2H4 Separation. *Green Energy and Environment*. https://doi.org/10.1016/j.gee.2020.03.002

Loewenstein, W. (1954). The distribution of aluminum in the tetrahedra of silicates and aluminates. *American Mineralogist*, *39*(1–2), 92–96.

Lopez, Z. E., González, G., & Reichelt, R. (2003). Effect of the Si/Al Ratio on the Size and Morphology of the Crystals of Zeolites MFI and MEL. *Microscopy and Microanalysis*, *9*(S03), 362–363. https://doi.org/10.1017/S1431927603027089

Lowry, T. M. (1923). The uniqueness of hydrogen. *Journal of the Society of Chemical Industry*, *42*(3), 43–47. https://doi.org/10.1002/jctb.5000420302

Madani, S. H., Silvestre-Albero, A., Biggs, M. J., Rodríguez-Reinoso, F., & Pendleton, P. (2015). Immersion Calorimetry: Molecular Packing Effects in Micropores. *ChemPhysChem*, *16*(18), 3984–3991. https://doi.org/10.1002/cphc.201500580

Malenshek, M., & Olsen, D. B. (2009). Methane number testing of alternative gaseous fuels. *Fuel*, *88*(4), 650–656. https://doi.org/10.1016/j.fuel.2008.08.020

Marić, I. (2005). The Joule-Thomson effect in natural gas flow-rate measurements. *Flow Measurement and Instrumentation*, *16*(6), 387–395. https://doi.org/10.1016/j.flowmeasinst.2005.04.006

McKinsey & Company. (2019). Global Energy Perspective 2019 : Reference Case. In *Energy Insights* (Issue January).

Menad, K., Feddag, A., & Rubenis, K. (2016). Synthesis and study of calcination temperature influence on the change of structural properties of the LTA zeolite. *Rasayan Journal of Chemistry*, *9*(4), 788–797.

Mintova, S., & Barrier, N. (2016). *Verified Syntheses of Zeolitic Materials* (Third Ed.). International Zeolite Association - IZA.

MOGHIMI, F., JAFARI, A. H., YOOZBASHIZADEH, H., & ASKARI, M. (2020). Adsorption behavior of Sb(III) in single and binary Sb(III)—Fe(II) systems on cationic ion exchange resin: Adsorption equilibrium, kinetic and thermodynamic aspects. In *Transactions of Nonferrous Metals Society of China (English Edition)* (Vol. 30, Issue 1, pp. 236–248). https://doi.org/10.1016/S1003-6326(19)65195-2

Mortier, W. J., Pluth, J. J., & Smith, J. V. (1977). Positions of Cations and Molecules in Zeolites. *Pergamon Press*, *12*(i), 1001–1007.

Moscoso, J. G., & Lewis, G. J. (2003). *Crystalline Aluminpsilicate Zeolitic Composition: UZM-9* (Patent No. WO 03/068679 A1).

Mota, C. J. A., Bhering, D. L., & Rosenbach, N. (2004). A DFT study of the acidity of ultrastable Y zeolite: Where is the Brønsted/Lewis acid synergism? *Angewandte Chemie - International Edition*, *43*(23), 3050–3053. https://doi.org/10.1002/anie.200353049

Moura, P. A. S., Bezerra, D. P., Vilarrasa-Garcia, E., Bastos-Neto, M., & Azevedo, D. C. S. (2016). Adsorption equilibria of CO2 and CH4 in cation-exchanged zeolites 13X. *Adsorption*, *22*(1), 71–80. https://doi.org/10.1007/s10450-015-9738-9

Moura, P. A. S., Rodríguez-Aguado, E., Maia, D. A. S., Melo, D. C., Singh, R., Valencia, S., Webley, P. A., Rey, F., Bastos-Neto, M., Rodríguez-Castellón, E., & Azevedo, D. C. S.

(2021). Water adsorption and hydrothermal stability of CHA zeolites with different Si/Al ratios and compensating cations. *Catalysis Today*. https://doi.org/10.1016/j.cattod.2021.11.042

Mutch, G. A., Qu, L., Triantafyllou, G., Xing, W., Fontaine, M. L., & Metcalfe, I. S. (2019). Supported molten-salt membranes for carbon dioxide permeation. *Journal of Materials Chemistry A*, *7*(21), 12951–12973. https://doi.org/10.1039/c9ta01979k

Myers, a L., & Prausnitz, J. M. (1965). Thermodynamics of mixed-gas adsorption. *AIChE Journal*, *11*(1), 121–127. https://doi.org/10.1002/aic.690110125

Nachtigall, P., Delgado, M. R., Nachtigallova, D., & Arean, C. O. (2012). *The nature of cationic adsorption sites in alkaline zeolites — single , dual and multiple cation sites*. 1552–1569. https://doi.org/10.1039/c2cp23237e

Nascimento, B. O., dos Santos, B. F., Maia, D. A. S., de Melo, D. C., Vilarrasa-Garcia, E., Torres, A. E. B., Bastos-Neto, M., & Azevedo, D. C. S. (2021). Water adsorption in fresh and thermally aged zeolites: equilibrium and kinetics. *Adsorption*. https://doi.org/10.1007/s10450-021-00331-x

OECD. (2020). *Monthly Gas Statistics (Dec/2019)*.

OGJ. (2019). Worldwide (Oil Reserves and Oil Production). In *Worldwide Oil Report 2019*. Oil and Gas Journal.

Park, J. W., & Seo, G. (2009). IR study on methanol-to-olefin reaction over zeolites with different pore structures and acidities. *Applied Catalysis A: General*, *356*(2), 180–188. https://doi.org/10.1016/j.apcata.2009.01.001

Perez-Carbajo, J., Balestra, S. R. G., Calero, S., & Merkling, P. J. (2020). Effect of lattice shrinking on the migration of water within zeolite LTA. *Microporous and Mesoporous Materials*, *293*(March 2019), 109808. https://doi.org/10.1016/j.micromeso.2019.109808

Phung, T. K., & Busca, G. (2015). On the Lewis acidity of protonic zeolites. *Applied Catalysis A: General*, *504*, 151–157. https://doi.org/10.1016/j.apcata.2014.11.031

Poling, B. E., Prausnitz, J. M., & O'Connell, J. P. (2001). The Properties of Gases and Liquids. In *Solutions* (Fifth Edit, Issue C). McGRAW-HILL. https://doi.org/10.1036/0070116822

Pulido, A., Nachtigall, P., Zukal, A., Dominguez, I., & Čejka, J. (2009). Adsorption of CO 2 on sodium-exchanged ferrierites: The bridged CO 2 complexes formed between two extraframework cations. *Journal of Physical Chemistry C*, *113*(7), 2928–2935. https://doi.org/10.1021/jp810038b

Ravi, M., Sushkevich, V. L., & van Bokhoven, J. A. (2020). Towards a better understanding of Lewis acidic aluminium in zeolites. *Nature Materials*, *19*(10), 1047–1056. https://doi.org/10.1038/s41563-020-0751-3

Rezvani, H., & Fatemi, S. (2020). Influence of water vapor condensation inside nano-porous 4A adsorbent in adsorption-desorption cyclic process of natural gas dehydration. *Separation Science and Technology (Philadelphia)*, *55*(7), 1286–1302. https://doi.org/10.1080/01496395.2019.1593455

Ribeiro, F. R., Alvarez, F., Henriques, C., Lemos, F., Lopes, J. M., & Ribeiro, M. F. (1995). Structure-activity relationship in zeolites. *Journal of Molecular Catalysis A: Chemical*, *96*(3), 245–270. https://doi.org/10.1016/1381-1169(94)00058-1

Ridha, F. N., Yang, Y., & Webley, P. A. (2009). Adsorption characteristics of a fully exchanged potassium chabazite zeolite prepared from decomposition of zeolite Y. *Microporous and Mesoporous Materials*, *117*(1–2), 497–507. https://doi.org/10.1016/j.micromeso.2008.07.034

Rouquerol, F., Rouquerol, J., Sing, K., Llewellyn, P., Maurin, G. (2014). Adsorption at the Liquid-Solid Interface: Thermodynamics and Methodology. In *Adsorption by Powders and Porous Solids: Principles, Methodology and Applications: Second Edition*. https://doi.org/10.1016/B978-0-08-097035-6.00004-8

Ruska, E. (1987). The Development of the Electron Microscope and of Electron Microscopy (Nobel Lecture). *Angewandte Chemie International Edition in English*, *26*(7), 595–605. https://doi.org/10.1002/anie.198705953

Ruthven, D. M. (1984). *Principles of Adsorption and Adsorption Properties* (J. W. & Sons, Ed.).

Salinas-Martinez de Lecea, C., Linares-Solano, A., Rodriguez-Reinoso, F., & Sepulveda-Escribano, A. (1988). Carbon Dioxide Subtraction (CDS) Method Applied to A Wide Range of Porous Carbons. In *Studies in Surface Science and Catalysis* (Vol. 39, Issue C, pp. 173–182). https://doi.org/10.1016/S0167-2991(09)60741-2

Santos, M. G. R. S., Correia, L. M. S., de Medeiros, J. L., & Araújo, O. de Q. F. (2017). Natural gas dehydration by molecular sieve in offshore plants: Impact of increasing carbon dioxide content. *Energy Conversion and Management*, *149*, 760–773. https://doi.org/10.1016/j.enconman.2017.03.005

Shannon, R. D. (1976). Revised Effective Ionic Radii and Systematic Studies of Interatomie Distances in Halides and Chaleogenides. *Acta Crystallographica*, 751–767.

Sharma, P., Han, M. H., & Cho, C.-H. (2015). Synthesis of Zeolite Nanomolecular Sieves of Different Si/Al Ratios. *Journal of Nanomaterials*, *2015*, 1–9. https://doi.org/10.1155/2015/912575

Shim, S. H., Navrotsky, A., Gaffney, T. R., & Macdougall, J. E. (1999a). Chabazite: Energetics of hydration, enthalpy of formation, and effect of cations on stability. *American Mineralogist*, *84*(11–12), 1870–1882. https://doi.org/10.2138/am-1999-11-1214

Shim, S. H., Navrotsky, A., Gaffney, T. R., & Macdougall, J. E. (1999b). Chabazite: Energetics of hydration, enthalpy of formation, and effect of cations on stability. *American Mineralogist*, *84*(11–12), 1870–1882. https://doi.org/10.2138/am-1999-11-1214

Silaghi, M. C., Chizallet, C., & Raybaud, P. (2014). Challenges on molecular aspects of dealumination and desilication of zeolites. *Microporous and Mesoporous Materials*, *191*, 82–96. https://doi.org/10.1016/j.micromeso.2014.02.040

Silaghi, M.-C., Chizallet, C., Sauer, J., & Raybaud, P. (2016). Dealumination mechanisms of zeolites and extra-framework aluminum confinement. *Journal of Catalysis*, *339*, 242–255. https://doi.org/10.1016/j.jcat.2016.04.021

Silvestre-Albero, J., Silvestre-Albero, A., Rodríguez-Reinoso, F., & Thommes, M. (2012). Physical characterization of activated carbons with narrow microporosity by nitrogen (77.4 K), carbon dioxide (273 K) and argon (87.3 K) adsorption in combination with immersion calorimetry. *Carbon*, *50*(9), 3128–3133. https://doi.org/10.1016/j.carbon.2011.09.005

Sing, K. S. W. (2014). Assessment of Surface Area by Gas Adsorption. In *Adsorption by Powders and Porous Solids* (2nd ed., pp. 237–268). Elsevier. https://doi.org/10.1016/B978-0-08-097035-6.00007-3

Singh, R. K., & Webley, P. (2005). Adsorption of N2, O2, and Ar in potassium chabazite. *Adsorption*, *11*(1 SUPPL.), 173–177. https://doi.org/10.1007/s10450-005-5918-3

Sircar, S. (2006). Basic research needs for design of adsorptive gas separation processes. *Industrial and Engineering Chemistry Research*, *45*(16), 5435–5448. https://doi.org/10.1021/ie051056a

Speight, J. G. (2019). Natural Gas A Basic Handbook. In P. J. J. Collett (Ed.), *2nd* (2nd ed.). MPS Limited.

Stepanov, A. G. (2016). Basics of Solid-State NMR for Application in Zeolite Science. In *Zeolites and Zeolite-Like Materials* (pp. 137–188). Elsevier. https://doi.org/10.1016/B978-0-444-63506-8.00004-5

Stephen Brunauer, P. H. Emmett, E. T. (1938). Adsorption of Gases in Multimolecular Layers. *Journal of the American Chemical Society*, *60*, 309–319. https://doi.org/10.1007/978-94-017-2539-2_3

Sun, P., Yu, D., Fu, K., Gu, M., Wang, Y., Huang, H., & Ying, H. (2009). Potassium modified NaY: A selective and durable catalyst for dehydration of lactic acid to acrylic acid. *Catalysis Communications*, *10*(9), 1345–1349. https://doi.org/10.1016/j.catcom.2009.02.019

Talaghat, M. R., & Khodaverdilo, A. R. (2019). Study of different models of prediction of the simple gas hydrates formation induction time and effect of different equations of state on them. *Heat and Mass Transfer*, *55*(5), 1245–1255. https://doi.org/10.1007/s00231-018-2508-y

Theodore L., M. W. B., H. Eugene Jr., L., Bruce E., B., Catherine J., M., Patrick M., W., & Stoltzfus. (2017). *Chemsitry The Central Science: Vol. 11th Editi* (Pearson, Ed.; 14th Editi, Issue 2).

Thommes, M., Kaneko, K., Neimark, A. v., Olivier, J. P., Rodriguez-Reinoso, F., Rouquerol, J., & Sing, K. S. W. (2015). Physisorption of gases, with special reference to the evaluation of surface area and pore size distribution (IUPAC Technical Report). *Pure and Applied Chemistry*, *87*(9–10), 1051–1069. https://doi.org/10.1515/pac-2014-1117

Tóth, J. (2003). On thermodynamical inconsistency of isotherm equations: Gibbs's thermodynamics. *Journal of Colloid and Interface Science*, *262*(1), 25–31. https://doi.org/10.1016/S0021-9797(03)00236-4

Treacy, M. M. J., & Higgins, J. B. (2007). Collection of Simulated XRD Powder Patterns for Zeolites. In *Collection of Simulated XRD Powder Patterns for Zeolites Fifth (5th) Revised Edition*. Elsevier. https://doi.org/10.1016/B978-0-444-53067-7.X5470-7

Van Duc Long, N., & Lee, M. (2013). A novel NGL (natural gas liquid) recovery process based on self-heat recuperation. *Energy*, *57*, 663–670. https://doi.org/10.1016/j.energy.2013.04.078

VGB. (2020). VGB Powertech Report 2019|2020. In *New Civil Engineer*.

Vigil de la Villa Mencía, R., Goiti, E., Ocejo, M., & Giménez, R. G. (2020). Synthesis of zeolite type analcime from industrial wastes. *Microporous and Mesoporous Materials*, *293*(November), 1–9. https://doi.org/10.1016/j.micromeso.2019.109817

Wadlinger, R. L., Rosinski, E. J., & Plank, C. J. (1968). *Synthetic Zeolite* (Patent No. 3,375,205).

Wang, Y. (2020). Measurements and Modeling of Water Adsorption Isotherms of Zeolite Linde-Type A Crystals. *Industrial and Engineering Chemistry Research*, *59*(17), 8304–8314. https://doi.org/10.1021/acs.iecr.9b06891

Xu, B., Rotunno, F., Bordiga, S., Prins, R., & Vanbokhoven, J. (2006). Reversibility of structural collapse in zeolite Y: Alkane cracking and characterization. *Journal of Catalysis*, *241*(1), 66–73. https://doi.org/10.1016/j.jcat.2006.04.009

Yan, Y., & Bein, T. (1992). Molecular recognition on acoustic wave devices: Sorption in chemically anchored zeolite monolayers. *Journal of Physical Chemistry*, *96*(23), 9387–9393. https://doi.org/10.1021/j100202a060

Yu, J. (2007). Chapter 3 SYNTHESIS OF ZEOLITES. In F. S. J. Cajka, H. van Bekkum, A. Corma (Ed.), *Introduction to Zeolite Science and Practice* (3rdRevised ed., pp. 1–65). Elsevier B. V. https://doi.org/10.1016/S0167-2991(07)80791-9

Zones, S. I. (1991). Conversion of faujasites to high-silica chabazite SSZ-13 in the presence of N,N,N-trimethyl-1-adamantammonium iodide. *Journal of the Chemical Society, Faraday Transactions*, *87*(22), 3709–3716. https://doi.org/10.1039/FT9918703709